Martin-Luther-Universität
Halle-Wittenberg

Multiferroic tunnel structures

Dissertation

zur Erlangung des
Doktorgrades der Naturwissenschaften (Dr. rer. nat.)

vorgelegt an der

Naturwissenschaftlichen Fakultät II - Chemie, Physik und Mathematik

von

Herrn Dipl.-Phys. Andy U. Quindeau
geboren am 01.07.1984 in Duisburg

1. Gutachter: Prof. Dr. Dietrich Hesse

2. Gutachter: Prof. Dr. Hermann Kohlstedt

3. Gutachter: Prof. Dr. Georg Schmidt

Halle (Saale), 02. Juni 2015

To Madita

Contents

List of Figures

List of Tables

Abbreviation	**Short for**
AC	Alternating current
AFM*	Antiferromagnet
AFM	Atomic force microscopy
CAFM	Conductive AFM
CCD	Charge coupled device
DART	Dual AC resonance tracking
DC	Direct current
DOS	Density of states
EB	Exchange bias
EDX	Energy dispersive X-ray spectroscopy
FC	Field cooling
FE	Ferroelectric
FIB	Focused ion beam
FM	Ferromagnet
FTJ	Ferroelectric tunnel junction
GM	Glazman-Matveev (model)
HAADF	High angle annular dark field
HDD	Hard disc drive
HREM	High resolution electron microscopy
IV	Current - voltage
KAI	Kolmogorov-Avrami-Ishibashi (model)
LAD	Laser ablation and deposition
LBL	Layer-by-layer (growth mode)
LED	Light emitting diode
LSMO	$LaSr_{0.3}Mn_{0.7}O_3$, Lanthanum strontium manganite
ME	Magnetoelectric
MFTJ	Multiferroic tunnel junction
MO	Magnetooptic
MOKE	Magneto-optical Kerr effect
(L)-MOKE	Longitudinal magneto-optical Kerr effect
(P)-MOKE	Polar magneto-optical Kerr effect
(T)-MOKE	Transversal magneto-optical Kerr effect
MPI	Max Planck Institute
PFM	Piezoforce microscope/microscopy
PLD	Pulsed laser deposition
PPMS	Physical property measurement system
PTO	$PbTiO_3$, Lead titanate
PUND	Positive up negative down
PZO	$PbZrO_3$, Lead zirconate
PZT	$PbZr_{0.2}Ti_{0.8}O_3$, Lead zirconate titanate
(M/F)-RAM	(Magnetic/Ferroelectric) random access memory
RHEED	Reflection high energy electron diffraction
RSM	Reciprocal space map
SMU	Source meter unit

SPT	Spin polarized tunneling
SQUID	Superconducting quantum interference device
STEM	Scanning TEM
STO	$SrTiO_3$, Strontium titanate
SXRD	Surface XRD
TAMR	Tunnel anisotropic magneto resistance
TDF	Thermal diffuse scattering
TEM	Transmission electron microscope/microscopy
TER	Tunnel electro resistance
TMR	Tunnel magneto resistance
UV(L)	Ultra violet (light lithography)
XMCD	X-ray magnetic circular dichroism
XRMS	X-ray resonant magnetic scattering
XRD	X-ray diffraction

GLOSSARY

1

Introduction

Some of the most intriguing questions of modern science and engineering are related to energy efficiency and computational power. Quantum computing [1], for instance, is a prominent candidate to solve many of the proposed computational problems such as large integer factorization [2], but has yet to be experimentally realized.

Trying to avoid fundamental bottlenecks [3] in classic approaches, one path to an increase in computing power has been heavily driving the computer industry now for the last decade: Parallelization [4].

Instead of boosting clock frequencies of processing units in order to linearly scale floating point operations, the clear trend was already set by the much older development of supercomputers. Clusters of processing units, today bundled together in graphics cards [5], work in parallel on scalable problems with very sophisticated algorithms that allow a high level of parallelization.

Yet, with the upscale of data processing capabilities, new requirements on data storage density and speed simultaneously become important. One way to combine both trends is to literally fuse memory and processing units together.

As for many disciplines in science and engineering, nature is a great template for what is possible in this field. A highly energy efficient, vastly powerful computer, the mammalian brain is one of the major complex systems that has not yet been attempted to be seriously engineered. However, so called memristive devices have, in principle, the potential to mimic the neural architecture of mammalian brains [6, 7] in means of processing and memorizing within single integrated elements. Being slow in digital single-stream throughput, but extremely fast in pattern recognition and self-optimizing [8], neuromorphic computing with memristors could lead to a new era in many areas of information technology [9].

As a first step and by utilizing and designing highly functional materials at the nanoscale, the problem of how energy efficiency could be tackled has already been proposed. The tunnel electro resistance (TER) effect [10], which is the dependence of the electron tunnel resistance on the remanently switchable ferroelectric polarization direction of a ferroelectric tunnel barrier, is a great example. It dissipates orders of magnitudes less energy per logic switch operation than the reversal of the magnetization direction of one bit via an electrical current, which is still used in hard disc drives for mass data storage facilities [11].

This novel phenomenon was first theoretically predicted in 2005 [12, 13] and experimentally realized in 2009 [14, 15]. First devices in capacitor geometry have been built

[16] based on the ferroelectric material $PbZr_{0.2}Ti_{0.8}O_3$ (PZT) [17] and $BaTiO_3$ [18, 19].

Dependent on the interfacial electronic properties resulting from the combination of magnetic and ferroelectric materials, multiferroic memories combine TMR[1] and TER [20], and have been experimentally designed already [21, 22]. Magnetoelectric (ME) coupling phenomena [23] that are presumably based on the interfacial atomic order were measured by means of the electric switching of the electron spin polarization in multiferroic tunnel junctions (MFTJ) [24].

Studying the origin of this coupling phenomenon was the main motivation behind the work on this thesis. With the advancement of lab equipment and knowledge in this field[2], it was possible to grow multiferroic tunnel junctions in a much more controlled and purposeful way and thus thoroughly study interface effects either directly with synchrotron radiation or indirectly via interface engineering.

As a starting point of the studies, junctions with deviations from the well known composition of PZT [25, 26] as ferroelectric tunnel barrier will be grown and optimized. The highly magnetoelectrically coupled system involving magnetic $La_{0.7}Sr_{0.3}MnO_3$ and cobalt electrodes will be investigated with emphasis on the interface between the ferroelectric barrier and cobalt. Based on theoretical predictions, this interface seems to play the key role in the magnetoelectric coupling, which might stem from a ferroelectrically induced proximity effect between the interfacial titanium of the PZT matrix and the first layer of cobalt atoms.

The second pillar of the thesis is dedicated to the TER alone. Besides the ability to tune the resistance of a ferroelectric tunnel junction (FTJ) digitally, meaning the possibility to switch between two resistive states ON and OFF in a very robust [27] way, the resistance of a TER junction can be tuned analogously. This was simultaneously and independently found during the work on this thesis by other groups in 2012 [18, 19]. The aim is to understand the principles of this ferroelectric tunnel memristor and to find a characteristic transfer function that would allow programming of the analogous resistive state of this two-terminal device. This would combine the two proposed advantages of high energy efficiency and parallelization within a ferroelectric tunnel junction.

After this brief first introduction, the thesis will continue by substantiating the experimentally obtained and later analyzed data with a Fundamentals chapter (2), which will be followed by a presentation of the employed methods (chapter 3).

In chapter 4, the growth optimization with focus on ultrathin ferroelectric layers will be presented. The main results of this thesis, exhibiting the analysis of TER and TMR of the measured MFTJs, are discussed in chapter 5. Chapter 6 will continue the examination of TER with emphasis on the possibility to use a ferroelectric tunnel junction as a memristor. Chapter 7 will be dedicated to the conducted Synchrotron studies and will finally lead into the Summary and outlook with chapter 8.

---

[1] TMR: Tunnel magneto resistance

[2] In strong collaboration with V. Borisov and Prof. I. Mertig.

2

Fundamentals

This chapter will provide the necessary background to analyze the experimentally acquired results. After explaining multiferroicity, material properties and relevant electronic transport mechanisms, the characterization and growth methods will be explained in a subsequent chapter. Since a part of this thesis will address the possibility to use a ferroelectric tunnel junction as a circuit element called a memristor [4, 8, 18, 19, 28, 29, 30], the working principles of such a device will be discussed.

2.1 Multiferroics

Ferroic materials in general possess at least one property that shows a long range spontaneous order [31]. These properties can be elasticity, electric polarity (ferroelectricity) and ferromagnetism. If a material or a nanostructured composition of materials possesses more than one of these attributes, it is referred to as multiferroic material. Although the order parameter of a ferroic material can usually be influenced by applying an excitation of the same kind (electric field for a ferroelectric, magnetic field for a ferromagnet etc.), coupling between ferroic properties is achievable and results in interesting fields of study. It is, for example, possible to reverse the ferroelectric polarization of $BaTiO_3$ by applying mechanical stress with an atomic force microscopy tip [32].

2.1.1 Ferroelectrics

As the name indicates, a ferroelectric material possesses a spontaneous electric order, a polarity, that can be switched by an electric field. The origin of the polarization can be explained on the tetragonal pseudo-cubic unit cell of the perovskite $PbTiO_3$, which is one of the ferroelectric materials that is used in this work (see **Fig. 2.1**). In this case, the body-centered cation Ti possesses only two stable positions inside the ionic potential (**Fig. 2.1 c**) given by the surrounding oxygen octaedron. As a result of the effective ion displacement, the cell possesses an electric dipole along its symmetry (c) axis [33], which creates an effective surface charge (ferroelectric polarization) on the $(00l)$-planes. The electric potential between the two possible stable states has to be overcome in order to switch the ferroelectric polarization direction of the crystal. The corresponding electric field is called the coercive field. The larger the displacement of

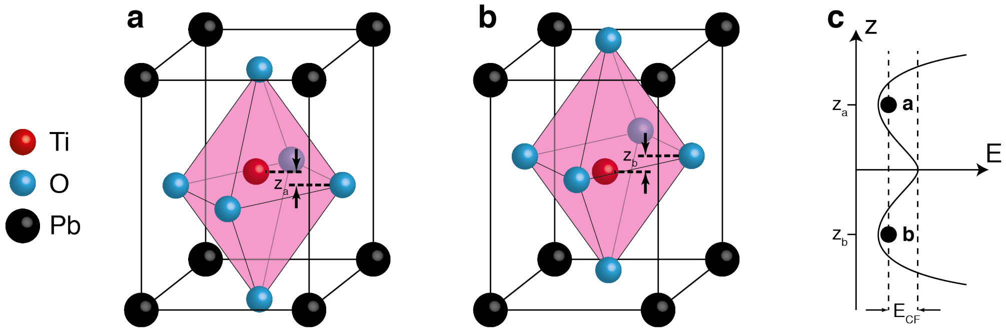

Figure 2.1: Exemplary tetragonal unit cell of the ferroelectric PbTiO$_3$. a, Tetragonal unit cell of PbTiO$_3$ in the ferroelectric phase. The oxygen octahedron is displaced in the elongated direction against the bcc subcell containing lead and titanium. **b**, The same tetragonal unit cell as in **a** after polarization reversal. **c**, Potential for the titanium cation inside the unit cell along the z-axis. There are two stable states (at positions z_a and z_b) that are separated by a potential wall (equivalent to the ferroelectric coercive field).

the ions against each other, the larger is the ferroelectric polarization per unit cell, which is the reason for a strong correlation between strain and ferroelectricity.

Commonly, the phase transition temperature of ferroelectric materials is rather high and can be explained by the Ginzburg-Landau theory. In the monocrystalline tetragonal case, in which the ferroelectric polarization P_z is parallel to the tetragonal elongation of the ferroelectric unit cell ([00l]-direction), the energy potential in z-direction has the shape of a double potential well of the form:

$$\Delta E = \frac{1}{2}\alpha_0 \left(T - T_0\right) P_z^2 + \frac{1}{4}\alpha_{11} P_z^4 + \frac{1}{6}\alpha_{111} P_z^6 \tag{2.1}$$

T_0 is the phase transition temperature, the α_{xyz} are ferroelectric coefficients for the Cartesian coordinate system. The sign of the ferroelectric coefficient α_{11} determines the order of the phase transition, which is first-order for negative α_{11} and second-order for positive α_{11}.

Above the phase transition temperature, the shown PTO lattice looses its tetragonal elongation and becomes simple cubic. For the titanium inside the unit cell, the stable position in this case is exactly the center, which is why the crystal looses its spontaneous cation-anion displacement and thus its ferroelectricity.

2.1.2 Ferromagnet - antiferromagnet interaction

The interaction of ferromagnetic and antiferromagnetic materials can cause a uniaxial (exchange) anisotropy [34]. This interface effect potentially leads to an offset along a magnetic axis, which can usually be identified as a shift of a measured magnetic hysteresis loop along the applied magnetic field axis. In **Fig. 2.2**, the effect of an exchange biased system is schematically presented. In **Fig. 2.2 a**, the hysteresis loop of a ferromagnet is shown. It possesses coercive fields that are symmetrical about the zero-point of the magnetic field axis.

The situation changes with the presence of an antiferromagnetic contributor in the system with a Néel temperature T_N. Being above T_N, the magnetic spins inside

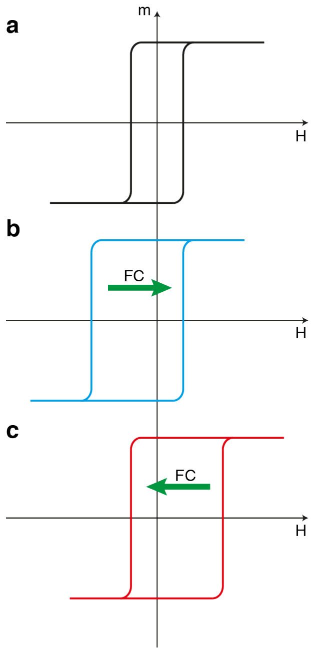

Figure 2.2: Exchange bias effect on the magnetic coercivity. **a**, Magnetic hysteresis loop for a system that has not been field cooled. **b** and **c**, Magnetic hysteresis loops for systems that were field cooled through T_N with either positive (blue curve) or negative (red curve) applied magnetic field during cool down.

the antiferromagnet are disordered, and behave paramagnetic. Upon application of an external magnetic field, the spins align and form the antiferromagnetic anisotropy axis along the direction of the externally applied magnetic field when cooled down through T_N. This process is called field cooling (FC) and allows to pin the uniaxial antiferrmagnetic anisotropy direction. If field cooled into one particular direction with the system being in the temperature range $T < T_N$, magnetic hysteresis loops show a broadening of the coercivity and a shift along the magnetic field axis towards the opposite direction of the applied magnetic field during the FC process (see **Fig. 2.2 b** and **c**). This effect can be attributed to the so called exchange bias effect.

2.2 Materials used for multiferroic tunnel junctions

The important material properties of the metals and complex oxides that were studied in this work will be presented in the following section. First, the used substrate STO will be described, followed by the electrode materials and ferroelectric tunnel barrier materials.

2.2.1 Substrate: strontium titanate

For epitaxial growth it is necessary to start with a monocrystal of about the same lattice constant as the subsequently grown material. The substrate dictates the lattice direction and strain of the following films and thereby influences many physical properties. It is important that a substrate has, if at all, very well known magnetic and electric properties so that the studies on those small effects in the grown heterostructures are not negatively influenced.

$SrTiO_3$ (STO) is commonly used as a starting point for epitaxial growth due to its lattice constant of 3.905 Å, which is close to the in-plane lattice constants of many functional oxide materials (**Fig. 2.3**). One more reason for the wide use of STO is

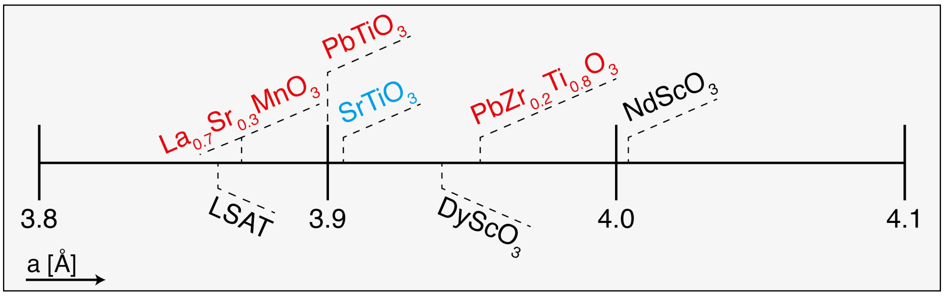

Figure 2.3: Comparison of different perovskites on an in-plane lattice constant scale. The in-plane lattice parameters in units of angstroms of the (bulk) pseudocubic unit cells for the used materials in this work (blue for the used substrate, red for the used thin films) in relation to each other and some additional commonly used materials (black). The linear scale should give an idea of the strain different materials have to experience in order to grow epitaxially on each other.

certainly the possibility to obtain perfect B-site surface termination by etching STO inside a buffered HF solution [35] as it is done for every sample in this work. Electrically and magnetically it can be mostly treated as neutral, especially in its center-symmetric pseudocubic phase. However, STO tends to show flexoelectricity [36] under strain and becomes conductive upon doping with Nb [37], which demonstrates the variety of phenomena that can be induced by small changes in the crystallography of oxide materials in general. STO has even been shown to be a relaxor ferroelectric at low temperatures [38], which makes it interesting for thin film application itself. However, this property does not influence the discussion of phenomena that can be observed on thin films grown on STO as a substrate, which is why it is so widely used. The simple cubic unit cell of $SrTiO_3$, as it is used in this work, results in atomically flat (001) surfaces.

2.2.2 Bottom electrode: Lanthanum strontium manganite

A MFTJ usually consists of three layers, of which two are the conductive and magnetic electrodes that confine the ultrathin ferroelectric barrier. For many reasons such as strain-enhanced ferroelectricity, phase purity and high interface quality, it is important to achieve a well-oriented crystallinity of the tunnel barrier. Therefore, a bottom electrode (the first layer after the substrate) is needed, which has to fulfill the requirements of growing epitaxially and fully strained on STO (001), exhibiting a good conductance and, in case of MFTJs, of being magnetic.

Lanthanum strontium manganite in its stochiometry $La_{0.7}Sr_{0.3}MnO_3$ (LSMO) is the only bottom electrode material that is being used in this work and was chosen because of its magnetic and conductive properties. It is considered to be half metallic with almost 100 % spin-polarization [39, 40], which makes it a good choice for using it as a spin valve, meaning that TMR ratios with LSMO can be expected to be high [41]. The electric transport properties originate from a double exchange process, which correlates conductivity and ferromagnetism [42]. Its crystal structure is rhombohedral in bulk with lattice constants of $a = b = c = 3.87$ Å and $\beta = 90.13°$ [43]. Under tensile strain, as it is the case for thin films of LSMO epitaxially grown on STO (001), the unit cell becomes pseudocubic with an out-of-plane lattice constant of c = 3.846 Å [44].

2.2.3 Top electrodes: Cobalt and copper

Mainly two metals were used as top electrodes that were either, in the case of cobalt, deposited *via* magnetron sputtering, or, in case of copper, thermally evaporated. Cobalt is a ferromagnet with a Curie temperature of $T_{C,Co} = 1150\,°\mathrm{C}$ [45]. Below a temperature of 400 °C cobalt remains in the hexagonal α phase with lattice constants $a = 2.5\,\text{Å}$ and $c = 4.07\,\text{Å}$ [46]. Above 400 °C, it is face-centered cubic.

Copper is a very good, non-magnetic conductor and can be easily evaporated. Capped with a gold top layer it does not oxidize and is thus used as a non-magnetic electrode for reference.

2.2.4 Ferroelectric tunnel barrier: $\mathbf{PbZr}_x\mathbf{Ti}_{1-x}\mathbf{O}_3$

Lead zirconate titanate ($PbZr_{0.2}Ti_{0.8}O_3$ or PZT) is a ferroelectric material with a large out-of-plane polarization value of up to $(105 \pm 5)\,\frac{\mu\mathrm{C}}{\mathrm{cm}^2}$ [47], which can be grown epitaxially on STO *via* pulsed laser deposition [48, 49] up to thicknesses of around 50 nm [50] or more. PZT melts incongruently because of the different melting points of the used binary oxides [51]. In order to obtain the correct film stoichiometry with PLD, the PZT target possesses an excessive amount of lead ($Pb_{1.1}Zr_{0.2}Ti_{0.8}O_3$), which is necessary to even out its high fugacity [52].

Its tetragonal pseudo-cubic lattice parameters are $a = b = 3.953\,\text{Å}$ and $c = 4.148\,\text{Å}$ [53]. When grown epitaxially/strained on STO, it carries 90° and 180° ferroelectric domains, which are accessible by exploiting certain ferroelectric domain switching kinetics that occur for thin films in the order of several tens of nanometers thickness [54]. Due to its mostly covalent bonding nature [55], PZT owns a band gap of $E_{gap} = 3.2 - 3.9\,\mathrm{eV}$ [56], which can thus be regarded as a semiconductor with large band gap. Ferroelectricity is, however, maintained down to thicknesses of 1.2 nm [57] to 1.6 nm [17], and therefore enables the creation of ferroelectric tunnel junctions.

The ferroelectric lead titanate (PTO) is in principle very similar to PZT. It is a perovskite with lattice parameters of $a = b = 3.9\,\text{Å}$ and $c = 4.155\,\text{Å}$ [58] and has in its tetragonal form a ferroelectric polarization value of about $80\,\frac{\mu\mathrm{C}}{\mathrm{cm}^2}$, when grown on STO [59].

In bulk, lead zirconate (PZO) is an antiferroelectric material [60, 61], which undergoes an antiferroelectric-to-ferroelectric phase transition for film thicknesses less than 10 nm [62]. PZO retains an orthorhombic unit cell with lattice parameters $a = 5.88$, $b = 11.787$ and $c = 8.231\,\text{Å}$ [63, 64]. Nevertheless, it is possible to grow thin PZO films strained on STO substrates, exploiting its cubic phase above $T_C = 230\,°\mathrm{C}$ [64]. PZO will be used in this work to create a "digital alloy" structure, to artificially engineer the zirconium content of the ferroelectric tunnel barrier at the cobalt interface (chapter 5.4 on page 67).

2.3 Charge transport

The main focus of this thesis is based on the perpendicular electronic transport through ultrathin ferroelectric films. Although a ferroelectric material is a dielectric, an electric current can be measured for sufficiently thin films and small applied biases. This effect goes back to the quantum mechanical phenomenon of electron tunneling, which is widely exploited in size-crucial applications such as writing and reading very large amounts of data in magnetic hard disc drives. The thickness of an insulating layer can be divided into different ranges in which distinct transport properties become dominant [65]. For thin layers in the $10-20\,\mathrm{nm}$ range, the electronic potential barrier defined by the ferroelectric will mainly be overcome by thermionic injection, a thermally activated current transport effect [66]. In this situation, the energy of (hot) electrons becomes high enough to overcome the potential barrier in the classical sense. For ultrathin films (usually in the sub-10 nm range), electrons are able to tunnel trough an electric potential barrier, possessing potential energies lower than the average potential barrier height [67]. The shape and size of the barrier plays an important role of how the transport mechanism can be described analytically. One can subdivide the tunneling regime into the Fowler-Nordheim ($\approx 5-10\,\mathrm{nm}$) and the direct tunneling (sub-5 nm) range, which is strongly dependent on the applied biases with respect to the tunnel barrier potential shape.

Other contributions to the conductivity in thin ferroelectric oxide films may originate from electroformation processes caused by redox processes (ionic) [68] or metal filament dissolution (metallic pin holes) [69, 70] that are difficult to distinguish from proper quantum tunneling [71]. However, current-voltage characteristics for 2 to 5 nm thin barriers can give rise to the possibility of distinguishing quantum tunneling from parasitic conductivity influences by fitting IV- characteristic curves according to Brinkman [72] and by measuring the resistivity-temperature dependence of the junction [73, 74].

2.3.1 Quantum tunneling

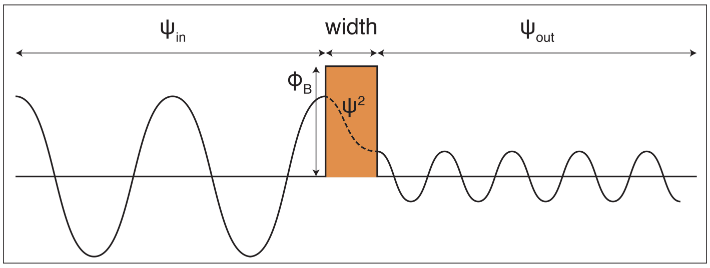

Figure 2.4: Tunneling through an electric potential barrier. This sketch shows qualitatively the wavefunction of an electron propagating from left to right with an energy that is less than the barrier height. Inside the barrier, the square of the wavefunction (the probability density) is plotted, showing a non-vanishing probablity on both sides.

In 1927, Friedrich Hund was the first to describe the (later named) tunnel effect in his work on isomeric molecules [75]. He was able to derive the Schroedinger equation for oscillating nuclei of a molecule's double potential well, in which the potential barrier Φ_B is higher than the eigenvalue of the ground state. One year later it was found that alpha decay could be directly explained by this theoretical model [76], establishing the quantum mechanical description for physical phenomena in other fields. Today, electron tunneling is described by the probability density of its wave function in the quantum mechanical sense [67]. According to this theory, charged particles can propagate through barriers that could not be overcome in the classical sense. As it is sketched in **Fig. 2.4**, the wave function of an electron does not vanish in the wall of an electric potential which is higher than the kinetic energy (E_{e^-}) of the electron itself ($\Phi_B > E_{e^-}$).

The finite probability of an electron with energy E_{e^-} to tunnel through a given barrier in z-direction is described by the transmission coefficient:

$$T = e^{-2\int_{z_1}^{z_2}\sqrt{\frac{2m}{\hbar^2}\left(V(z)-E_{e^-}\right)}\,\mathrm{d}z} \tag{2.2}$$

Where $V(z)$ is the potential barrier, $\hbar$ the reduced Planck constant and m the mass of an electron. This transmission coefficient is derived from the global solution of the wave function coefficients calculated *via* the WKB approximation[1]. Regarding the transmission coefficient, it is already possible to see the exponential dependence of the tunneling probability on the barrier thickness $d = z_2 - z_1$, which is the most influencing factor. Given a bias between the left and the right side of a potential barrier, electrons that tunnel through it are equal to an electric current (-density). The direct tunnel current density j_{DT} for a rectangular shaped barrier is given by:

$$j_{DT} = \frac{4\pi}{\hbar}\sum_{k_t}\int_{-\infty}^{+\infty}\rho_1(E)\rho_2(E+eV)T(E_z)\left[f(E)-f(E+eV)\right]\mathrm{d}E_z \tag{2.3}$$

Here, in z direction, electrons tunnel through a potential barrier with the transmission coefficient $T(E_z)$, coming from a metal with density of states (DOS) of ρ_1 and flowing towards a metal with DOS of ρ_2. f is the Fermi distribution.

An analytical solution for equation 2.3 given triangular, asymmetrically shaped potential barriers of the form $\Phi(z,V) = \Phi_{i1} + \frac{eV}{2} + (\Phi_{i2} - eV - \Phi_{i1})\frac{z}{d}$ is presented in chapter 3.5.1 on page 32.

Another transport mechanism that is based on the phenomenon of electron quantum tunneling is described by the Glazman-Matveev (GM) model [77, 78]. Thermally activated spin-conserving hopping transport through chains of localized states [79] can result in conduction behavior through insulating ultra thin barriers. The GM model delivers the possibility to describe this transport mechanism in tunnel junctions at relatively high temperatures (above 50 K), as it has been shown in literature [80, 81, 82]. The conductance G based on spin-conserving hopping transport through a barrier is described by:

$$G = G_{DT} + \sum_{i=1}^{N} e^{\left(-2\frac{d}{\alpha(i+1)}\right)}T^{\left(i-\frac{2}{i+1}\right)} \tag{2.4}$$

Where G_{DT} is the temperature invariant direct tunnel conductance, d the barrier thickness, N the number of localized states, T the temperature and α the radius of the localized states inside the barrier.

---

[1] The WKB (short for Wentzel-Kramers-Brillouin) approximation is used to find the approximate semi-classical solution for the one-dimensional time-independent Schroedinger equation.

2.3.2 Resistive switching

Resistive switching effects are essential in electric memory and processing circuits. Switching the resistance of a two-terminal device *via* external (small) applied excitations such as electric or/and magnetic fields can lead, on the one hand, to sensing technology in form of HDD reading heads, for example, or, on the other hand, to memory storage in form of M- or FRAMs [83].

2.3.2.1 Tunnel electro resistance

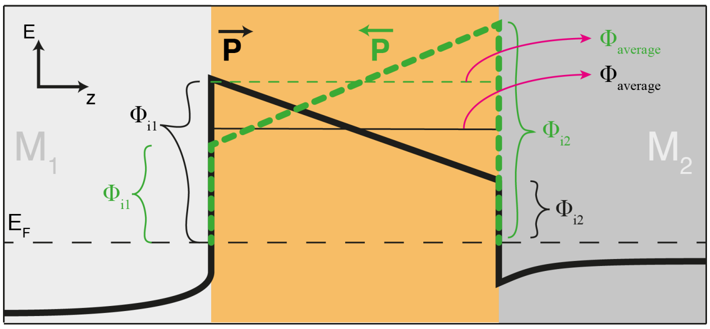

Figure 2.5: Principle of the tunnel electro resistance. Schematics of the electric potential Φ inside a ferroelectric tunnel junction with two different confining metals that have distinct screening lengths with $l_{M_1} < l_{M_2}$. The black-continuous and green-dashed lines are the potential profiles for two opposite ferroelectric polarizations, respectively.

Since 1961, physicists study and apply effects based on electron tunneling through thin insulating layers in Metal-Insulator-Metal capacitors [84], which are essential in modern and future data storage applications [85]. One recent advancement in electrical resistive switching was made by replacing an insulating tunnel barrier by a ferroelectric material [10, 12, 14, 15, 22, 65, 86]. As already discussed, ferroelectrics spontaneously obtain electrical polarity, thus forming an electric potential barrier of asymmetrical shape. As sketched in **Fig. 2.5**, a FE tunnel junction (FTJ) possesses two definite potential shapes (the black and the green lines) that depend on the ferroelectric polarization of the barrier. The triangular shape simply derives from Poisson's equation $\Delta\Phi = -\frac{\rho(r)}{\epsilon}$ and is a result of imperfect screening at the interface of the ferroelectric with the metals. The effective electric field inside the ferroelectric barrier is a superposition of the depolarization field [87] (caused by *ex situ* screening) and the electric field caused by the ferroelectric [12], which is known to be still present down to thicknesses of several unit cells of common FE materials [57, 88].

In order to achieve a symmetry break upon ferroelectric polarization reversal, the two interfaces of the MFTJ must possess contrasting properties: Either different charge displacements on each side of the FE must be induced, which could be obtained by different lattice terminations or introducing spacer layers of a different material; or the electrodes must involve different screening lengths as it is the case in the illustration **Fig. 2.5**, where the screening length of metal one (l_{M_1}) is shorter than that of metal two (l_{M_2}). As already reported, the former mechanism can lead to large resistive switching ratios of 10^4 or higher, due to a spacing layer of STO at one interface [89, 90]. The latter, "electro statical" explanation, was one of the first suggested mechanisms [13] and is commonly used to describe tunnel electro resistance (TER) effects in recent literature [15, 16, 17, 24, 91, 92].

There are other effects that can lead to TER, which are mainly related to strain effects caused by asymmetric ferroelectric switching due to the inverse piezoelectric effect. This will be discussed in detail in the Results chapter 5.2.1 on page 52.

2.3.2.2 Tunnel magneto resistance

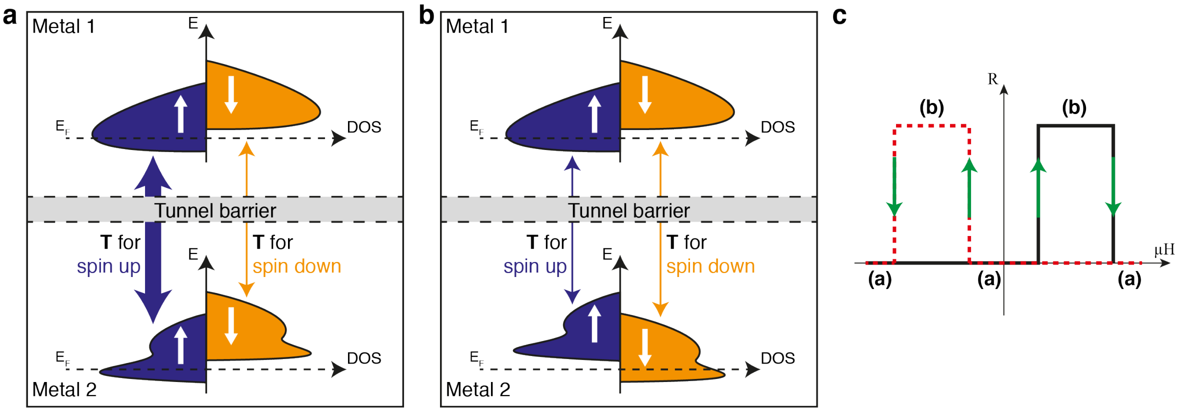

Figure 2.6: Principle of the tunnel magneto resistance. Schematics of the tunnel magneto resistance mechanism. For a tunnel junction comprising two metals and an insulating barrier, the density of states at the interfaces are sketched on either side of the tunnel barrier as a function of the energy for both electronic spin polarizations *up* and *down*, emphasized with the white arrows. Dependent on the magnetization direction of the electrodes in respect to each other (**a** for parallel, **b** for antiparallel alignment), the transmission coefficients T for each electron spin state are shown by the colored arrows, where the tunneling probability is higher for thicker arrow width. **c**, The idealized resistance versus applied magnetic field loop of a tunnel junction with two different magnetic electrodes. The high resistance states correspond to the antiparallel (**b**) alignment, the low resistance states to the parallel alignment (**a**) of the magnetic moments of the electrodes.

Upon separation of two magnetic electrodes by a very thin insulator, which is thin enough to allow direct quantum tunneling of electrons, a tunnel magneto resistance (TMR) effect can be measured that is dependent on the directions of the magnetic moments of the electrodes relatively to each other [93, 94]. The first to discover the fundamental principle of spin polarized tunneling (SPT) were Tedrow and Meservey in 1970 [95]. A large TMR effect at room temperature was, however, first observed by physicists in 1994, among whom Moodera *et al.* [96] were among the first to succeed and thus to contribute significantly to the development of modern memory and field sensing technology. This was conceived and revolutionized by Parkin *et al.* in 1999 due to the introduction of an antiferromagnetic exchange biasing layer [97].

The TMR effect is based on the spin-resolved DOS at the two interfaces that an insulating tunnel barrier possesses with its confining magnetic electrodes. This is the detail, which makes the TMR unique among other magnetoresistive effects such as the giant magnetoresistance [98] and the anisotropic magnetoresistance [99], since it (the

TMR) is not based on spin dependent scattering phenomena. Its principle is solely based on the fundamental probability of direct tunneling of electrons from one state at the tunnel junction interface to the other.

In **Fig. 2.6**, the situation of a magnetic tunnel junction is shown. Assuming two different electrodes in terms of magnetic in plane coercive fields, two different magnetic alignments are possible to realize with an external applied magnetic field. For the parallel alignment (**Fig. 2.6 a**), the tunnel probability, expressed by the transmission coefficient T, is highest for electrons of the same spin state. Recalling that the tunnel current is proportional to T (equation 2.3), the corresponding resistance of each junction is given by the total transmission probability for each spin state. Hence, the resistance of the junction with parallel magnetized electrodes is low compared to that of the junction with antiparallel magnetized electrodes (**Fig. 2.6 b**).

This "normal" TMR leads, in case of an ideal junction, to the characteristic TMR loop as it is shown in **Fig. 2.6 c**. Here, the resistance of a junction is plotted against the externally applied magnetic field. Coming from a defined state of parallel magnetic electrode alignment towards the negative direction (low resistance = **Fig. 2.6 a**), the resistance increases at the weaker coercive field of the corresponding magnetic electrode, since the magnetization of the electrodes is switched into the antiparallel state (high resistance = **Fig. 2.6 b**). Reaching the coercive field of the second electrode with higher coercivity, the electrodes are again magnetized in parallel, but into the opposite direction (positive), which leads to the low junction resistance again. For the negative branch of the loop, the same arguments lead to the characteristic shape.

The ratio TMR_{abs}, which determines the size and sign of the effect is given by equation 3.6 on page 33.

The reason for the less probable tunneling of electrons in the antiparallel aligned magnetization state is that, in order to tunnel from a state A with spin $\uparrow$ into a state B with opposite spin $\downarrow$, the electron spin has to flip, which costs the energy of one Bohr magneton: $E_{flip} = 5.79 \cdot 10^{-5}\,\frac{eV}{T}$. In some cases there are scenarios, however, in which the TMR changes sign ("inverse" TMR, see equation 3.6), which can be attributed to the amount of tunneling s- or d- electrons due to certain interface characteristics of the involved materials [100].

2.4 Memristive systems

Next to the three well known circuit elements "resistor", "capacitor" and "inductor", Leon Chua gave the first theoretical description of a fourth passive circuit element in 1971 that he called memristor [28] (short for memory resistor). The first demonstration of a memristor was performed 37 years later on titanium dioxide-based switches [29]. In principle, a memristor is a resistor that changes its resistance with the amount of electric current that passes through it. The change in resistance is therefore dependent on its own resistance history and is reversible upon change of the current direction.

Apart from the potential to massively improve parallel computing power in form of memcomputing [4, 9], one of the resulting interesting properties of a memristor is simply the ability to store information semi-analogously. The memristance M, which is a measure of resistance, is the state of this system and a function of the state variable w. To bring the system from one state $M(w_1)$ into another state $M(w_2)$, a certain amount of flux has to pass through the two terminals, reading out the resistance as well. Therefore, the state variable itself can be identified as the charge $dw = dq = idt$, whereas i is the current density. For a memory resistor follows then:

$$M\left(q,i\right) = \frac{v(t)}{i(t)} \tag{2.5}$$

This leads to the characteristic pinched I(V) hysteresis curves that are a necessity for memristive systems [101, 102]. Similar to this phenomenon, investigations on the AC dynamics of ferroelectric domains [103] lead to comparable observations of the P(V) hysteresis curves.

2.4.1 Ferroelectric domain kinetics

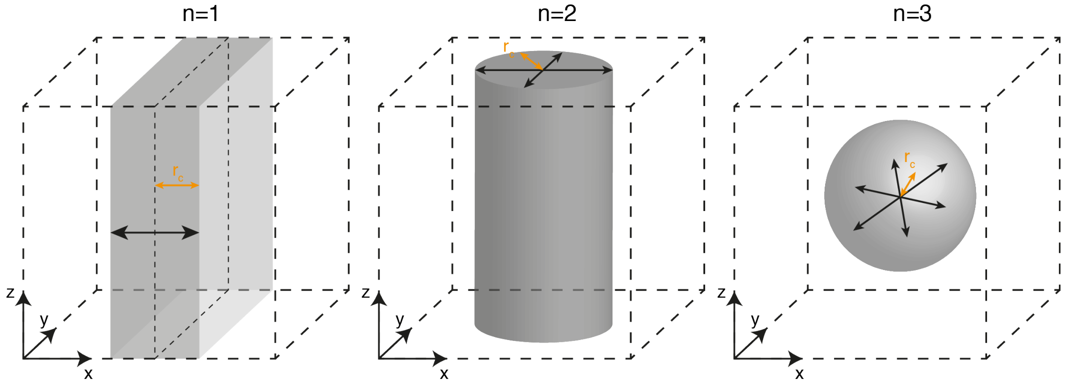

Figure 2.7: Ferroelectric domain wall kinetics. The three possibilities of ferroelectric domain wall motion inside a ferroelectric crystal. The one, two and three dimensional cases ($n = 1, 2, 3$) are sketched inside a cubic crystal. Grey areas demonstrate the oppositely (from the surrounding volume) switched ferroelectric domains, which possess propagation directions towards the directions that are emphasized *via* the black arrows. A representative radius r_c is defined for measuring the volume of the switched domains.

Ferroelectricity in ultrathin-film ferroelectrics is determined, similar as in ferromagnets, by ferroelectric domains. Switching between two polarization states inside a crystal leads to a motion of domains walls (see **Fig. 2.7**) [104] after a random distribution of ferroelectric nuclei [105]. This phenomenon can be well described by a model after Kolmogorov, Avrami and Ishibashi, which is further referred to as KAI model and is explained in the following section.

The volume $V_{sw.}$, which is the switched volume (emphasized by the grey area in **Fig. 2.7**) can be written as:

$$V_{sw.}\left(t,t_0\right) = C\left(r_c + v\left(t - t_0\right)\right)^n \tag{2.6}$$

Where C is a factor, dependent on the dimensionality of the domain wall growth n with $C = 2, \pi$ and $4\pi/3$ for $n = 1, 2, 3$, respectively, and v the domain wall velocity. The starting point, or nucleation, is assumed to happen at an instant time t_0. With the probability $q\left(t\right) = e^{-\int_0^t \mathrm{d}t_0 R(t_0) V_{sw.}(t,t_0)}$ of any point inside the crystal that is not switched at time t, one can define the "extended volume" A [106]:

$$A\left(t\right) = \int_0^t \mathrm{d}t_0 R\left(t_0\right) V_{sw.}\left(t, t_0\right) \tag{2.7}$$

with the nucleation rate $R\left(t_0\right)$ and time t_0 per unit time per unit volume. The fraction Q of the switched volume to the total volume is dependent on the probability $q\left(t\right)$ and can be written with use of eq. 2.7 [107] as:

$$Q\left(t\right) = 1 - q\left(t\right) = 1 - e^{-A(t)} \tag{2.8}$$

From there on, two cases have to be distinguished, where the first case, *Category I*, is determined by a constant nucleation rate and the second case, *Category II*, by just an initial nucleation of ferroelectric nuclei, which is then followed up purely by ferroelectric domain wall propagation.

As mentioned before, ferroelectric domains grow in thin films *via* domain wall propagation after initial nucleation (in a time window of Δt_0) [105], and thus *Category II* is the important one for this thesis, since only ferroelectric films of ultrathin thicknesses are studied.

In this case, A deduces to $A\left(t\right) = \left(\frac{t_c + t}{\tau}\right)^n$, with $\tau = \left(CR_0 \Delta t_0 v^n\right)^{-1/n}$ for a constant nucleation rate R_0 and $t_c = 0$ for the initial condition $r_c = 0$ at $t = 0$. It follows then for the fraction Q:

$$Q\left(t\right) = 1 - e^{-(t/\tau)^n} \tag{2.9}$$

Given a capacitor, which confines a very thin ferroelectric film between two metal electrodes, the only directions for ferroelectric domain walls to propagate are in the plane. Equation 2.9 simplifies in this case to:

$$Q\left(t\right) = 1 - e^{-(t/\tau)^2} \tag{2.10}$$

In this two-dimensional case, the ratio of ferroelectric domains that are polarized "up" to the domains that are polarized "down" is the fraction $P_{\downarrow}\left(t\right)/P_{\uparrow}\left(t\right)$. Defining the saturation polarization to be $P_S = P_{\downarrow}\left(t = t_S\right)$ (t_S is the time, when the whole film is fully polarized down), one can normalize the polarization value to be $P_{norm}\left(t\right) = \frac{P_{\downarrow}(t)}{P_S}$, which is the same fraction as $Q\left(t\right)$ (see eq. 2.10). It follows:

$$P_{norm}(t) = 1 - e^{-(t/\tau)^2} \tag{2.11}$$

Since the polarization of the sample changes with an electric field, the dynamics of the ferroelectric domain walls are given by the time t during which the electric field is applied and its amplitude (voltage), which defines the characteristic "decay" time τ. Equation 2.11 is thus a function of the applied pulse time and amplitude, which defines the domain ratio of the ferroelectric thin film.

2.5 X-ray magnetic circular dichroism and synchrotron radiation

A way to measure magnetism in condensed matter is to use magneto optical (MO) interactions. Already observed in 1845, the Faraday effect describes the rotation of the polarization vector of transmitted linear polarized light in the visible light spectrum through a magnetic material, which could later be reproduced on a variety of metals with light in the soft X-ray range [108]. Based on the same physics, but using different geometries, the magneto-optical Kerr effect (MOKE), was found in 1877. With this method, it is possible today to distinguish between in-plane (L/T-MOKE) and out-of-plane (P-MOKE) magnetic moments of a sample surface [109, 110]. Proposed much later in 1975 [111] and realized in 1987 [112], the first MO effect with circular polarized light in the soft X-ray range (X-ray magnetic circular dichroism: XMCD) was observed. This opened the path for utilizing synchrotrons, which are specialized to deliver the high brilliance needed for element-selective magnetic measurements using polarized light.

2.5.1 Creation of synchrotron radiation

Synchrotron radiation is created *via* the acceleration of charged particles (i.e. electrons) perpendicular to their trajectory. This can be achieved by magnetic fields (with so called bending magnets) that force electrons on trajectories with a radius of $r = m_e \frac{v_c}{eB}$[1] around a ring (storage ring). With high relativistic velocities, the electrons emit light focused into a small cone with an opening angle of $1/\gamma$, where $\gamma = \frac{E_e}{m_e c^2}$ is the electron energy in units of rest mass $m_e c^2 = 511\,\text{keV}$.

At the synchrotron BESSY II in Berlin, the storage ring holds an electron beam in multibunch mode[2] at an energy of 1.7 GeV with bending magnets applying 1.3 T, which forces the electron trajectory into an arc with a radius of $r = 4.35\,\text{m}$. The resulting radiation is mostly confined to the synchrotron plane and is linearly polarized.

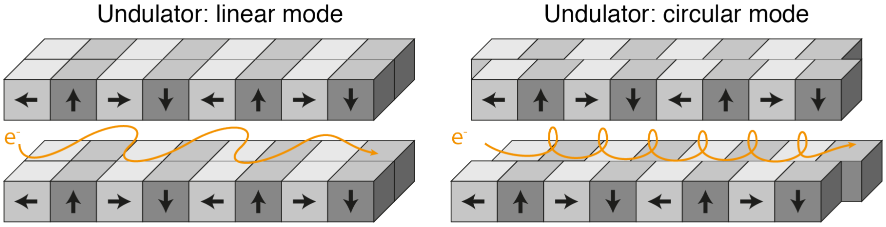

Figure 2.8: Schematics of an undulator. Magnet arrangement of an undulator in linear light polarization mode (left) and circular light polarization mode (right), where the magnets are shifted with $\lambda/4$ against each other. The orange line is the trajectory of the electrons.

To achieve even larger brilliance and to obtain circular light polarization without losing intensity, insertion devices, so-called undulators, are used. In principle, an undulator forces the electron beam during its path through a straight segment of the synchrotron into a sinusoidal motion *via* an arrangement of magnets (see **Fig. 2.8**). This motion creates a coherent superposition from all oscillations, which leads to an intensity increase that scales with the square of undulator periods N^2. By shifting the magnet arrangement of the undulator by $\lambda/4$, the magnetic field inside the gap is helical, creating a spiral trajectory of the electrons that emit circular polarized light this

---

[1] Derived from Lorenz force compensation $F_L = F_Z$, where F_Z is the centripedal force.

[2] A continuous injection mode that allows an almost constant light intensity.

way. The helicity of the emitted light $\sigma^{\pm}$ can thus be chosen, while the light intensity stays unaffected.

2.5.2 X-ray magnetic circular dichroism

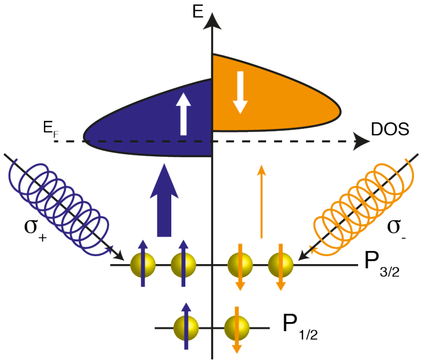

Figure 2.9: Principle of X-ray circular dichroism. Schematics of the absorption of left and right circular polarized X-rays by the $2p$ states of $3d$ metals. The colored arrows indicate the strength of the absorption coefficients $\mu_{\pm}$, being larger for thicker arrow width.

Circular polarized light is used for MO methods to measure magnetism in solid state matter. With the so called resonant magnetic scattering (XRMS) method, it is possible to measure X-ray magnetic circular dichroism (XMCD), which element-selectively allows to probe magnetism of a material composition. XRMS is a measuring technique that is based on the specular reflection of the X-ray beam on the sample (usually within angles of a few up to 40°) for the case when the energy of the photons is close to an absorption edge of one of the elements $h\nu = E_n - E_i$, where the initial and intermediate atomic states are E_i and E_n, respectively.

For $3d$ metals, the resonant absorption of circular polarized X-rays is illustrated in **Fig. 2.9**. The degeneracy of the $2p$ states is lifted by the spin-orbit coupling into the $2p_{1/2}$ and $2p_{3/2}$ core levels. The absorption of circular polarized light in case of the $2p_{3/2} \rightarrow 3d$ transition (at the so called metal $L_{3,2}$ edges) is explained by the dipole selection rules [113] and Clebsch-Gordan coefficients and will not be further discussed here.

The resulting absorption coefficients $\mu_{\pm}$, however, are dependent on the circular light polarization helicity $\sigma\pm$. For the XMCD fraction follows:

$$\text{XMCD} = \frac{\mu_+ - \mu_-}{\mu_+ + \mu_-} \tag{2.12}$$

This fraction means that the measured signal with XRMS depends on the helicity of the incoming polarized X-rays, leading to a measurable contrast, which proves magnetism. Additionally, the absorption coefficients underlie symmetric principles that allow to measure magnetic hysteresis loops in reflection *via* an externally applied magnetic field.

These symmetric principles of the contrast mechanism can be used to measure XMCD without the actual inversion of the circular polarized light helicity. Therefore an external magnetic field is applied that saturates the magnetic material into the corresponding directions.

As it is shown in **Fig. 2.10**, the measured intensity signal contrast of reflected polarized light is identical for the two cases presented in the parts **a** and **b** of the figure, which can be seen on the thickness of the vertical arrows that stand for the absorption

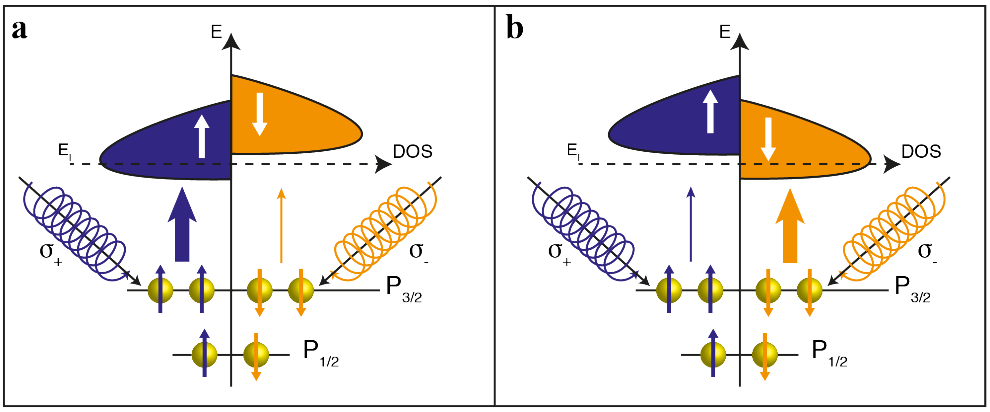

Figure 2.10: Constant field versus constand helicity XRMS signal. The scheme illustrates the DOS of a magnetic material that is split into spin up and spin down parts. The magnetization of the material is reversed between the two cases **a** and **b**, leading to a symmetric redistribution of the spin resolved DOS. The X-ray circular polarized light is visualized by pointing and spiral vectors that emphasize the helicity. The thicknesses of the colored vertical arrows indicate the absorbtion strength of the corresponding circular polarized light of certain helicity.

strength of the corresponding light helicity. These cases resemble the two magnetically saturated orientations where the minority and majority electron spins change roles. If the symmetry of beam intensity upon helicity reversal and DOS distribution upon magnetic field sign reversal is granted[1], it follows that the contrast of a measured reflected light intensity with opposite helicity and constant magnetization $I_{\sigma+,M_+}/I_{\sigma^-,M_+}$ is precisely the same as the contrast with constant helicity but reversed magnetization direction $I_{\sigma^+,M_+}/I_{\sigma+,M_-}$.

In principle, it is possible to quantify the arrangement of atomic orbitals *via* other techniques like total electron yield measurements and the use of sum rules. These methods, however, were not possible to apply to the grown samples, and are thus not a matter of further discussion here.

2.6 Summary of the chapter

In this chapter, all investigated ferroic materials have been presented with focus on their ferroic and structural properties. To understand the presented transport data that were measured on multiferroic tunnel junctions, the theory of quantum tunneling was recalled and the theoretical model for direct tunnel current through asymmetric, triangular potential barriers was motivated. The two resistive switching phenomena ”tunnel electro” and ”tunnel magneto resistance” were discussed with focus on a few possible explanations that were studied in the framework of this thesis. The definition of the later used term ”memristor” was introduced and the necessary theoretical background of ferroelectric domain wall kinetics was given, which is crucial for the understanding of the ”programmable ferroelectric tunnel memristor” [114] that was

---

[1] This is absolutely the case, since the elliptical undulators of the BESSYII facility work with extremely good precision.

created in this work.

The very basic principles of the conducted synchrotron experiments were presented, involving the creation of high intensity X-rays and the fundamentals of magneto optical coupling phenomena.

3

Methods and sample preparation

A considerable part of the work was devoted to the growth and characterization of the investigated samples. The implementation of *in situ* growth observation *via* RHEED (Reflection High Energy Electron Diffraction) played a crucial role in order to produce controlled terminations, defined film thicknesses and for growth parameter optimization. In this chapter, the used methods are listed in the same order in which the actual characterization processes were executed.

3.1 (Ultra-) thin film growth and structuring

To grow (ultra-) thin film samples, the respective material must first be transferred from the material source to a substrate. The transported material, which is usually in the gas or plasma phase during the transport process, must then condensate at the substrate surface, ultimately resulting in the deposition and growth of the film.

3.1.1 Pulsed laser deposition (PLD)

In **Fig. 3.1**, the main setup used for pulsed laser deposition is sketched. Here, a laser beam is directed *via* laser optics to a source, which is the so called target. The impact of the beam into the target creates a plasma (plume) [115], that transfers the target material to the substrate (usually of size $5 \cdot 5 \cdot 0.5\,\mathrm{mm}^3$), where it condensates at the surface and forms the film. The created electric field at the impact spot of the laser must be high enough to remove potentially conducting electrons, allowing the laser to penetrate the target with around $\approx 100\,\mathrm{nm}$ depth [116]. The evaporated material gets thermalized through the environmental gas (usually oxygen with a pressure of around 0.1 to 0.3 mbar) and forms the plasma plume [115]. The properties of this plume (stoichiometric distribution, size, density etc.) are dependent on parameters such as focus area and surface roughness of the target. The laser beam is pulsed with repetition rates between 1 and 50 Hz, which enables the control of certain growth characteristics such as the nucleation rate of the deposited material at the substrate surface.

This relatively common method must be separated from the laser deposition method that is based on high local energy dissipation of the laser beam in the focus area at the target surface, which thermally evaporates material. Thermal laser deposition is used for metallic material transfer and is called laser ablation and deposition (LAD) [117,

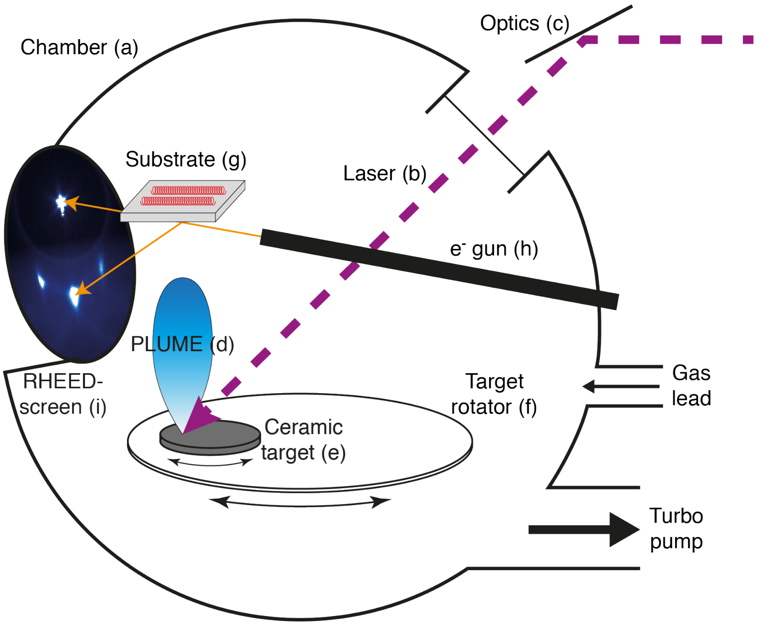

Figure 3.1: Pulsed laser deposition system. **a** Vacuum chamber with a base pressure down to $5 \cdot 10^{-7}$ mbar. **b**, $\lambda = 248$ nm excimer laser, based on KrF with a pulse width of 20 ns, a maximum repetition rate of $f = 50$ Hz and maximum power output of $W \approx 1.5$ J per pulse. **c**, Laser optics including aperture for beam profile forming. **d**, Resulting plasma (plume) from a laser pulse impact. **e**, Ceramic target. **f**, Target rotator for eccentric movement of the targets, enabling almost 100 % target surface coverage. **g**, Substrate holder with three degrees of freedom for RHEED positioning including a heating coil, capable of heating the substrates up to 850 °C. **h**, Electron gun as part of the *in situ* RHEED system with an acceleration voltage of 25 kV and beam current of 30 mA. **i**, Electron sensitive fluorescence screen for detecting the direct, diffracted and reflected electron beams.

118, 119]. Laser light with a wavelength of $\lambda < 300$ nm gets mainly absorbed by metals, because it lies below the plasma edge $\left(\lambda_p = \frac{c}{2\pi}\left(\frac{N \cdot e^2}{\epsilon_0 \cdot m_{eff}}\right)^{-1/2}\right)$ of common metals. In principle it is suitable for *in situ* follow-up deposition of metals after functional oxide deposition. However, because the power of the laser radiation must be large enough and dissipated in a short enough time to greatly overcome the evaporation point of the respective metal before it can transport the heat efficiently over the whole target volume, high laser fluencies (Energy per focus area) of minimum $2\,\frac{\mathrm{J}}{\mathrm{cm}^2}$ are necessary. The homogeneity of the focus spot must be extremely even, because droplet formation at the substrate surface becomes an issue otherwise [117]. These were some of the reasons why *ex situ* deposition of metal top electrodes was performed *via* other methods, which will be addressed later in this chapter.

In general, PLD possesses certain advantages over other growth methods with a relatively small amount of compromises that have to be taken into account. Some of the key features are certainly the nearly 100 % stoichiometric material transfer from a designated oxide target to the substrate and the possibility to grow oxide thin films in true layer-by-layer[1] (LBL) mode with possibly unmatched surface and interface sharpness [120]. Certain known exceptions of non-stoichiometric material transfer, however, can be easily overcome by oversupply of lead in $Pb(Zr_{0.2}Ti_{0.8})O_3$, for example. [121]

PLD allows the epitaxial growth of material compositions with well-defined doping levels by simply choosing the corresponding ceramic substrate. Additionally the used chamber enables the successive *in situ* growth of up to four different material compositions due to a target rotation system (**Fig. 3.1 e** and **f**), which can switch between different ceramic targets relatively fast. This also allows the growth of superlattices [122].

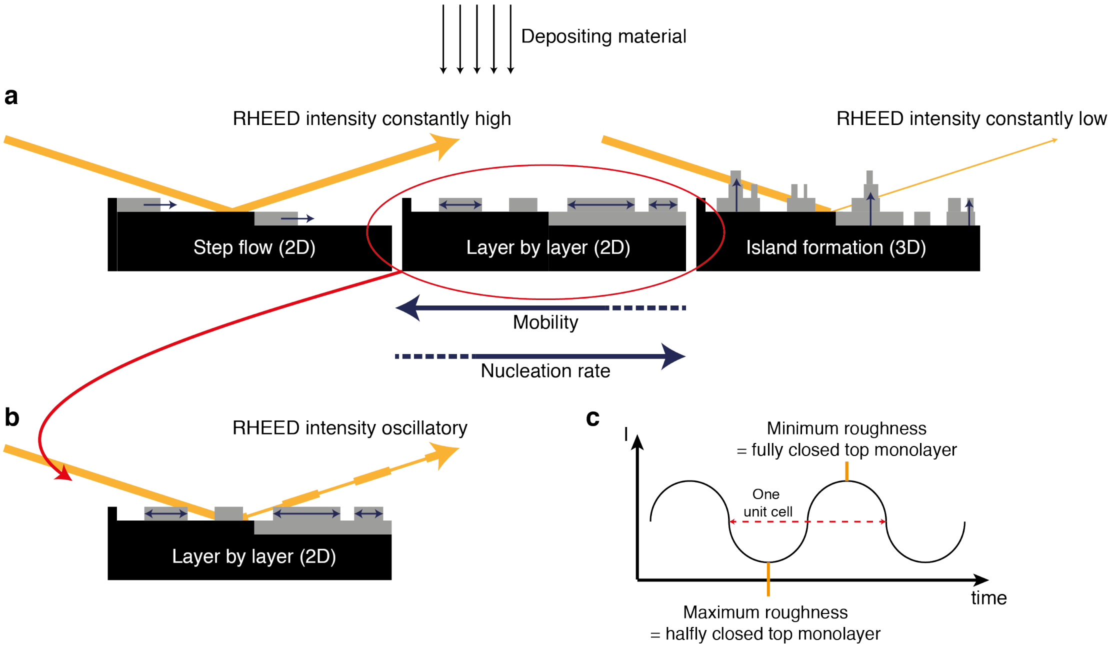

Figure 3.2: Growth modes and RHEED. a, Scheme of the three mainly distinguishable growth modes from left to right: Step flow-, layer by layer-, and 3D growth. The grey areas represent the adatoms that are deposited and already bound to the substrate. The arrows inside indicate the dominant growth direction. Orange arrows should demonstrate the electron beam (with exaggerated angle), that is reflected at the surface and thus leads to a constantly high or low intensity signal, depending on the growth mode. **b**, For the special case of layer-by-layer growth the intensity of the reflected electron beam is oscillatory as a function of time/layer-filling, that is sketched in the intensity versus time schematics (**c**).

Depositing functional oxides *via* PLD leads in general to three different growth modes that can be distinguished. Depending on the nucleation rate and the mobility of the deposited surface atoms at the substrate, the dominant local growth direction can be in-plane or out-of-plane. For high nucleation rates, the growth direction is out-of-plane, resulting in rough surfaces. For very low nucleation rates, the opposite is the case, which is referred to as step-flow-growth. From the epitaxial point of view, step-flow-growth is the best choice in order to obtain best possible, epitaxially strained

---

[1] Also named after Frank-van der Merwe.

films. However, in order to observe RHEED oscillations (discussed later), it is desirable to obtain a mixture of both (LBL growth mode). In **Fig. 3.2 a** the growth direction of the deposited material is illustrated by arrows inside the grey areas. Choosing the right parameters to obtain LBL growth can be very difficult to achieve. The crucial parameters and their effect on the growth mode and crystal quality in terms of roughness are: The laser fluency, which increases the nucleation rate with increasing laser power; the laser repetition rate, which mainly determines the ablation (and growth) speed and can thus influence the quality of epitaxy and growth mode; the substrate temperature, which defines the kinetic energy of deposited atoms, resulting in faster nucleation for lower temperature; the environmental gas (oxygen) pressure, mainly influencing the atomic arrangement of the deposited atoms, resulting in strong roughness and epitaxy dependencies [123]; the distance between substrate and target, which defines the thickness homogeneity of the ablated films across the substrate surface.

A main advantage of the used chamber over simpler PLD equipment is the installed RHEED system, which allows the *in situ* observation of the growth mechanism, surface quality and growth rate, and ultimately enables the control of complex oxide growth with an accuracy down to the single unit cell [124, 125, 126]. As it is illustrated in **Fig. 3.1 h, i** and **Fig. 3.2**, an electron beam (introduced through a differentially pumped vacuum pipe into the chamber) gets reflected at the substrate surface and directed to a fluorescence screen. Using a high sensitive CCD camera on the opposite side of the screen, it is possible to selectively measure the brightness of a chosen fluorescence spot of the RHEED pattern. According to the reciprocal lattice description of diffraction, the brightest intensity spot is the $(0,0)$ constructive interference spot, resulting from the crossing of the Ewald sphere with reciprocal lattice rods on the 0th Laue circle (mirror reflection) [127] (see **Fig. 3.3**). The horizontal distance between two reflection points on the Laue circle corresponds to the $2\pi/b$ lattice constant, which is of course equal to $2\pi/a$ in a tetragonal system. The distance $d_{h,k}$ is given by symmetry and the incident angle of the incoming electron beam with respect to the sample and thus enables in principle the investigation of the lattice structure *in situ*.

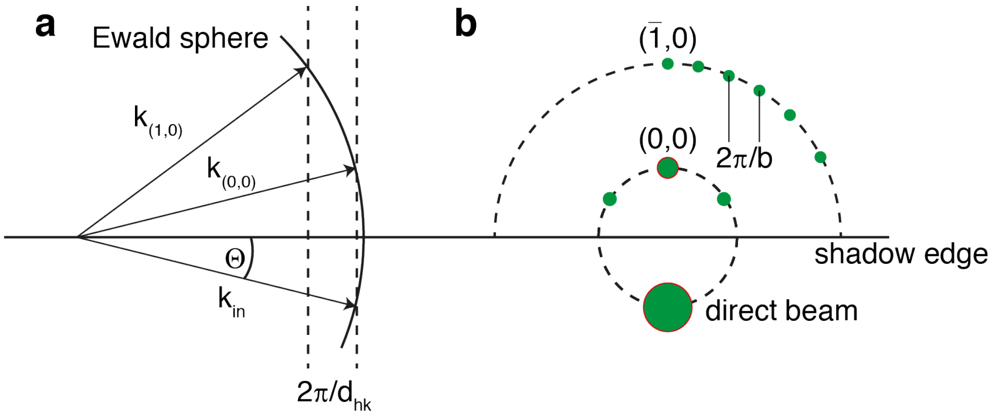

Figure 3.3: RHEED principle. **a**, Crossing point of the Ewald sphere with the reciprocal lattice rods of distance $2\pi/d_{hk}$ resulting in the **k** vectors of constructive interference. **b** On the perimeter of the resulting Laue circles, the different diffraction spots are visible. The difference in intensity is emphasized by the size of the green dots, becoming smaller for larger Laue circle numbers.

The intensity of the mirror reflection is directly dependent on the roughness of the surface. Hence it allows to observe layer-by-layer growth that possesses a maximum roughness when the topmost unit cell is half closed and a minimum roughness when it is fully closed, resulting in oscillatory behavior of the intensity (**Fig. 3.2 c**). The wavelength between two intensity maxima corresponds to the events of two successive full closures of the surface, which can be translated into a thickness gain of exactly one unit cell. Counting the number of maxima is therefore a reliable method to know the deposited film thickness with best possible accuracy, and even allows to stop the deposition right at the point when the topmost layer is completely closed and possesses maximum flatness. To see proper RHEED intensity oscillations, however, the incident angle Θ must be chosen to be as small as possible.

Obviously, the deeper investigation of the RHEED pattern would also allow the study of lattice constants, width of terraces and the quantification of the surface roughness, but as a rule of thumb, grown films are perfectly flat when the RHEED spots lie on the Laue circles. This behavior could always be confirmed with a subsequent investigation *via* AFM to study the surface morphology.

The time dependence of the intensity of the $(0,0)$ reflection point after a depositing laser pulse allows to study the surface adatom kinematics. Extensive studies on that allowed the optimization of thin film quality for oxide films due to the development of the "interval deposition" [128].[1]

In **Table 3.1**, suitable PLD growth parameters for the used oxide materials have been summarized. It should be acknowledged that every PLD chamber possesses different characteristics, for example the way how and where the oxygen pressure and the substrate temperature is measured, or variations of the uniformity of the focused beam profile, which leads to certain plasma plume characteristics. This could lead to significant deviations from the presented growth parameters.

Material	**Fluence** $\left[\frac{\mathbf{J}}{\mathbf{cm^2}}\right]$	**Rate** [**Hz**]	**Temp.** [°**C**]	$\mathbf{O_2}$**-pressure** [**mbar**]
LSMO	1	$1-2$	600	0.15
PTO	0.5	4	600	0.2
PZO	0.5	4	600	0.2
PZT	1	5/50*	575	0.28

Table 3.1: PLD growth parameters for the used materials. The repetition rate for PZT, marked with * is used for the interval deposition technique.

3.1.2 Magnetron sputtering and patterning of cobalt electrodes

To create cobalt top electrodes after the growth of functional oxide materials, the samples were immediately transferred into a designated growth chamber with a magnetron sputtering unit. The magnetic cobalt top electrodes were grown *via* this technique, which delivered excellent results in terms of interface quality between the oxides and the metal (see chapter 4.4 on page 45).

---

[1] Used and presented later in chapter 4.3.1 on page 39.

The base pressure for growing metals with this technique reached down to $2 \cdot 10^{-7}$ mbar. With a dissipated power of 20 W, an argon plasma was used at a pressure of $2.5 \cdot 10^{-3}$ mbar to deposit the cobalt material. The deposition rate was relatively fast with around $4\,\frac{\text{nm}}{\text{s}}$. Deposition was conducted at room temperature. The magnetic properties of the Co films were measured *via* SQUID at temperatures of 5 K and room temperature (see chapter 4.5 on page 46) and with XMCD at room temperature (see chapter 7.1 on page 86).

3.1.3 Thermal evaporation

The non-magnetic top electrode material copper and the eventual capping layer of gold were both deposited *via* thermal evaporation inside a growth chamber with a base pressure of down to $5 \cdot 10^{-7}$ mbar. Al_2O_3-covered tungsten boats and coils were used, enabling deposition rates of around $0.2\,\frac{\text{nm}}{\text{s}}$. The growth rate could be monitored with a piezo-driven quartz crystal monitor with good accuracy. Confirmation of the film thicknesses were carried out *via* a profilometer from Asylum.

To create patterned copper electrodes, the metals (including the gold capping layer) were deposited through a shadow mask with grid size of around 60 μm. This made an additional etching and lithography step unnecessary for this type of samples. The thickness of the layers were usually 20 to 40 nm for copper, whereas gold was *in situ* deposited within the thickness range of around 15 to 20 nm.

3.1.4 UV light lithography patterning of cobalt electrodes

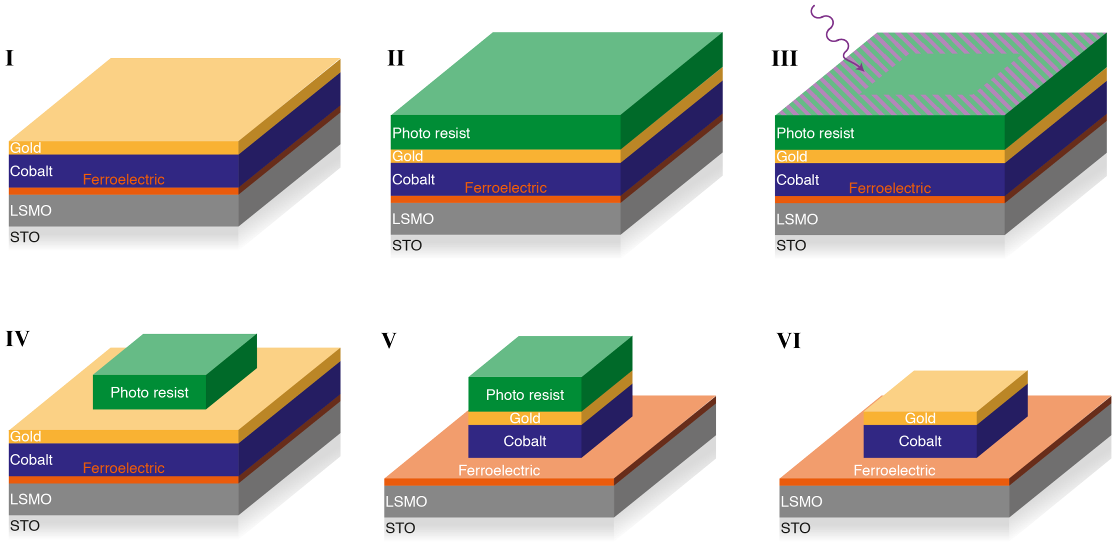

Figure 3.4: UV-light lithography. Scheme of the five steps to pattern top electrodes of variable sizes, using potassium iodide etchant to selectively etch the top electrode metals. (I) Virgin sample. (II) Adding a layer of photo resist. (III) Exposing the (positive) photoresist at the designated areas. (IV) Selective etching of photo resist. (V) Selective etching of metal films. (VI) Removing of the photo resist.

Tunnel junction devices are mostly fabricated in capacitor geometry with the surface normal pointing out of plane of the films. This is the easiest geometry to reliably create large amounts (e.g. hundreds) of devices from one single sample, and can be achieved with a single fabrication process.

After the *in situ* growth of the complex oxide films and the following deposition of the cobalt and gold top layers, the whole area of the substrate surface is covered by a homogeneous heterostructure of layers. The following patterning steps are summarized in **Fig. 3.4**. The freshly grown sample (I) is covered with a positive photo resist[1] (II) using a spin coater (6000 rpm, for one minute) and then baked at 95 °C for one minute. A quartz-chromium mask with the desired pattern is then brought into contact with the sample *via* a special mask aligner. UV-LED light sources then illuminate selected areas of the photo resist (III). The development of the photo resist film is carried out in a bath of special developer[2] (IV). A diluted potassium iodide solution ($KI : H_2O \rightarrow 1 : 10$) was then used to etch both the gold and the cobalt selectively, which took around five seconds (V). Eventually, the remaining photo resist was removed with acetone and isopropanol (VI).

3.2 Surface analysis

Atomic force microscopy (AFM) methods were used to either visualize surface roughness and step terrace width or to measure the ferroelectric response of films *via* a technique called piezoforce microscopy (PFM), which is a modified version of the AFM.

Since these techniques are not the main focus of the presented work and several members of the working group at the MPI were specialized on these particular topic, they will just be mentioned and not described in detail.

3.2.1 Atomic force microscopy

At its heart, the principle of AFM is based on leverage. A tiny signal becomes physically magnified *via* a laser beam reflected from the back of a small cantilever. The ratio of the length of the laser beam path to the length of the lever is directly proportional to the magnification. Hence a tiny bending of the lever, caused by a small sensation of the atomically sharp AFM tip, leads to a measurable deflection of the laser beam with a photodetector.

The tip of the cantilever is brought into contact with a surface *via* piezoceramic actuators, which are highly responsive and very accurate. In the dynamic contact (or tapping) mode, which is the one used in this work, the actuators drive the cantilever with a frequency close to its eigenfrequency. The electronic circuit of the AFM is able to adjust the piezoactuators according to a differential change in the amplitude of the oscillating cantilever and thus keeping it constant. The vertical actuator movement, which is a result of following the change in distance between the surface and the cantilever, is the measuring signal. This enables the measurement of a height profile (topology), by moving the AFM tip over a surface in a rasterized way.

The vertical resolution of the used AFM[3] is with less than 0.2 Å more than sufficient

---

[1] The used photo resist is AR-P 3510 from Allresist.

[2] The used developer is AR 300-35, also from Allresist. The solution for a developing step was $H_2O : AR \rightarrow 1 : 1$ and the developing time was one minute.

[3] Digital Instruments 5000 AFM with silicon tips.

to measure step heights of atomically flat surfaces that are a result of the substrate off-cut angle. The size of the AFM images was usually set between $2 \cdot 2\,\mu\mathrm{m}^2$ and $10 \cdot 10\,\mu\mathrm{m}^2$, with a scan frequency of 2 Hz per raster line.

3.2.2 Piezoforce microscopy

With a conductive AFM tip[1], it is possible to apply an electric bias between the tip and a back electrode in contact mode. If a piezo- or ferroelectric film lies between the tip and the electrode, the applied electric field leads to the inverse piezoelectric effect and thus to a local deformation of the material or even to a ferroelectic polarization switching for fields being larger than the ferroelectric coercive field (see chapter 2.1.1 on page 3). To illustrate the ferroelectric 180° out-of-plane domains of PTO, PZT and PZO/PTO, a driving AC bias applied to the FE film induces a piezoelectric response, which can be analyzed in terms of phase shift and amplitude.

Simultaneously, a DC bias can be applied to the tip in order to additionally switch the ferroelectric film at the location of the AFM tip. With this technique it is possible to write ferroelectric domains into a film. In **Fig. 4.9** on page 44 an image of such a manipulated (ultra) thin ferroelectic film is presented. In that case, the ferroelectric domains have been written into the ferroelectric thin film during the scan and afterwards read out with the PFM. The proof of ferroelectricity is the 180° phase shift of the measured PFM signal between regions of oppositely polarized FE domains.

In fact, for measurements on ultrathin films (in the tunneling thickness regime), a method called DART-mode PFM was employed, using a MFP-3D microscope from Asylum Research. In this mode, the PFM AC bias frequency follows the resonance frequency of the piezoelectric actuation of the film *via* dual AC resonance tracking (DART), resulting in a signal-to-noise ratio that is several magnitudes larger than for normal PFM. This is especially important, since for ultrathin films the tip bias leads to a leakage tunnel current, which does not allow to produce large piezoelectric amplitudes to effectively image ferroelectric domains. Additionally, relatively small AC excitation amplitudes of around 100 mV can be applied that, on the one hand, certainly do not switch the FE polarization, and on the other hand do not create too large currents, which might destroy the local chemistry of the films due to heat dissipation.

3.3 Structural investigations

Epitaxy of the grown films is very important to achieve reproducibility and high interface quality. Hence the structural characterization of the films was important.

3.3.1 X-ray diffraction

For macroscopic structural analysis, a Philipps X'Pert MRD, Typ 3050/65 x-ray diffractometer (XRD meter) with an angle resolution of $\delta 2\Theta \approx 0.3°$ was used. The x-rays are created with the wavelength of the characteristic copper K_α-line $\lambda\,(Cu_{K_\alpha}) = 1.541\,\text{Å}$ *via* deceleration of an electron beam (50 kV and 30 mA) by a copper target.

---

[1] Here, diamond coated (and doped) tips were used for that purpose.

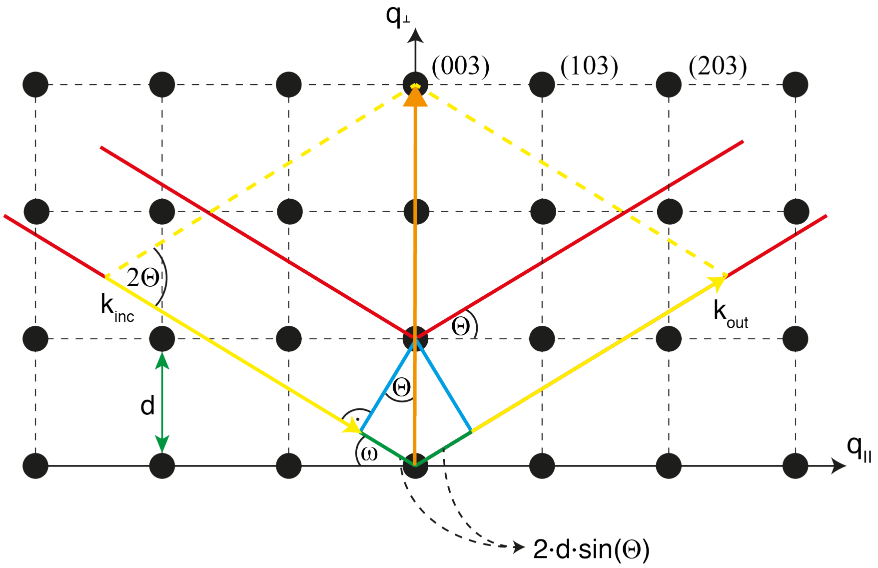

Figure 3.5: XRD principle. Scheme of a cubic two dimensional lattice in reciprocal space. The yellow lines indicate the incoming and outgoing **k** vectors of the x-ray beam. The colored lines emphasize the geometry of the Bragg-equation. The $q_\perp$ and $q_{||}$ resemble the c- and a/b directions in the crystal lattice, respectively.

The particular wavelength of the created photons is important, because it has to be in the same order of magnitude as the interatomic distance in condensed matter lattices (crystals) to make the Bragg-equation applicable:

$$2 \cdot d_{hkl} \cdot sin\,(\Theta) = \lambda \tag{3.1}$$

This equation gives the angle dependence for the constructive interference direction in relation to the photon wavelength. Hence it is possible to obtain information about interplanar spacings d for planes with Miller indexes (hkl). To scan the plane spacings in the $q_\perp$ direction of a sample, a $2\Theta - \omega$ scan has to be performed (see **Fig. 3.5**). Here, the angle ω, which is the angle of the incoming x-ray beam with respect to the $q_\perp$ lattice planes of the sample and the angle 2Θ are moved simultaneously in a way that the sum of the vectors k_{inc} and k_{out} scans along the c-axis of the reciprocal lattice. Intensity maxima occur then at the $(00l)$ lattice points, where l is called the order of the reflection. The measured 2Θ angles, at which reflections exist, give rise to the out-of-plane lattice constant c of the investigated crystal. With known lattice constants, such as for the used STO substrates, the calculated reflections must be used to calibrate the angles 2Θ and ω with respect to the lattice by an offset angle $\Delta\omega$ to obtain maximum intensity at the reflections.

A way to obtain the in-plane lattice constants is to measure reciprocal space maps (RSM). With this method, reflections with $(h0l)$ number are chosen (for instance (203)). If a heterostructure possesses multiple reflections around the area of a known substrate $(h0l)$ peak, a reciprocal space map can give the information about whether grown films are epitaxial with respect to that substrate. A reciprocal space map is in general a composition of $2\Theta - \omega$ scans along one direction of the map and a $\Delta\omega$ scan into the perpendicular direction of it. The lattice constants in- and out-of-plane can be calculated by:

$$a = h \cdot \frac{d}{sin\,(\Theta - \omega)} \tag{3.2}$$

$$c = h \cdot \frac{d}{cos\,(\Theta - \omega)} \tag{3.3}$$

3.3.2 Transmission electron microscopy

One of the best methods to locally investigate interfaces is the transmission electron microscopy (TEM). With electron energies that are high enough, thin samples of cross sections (lamellas) are transparent for an electron beam. Due to the interaction of through-passing electrons with the lattice atoms, a contrast can be measured in bright field mode (measurement of the electrons that went through the sample undiffracted) and in dark field mode (measurement of the diffracted electrons).

The lamellas were fabricated using a focused ion beam (FIB) of the company FEI, allowing to investigate specific areas of a sample and positioning of several lamellas to one holder.

For the atomically resolved characterization an aberration-corrected (Cs probe corrector) FEI TITAN 80-300 analytical scanning transmission electron microscope (STEM) was used, allowing a spatial resolution of about 0.8 Å in the HREM and STEM mode as well. Applying a high angle annular dark field detector (HAADF) in the STEM mode, elastic, thermal diffuse scattering (TDS) events can be recorded. The intensity of these localized, incoherent scatter processes is roughly proportional to Z^2, and thus, the position of atom columns is imaged with a brightness related to their atomic number Z. This is usually referred to as Z-contrast technique.

3.4 Electric and magnetic measurements

The main chapter of this work (chapter 5 on page 49) is based on transport measurements through tunnel junctions, which were carried out in-house with the available facilities. Element selective magnetic measurements, however, have been done at the synchrotron facility BESSYII in Berlin in collaboration with Dr. Radu Abrudan, who supervised the experiments there and helped with the data analysis.

3.4.1 Cryoprobing station with built-in superconducting magnet

Most of the measurements on multiferroic tunnel junctions were performed in a LakeShore TTP4 probing station with a variable superconducting magnet for fields of up to 1 T that could be applied in-plane with respect to the sample holder. The helium flow cryostat allowed stabilized temperatures down to 5 ±0.005 K. The temperature adjustment was performed *via* the helium flux through a needle valve and a PID controlled heater.

The electrical connection of a tunnel junction was realized *via* a tungsten probe that was brought in contact with the top electrode and circuited over the back-contact through the LSMO electrode, which was connected to a copper sample holder (see

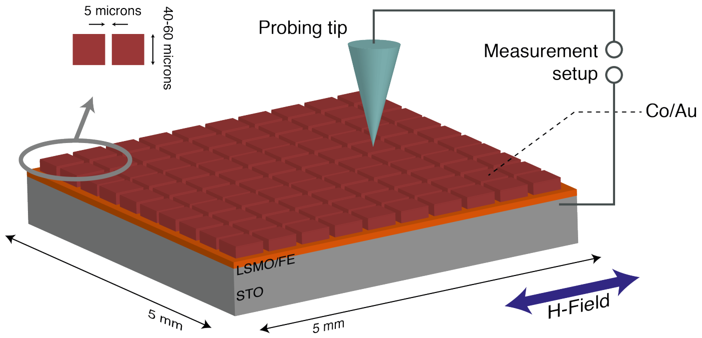

Figure 3.6: Sketch of the probing station. The patterned devices (red) are contacted *via* a tungsten probe. The backcontact is realized *via* the LSMO thin film, which is contaced *via* silverpaste at the edge and accordingly implemented into the circuit. The magnetic field lies in-plane and along one of the crystallographic axes of the sample.

Fig. 3.6) with silver paste. The positioning of the probe was performed *via* a digital microscope with large working distance and the probe manipulator, allowing tiny adjustments to balance out thermal stress-induced movement during cool down.

3.4.2 TER and TMR measurement setup

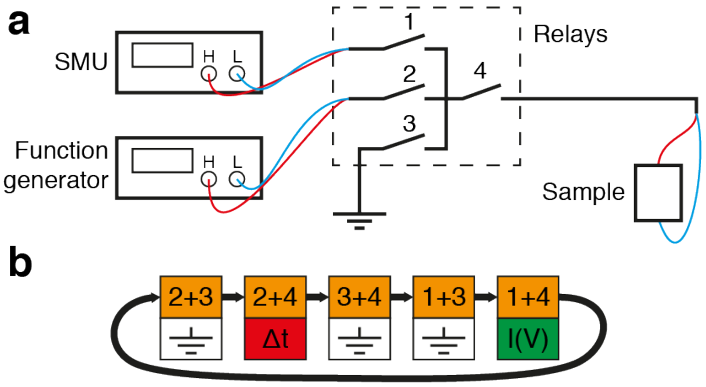

Figure 3.7: TER and memristor measurement schematics. Schematics including a sketch of the circuit at the top of the figure, and a block diagram of the programmed measuring loop. (SMU - Source meter unit).

The transport measurements of a connected junction underwent usually the loop of events that is displayed in form of a block diagram in **Fig. 3.7 b**. With a Model 7022 Matrix-Digital I/O Card from Keithley (resembles the relays in **Fig. 3.7 a**) and a specially designed break-out-box that was manufactured at the electronic workshop of the MPI, a variety of circuits and program routines could be realized (see **Fig. 3.7 a**). With this particular setup, it was possible to measure very small currents due to its ground-potential free design, which otherwise would produce too much noise. As a function generator, a SONY Tektronix AFG 310 with a voltage rise time of less than twenty nanoseconds was used. To measure the $I(V)$ characteristics of a junction, a Keithley Series 2600A System SourceMeter with an accuracy of 0.035% (current programming accuracy at room temperature) and a resolution of down to 50 pA was built into the setup.

To measure the $I(V)$-curve of a junction after a certain voltage pulse, the function generator was first grounded for 0.2 s and short-circuited to allow any potentially built up charge to neutralize (2+3). Then, it was connected to the sample (2+4) in order to apply the programmed pulse, which was always of rectangular shape. After grounding both the sample and the source meter unit (SMU, (3+4) and (1+3)), the SMU was brought into contact (1+4) with the sample to perform a voltage sweep (usually in the range of $\pm 200\,\mathrm{mV}$) and simultaneously measure the flowing current. The grounding step was always carried out for the same reason as before, not allowing any built up charge to influence the ferroelectric domain distribution inside the sample.

The software used to conduct the fully automated measurements (especially those for the memristor measurements in chapter 6 on page 77) and record the data was Testpoint version 1.2. All the programs have been written to meet the special needs of each individual measurement, but followed similar routines of grounding and measuring the samples. Built up charges were expected to occur from thermal gradients of the leads into the cryostat and from radio frequencies due to electric background noise inside the lab.

Magnetic transport measurements were carried out "on the fly", which means that a constant voltage was applied to the sample with continuous current readout, while the magnetic field of the cryostat swept through the programmed field ranges. The measurement speed was therefore determined by the ramping speed of the magnet and the integration time of the SMU. For one magnetic field sweep of $0\mathrm{mT} \rightarrow -200\mathrm{mT} \rightarrow 200\mathrm{mT} \rightarrow 0\mathrm{mT}$, the measurement took around ten minutes. During that time, the temperature of the cryostat had to be stabilized so that no movement between the probing tip and the top electrode of the sample occurred.

3.4.3 Physical property mesurement setup

For the lateral transport measurements on LSMO in chapter 4.2 on page 36 in Van der Pauw geometry [129], and for the temperature dependent measurement of the tunnel conductance in chapter 5.1 on page 50, a physical property measurement setup (PPMS) from Quantum Design was used. With this PPMS magnetic fields of up to 9 T could be applied within a temperature range between 1.9 and 400 K.

3.4.4 Synchrotron setup

The XRMS measurements at BESSYII in Berlin have been carried out at the bending magnet beamline PM3 using the diffractometer ALICE, a modular and mobile chamber with variable magnetic field and temperature. An energy range of 20 eV to 1.2 keV is accessible with this setup, which is suitable to measure the $L_{2,3}$ edges of the investigated elements in this work. The monochromator possesses an energy resolution of around $\Delta E/E \approx 1 \cdot 10^{-4}$ and a degree of circular polarization of about $P_C \approx \pm 95\,\%$ can be achieved *via* the undulator.

To measure samples inside ALICE, they first had to be aligned in order to measure proper 2Θ reflectivity scans. This was done by choosing the $L_3 = 780\,\mathrm{eV}$-edge of cobalt, which was in some cases only a patch of $0.5 \cdot 0.5\,\mathrm{mm}^2$ area in size (see **Fig.**

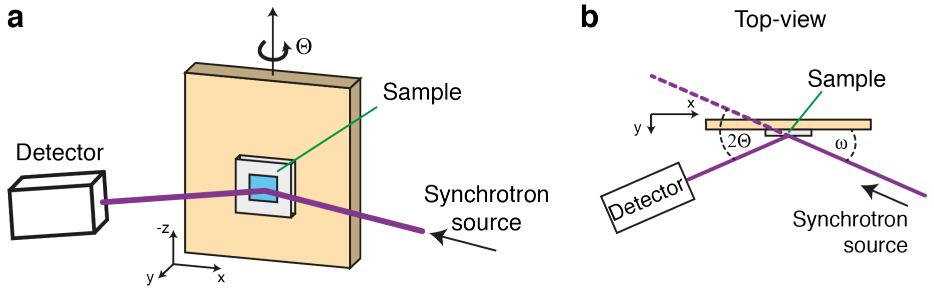

Figure 3.8: ALICE setup for XMCD measurements. a, Measurement geometry: Detector and X-ray pointing vector in relation to the sample. **b**, Top-view of **a** in order to visualize the respective angles for the reflectivity measurements.

7.1 in chapter 7 on page 86). The scheme in **Fig. 3.8** sketches the setup situation. The roughly estimated positions of the respective cobalt patches on the samples were used to pre-align the to-be-measured patch into the beam. At the $2\Theta = 0°$ position and with blanked-out sample (far away from the x-ray beam), the direct x-ray beam was then aligned to be in the center of the photo diode inside the detector to calibrate the beamline with the instrument. By bringing in the sample (moving it along the y-direction), partial blanking of the x-ray beam, detected by a decrease in the measured intensity, enabled the correct positioning of the sample along the y-axis. Upon blanking about half of the beam intensity, ω-rocking scans were used in order to determine the correct positioning of the sample/patch along the x-axis. After the correct alignment of x- and y position, the angle 2Θ was increased with $\omega = \Theta$ upon an angle of around $2\Theta = 5°$. A repetition of ω-rocking scans enabled then, in reflection, the optimal adjustment of an offset angle $\Delta\omega$ *via* intensity maximization. Staying in reflection, the sample was centered along the z-axis as well.

The XRMS reflectivity scans at constant photon energy were performed by gyration of the detector of 2Θ and the sample of Θ plus the constant offset of $\Delta\omega$, during which the measuring signal was constantly read out. The conventional magnet inside the chamber always stayed in the same position with respect to the sample, which allowed the application and modulation of an in-plane magnetic field at all reflectivity angles. For the $\sigma_{\pm}$ measurements, the reflectivity scan was conducted incrementally with a small angle variation $\Delta 2\Theta$ at which a magnetic field of ±100mT was applied successively. Energy spectra were recorded at constant reflectivity angle and *via* monochromator-ramping through the desired photon energy range. To obtain XRMS energy spectra, two energy sweeps have been performed during which the applied magnetic fields, of opposite sign each, were constantly applied.

3.5 Analytical methods

The methods to calculate certain physical parameters from $I(V)$-characteristics and to plot TMR curves are summarized in the following chapter.

3.5.1 Fitting of the tunnel current-voltage characteristics with the Brinkman model

In the direct tunneling regime, $I(V)$-characteristics can give rise to several parameters that are important for studying the electric and dimensional properties of tunnel junctions. It is used in cases of direct tunneling (DT) and where the tunnel barrier has not a simple rectangular shape, but possesses triangular characteristics. The Brinkman model [72] can deliver information about the thickness of a tunnel junction d, the effective electron mass m_{eff} and the work functions at the boundaries of the electric potential barrier to the metals $\Phi_{i1,i2}$ ($i1$ is the top, $i2$ the bottom interface of the FE tunnel barrier).

The analytical expression that was used to fit the $I(V)$ data of the tunnel current through the measured junctions was developed by Gruverman *et al.* [15] and is given by:

$$j_{DT} = C_1 \frac{Exp\left[C_2\left(\left(\Phi_{i2} - \frac{eV}{2}\right)^{\frac{3}{2}} - \left(\Phi_{i1} + \frac{eV}{2}\right)^{\frac{3}{2}}\right)\right]}{C_2^2\left(\sqrt{\Phi_{i2} - \frac{eV}{2}} - \sqrt{\Phi_{i1} - \frac{eV}{2}}\right)^2} sinh\left[\frac{3eV}{4}C_2\left(\sqrt{\Phi_{i2} - \frac{eV}{2}} - \sqrt{\Phi_{i1} + \frac{eV}{2}}\right)\right] \tag{3.4}$$

With $C_1 = -\frac{4em_{eff}}{9\pi^2\hbar^3}$ and $C_2 = \frac{4d\sqrt{2m_{eff}}}{3\hbar(\Phi_{i1}+eV-\Phi_{i2})}$, where e is the electron mass and V the applied voltage. The measured data (current) was calculated into the current density j with $j = \frac{I}{A}$, where A is the area of the tunnel junction capacitor. Using Mathematica[1], global minima for the data sets were found *via* the "NMinimize"[2] method in the "FindFit" function. The fitting parameters though needed to possess starting values inside certain boundaries in order to prevent overflows in the computation. The boundaries were chosen reasonably but were given enough freedom to not purposely design the result. Those boundaries were for the effective electron mass: $0.1\,\mathrm{m}_e < \mathrm{m}_{eff} < 2\,\mathrm{m}_e$, for the work functions: $0.1\,\mathrm{eV} < \Phi i1, i2 < 3\,\mathrm{eV}$, and for the potential barrier thickness: $0.5\,\mathrm{nm} < \mathrm{d} < 10\,\mathrm{nm}$. More refined boundary conditions were used in cases of very similar data sets of identical samples in order to considerably decrease the response time of the computation.

3.5.2 Normalizing of the tunnel magneto resistance

To normalize TMR loops, the zero crossing point was taken as reference. The percentage of TMR was always calculated as follows:

$$\mathrm{TMR}\,(R) = \frac{R - R_{ref}}{R} \cdot 100 \tag{3.5}$$

where R is the junction resistance and R_{ref} the corresponding reference resistance point. The absolute value of the TMR though is given by:

---

[1] Software version 8.0.

[2] The setting used was "DifferentialEvolution", which delivered highly accurate results in a reasonable time.

$$\mathrm{TMR}_{abs} = \frac{R_{\rightleftharpoons} - R_{\Rightarrow}}{R_{\rightleftharpoons}} = \frac{2\, P_{DOS,1}\, P_{DOS,2}}{1 + P_{DOS,1}\, P_{DOS,2}} \tag{3.6}$$

where TMR_{abs} is the absolute TMR value, $R_{\rightleftharpoons}$ and $R_{\Rightarrow}$ the resistances for antiparallel and parallel magnetization directions of the top and bottom electrodes, respectively. The $P_{DOS,i}$ are the electron spin polarizations at the electrodes $i = 1, 2$, which are dependent on the density of states (DOS) at the Fermi level (Jullière-model [93]).

3.6 Summary of the chapter

As a complementation to the Fundamentals chapter on page 3, the Methods and sample preparation chapter should have described the way of how the acquired and discussed data in this thesis have been obtained.

The methods of sample creation have been addressed with a particular emphasis on PLD and the possibility of *in situ* growth control *via* RHEED, which was used heavily to design and reproduce the measured tunnel junctions. Critical parameters have been pointed out and the applied knowledge in order to approach certain problematics has been presented. The other used growth methods (sputtering and thermal evaporation) have been shortly addressed for completion.

The way of top-down structuring of the devices *via* UV lithography has been shown and characterization methods have been described: The three different microscopy techniques, AFM, PFM and TEM were illustrated and some limitations have been pointed out in the context of ultrathin film characterization; For structural/crystal-lattice investigations, the macroscopic method XRD was outlined, which should make the understanding of some reciprocal space maps easier.

The most important part of this chapter is probably the description of the measurement setups. It is condensed to the basic principles of the mechanisms, which should, however, give enough detail to reproduce any of the following measurements. Especially the circuit schematics of the TER and TMR measurement setup, which was designed as a modular addition to the cryoprobing station and the PPMS, would be too complex to draw in detail while preserving the understanding of the essential measurement steps.

Being partly addressed in the Fundamentals chapter, the synchrotron setup in its XRMS geometry was discussed and the way of aligning and measuring samples was presented.

To reveal the way of how the measured data were treated, especially the fitting and simulations that will be shown in a later chapter, the analytical section focused on the software and keyalgorithms that were used in order to analyze the data.

4

Growth and characterization of the materials

Interface quality is a key property in order to obtain tunnel junctions. For that reason characterization and growth optimization of the used materials were important elements in the framework of this thesis. Crystallographic, interface and ferroelectric properties of thin films underwent certain characterization procedures of XRD, TEM and AFM, respectively. However, not all measured samples have a complete set of characterization data. This is due to the fact that interface morphology studies with AFM, for example, were not possible to obtain *in situ* between the depositions of different materials. In this case, reference samples with a certain material termination have been grown to be able to access the surface morphology. Nevertheless, with help of RHEED patterns, reasonably good prediction of surface morphology could be achieved *in situ*.

Although the main focus of this thesis lies on the physical understanding of the obtained results, it is also necessary to mention some paths that led into dead ends in order to prevent certain mistakes to happen again to potential followers.

4.1 Importance of $SrTiO_3$ substrate surface quality for subsequent interfaces

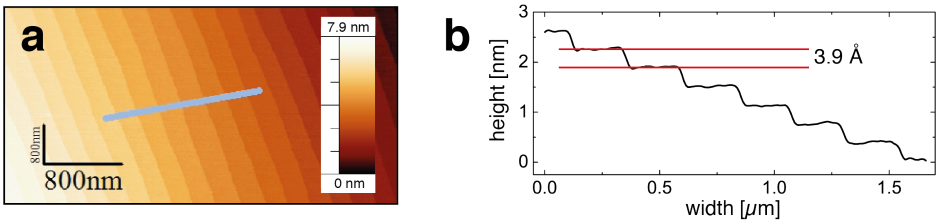

Figure 4.1: Strontium titanate morphology a, AFM image of the STO surface, showing the morphology after etching and annealing. **b**, Height profile along the grey line in **a**.

Right from the manufacturer (Crystec GmbH Berlin), substrates come with an offcut angle in respect to their (001) surface. This leads to step terraces at the surface of 100-500 nm width and step heights of exactly one unit cell (3.905 Å). In **Fig. 4.1 a**, step terraces of a treated [35] B-site terminated STO substrate are shown on an AFM picture. Following the grey line inside the figure, the height profile in **Fig. 4.1 b** shows step heights of 3.9 Å, which proves the uniform termination.

However, as a consequence of mixed termination, resulting from poor STO treatment, the morphology of an eight unit cell thick $PbTiO_3$ film is demonstrated *via* AFM measurements in **Fig. 4.2**. This surface quality is not suitable for being used as a tunnel junction for apparent reasons.

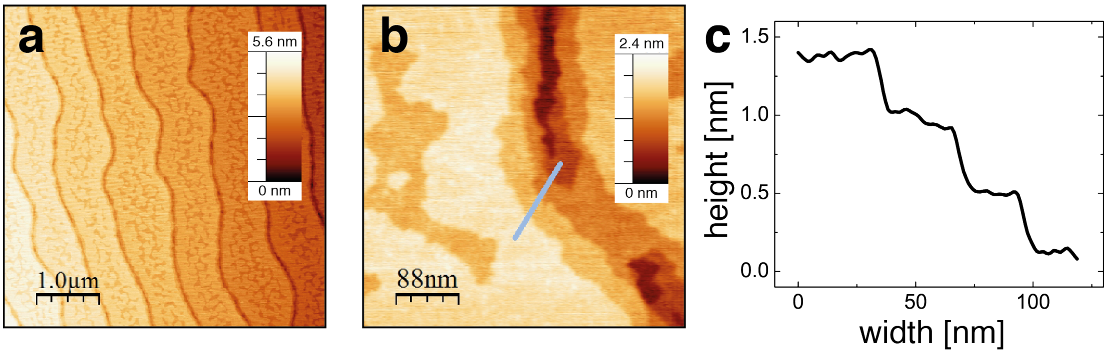

Figure 4.2: Surface morphology for $PbTiO_3$ grown on mixed terminated STO. **a** and **b**, AFM pictures of the topmost surface of a STO/LSMO/PTO structure. At the beginning of each step, fissures of 4 or more unit cells are visible, which can be seen on the profile (**c**) along the grey line in **b**.

In this case, one can clearly see fissures of about 2 nm depth and approximately 80 nm width (**Fig. 4.2 b**). A height profile (**Fig. 4.2 c**) of the $PbTiO_3$ surface emphasizes that the depth of one fissure is in the magnitude of the ferroelectric film thickness itself. Although the morphology of the ultrathin $PbTiO_3$ layer most certainly resembles the interface morphology of the underlying bottom electrode material (LSMO), and thus could possess a homogeneous thickness distribution nonetheless, big variations in the film structure itself make it complicated to use simple modeling of capacitor geometries. A step-like structure like this would lead to a complex current density distribution within the capacitor as a result of electric field-strength variations at the observed fissures. This could produce a lower than expected resistance of a FTJ of known thickness. As it will be demonstrated later on, by using substrates of very good quality with single termination, this kind of fissure texture was not observed anymore.

4.2 Growth and properties of the $La_{0.7}Sr_{0.3}MnO_3$ bottom electrode

Growth of LSMO *via* PLD showed signs of layer-by-layer growth. During the deposition, up to 100 RHEED oscillations could be followed, which enabled the possibility to stop at an intensity maximum after the desired thickness was reached. Although the polar discontinuity of LSMO films at the surface can lead to unwanted reconstructions [130], the complete filling of the top-most layer minimizes the surface energy and might

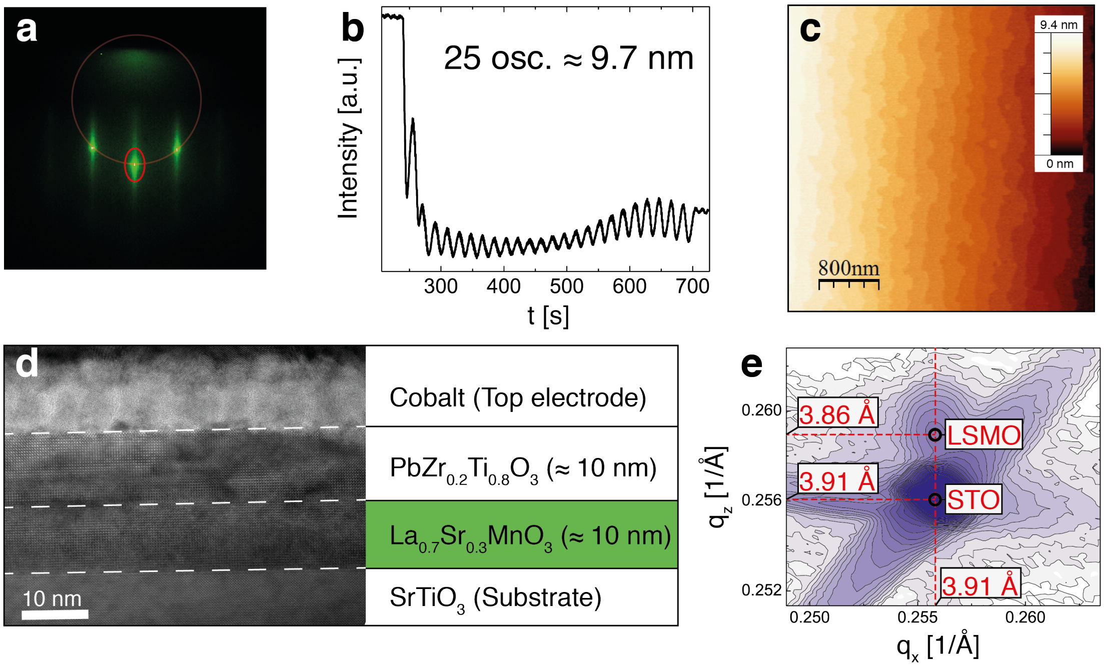

Figure 4.3: Exemplary lanthanum strontium manganite morphology and structure. **a**, RHEED pattern of a LSMO surface immediately after deposition. The big red circle's perimeter lies on top of the intensity spots, which emphazises that the surface roughness is very low. The area marked with the small ellipse indicates the intensity measuring area. **b**, Specular reflection intensity measurement over time during deposition of the material. The oscillations are counted and correspond to the growing thickness of the film. **c**, AFM picture of a typical LSMO surface morphology after growth on STO. **d**, TEM image and lokal thickness measurement of the same structure shown in **a** and **b**, consisting of LSMO and PZT grown on STO. **e**, Reciprocal space map of a LSMO film on STO around the (103)-reflection. The red lines indicate the intensity centers of STO and LSMO, the number values inside the figure are given by the reciprocal of the q-values for the respective directions q_x or q_z.

therefore help to prevent double termination without further engineering. In **Fig. 4.3**, a sheet of figures for structural data analysis during and after the growth is presented for a 10 nm thick LSMO film. During its growth, RHEED oscillations were visible and pronounced enough to easily stop at a local maximum of the intensity curve (**Fig. 4.3 b**). With the value for the c-lattice parameter, taken from the RSM measurement in **Fig. 4.3 e**, the thickness of the film was calculated to 9.7 nm, which can be confirmed by the TEM thickness measurement in **Fig. 4.3 d**. The good agreement of both thickness measuring methods shows that the counting of RHEED oscillations can be used as a reliable thickness control of LSMO thin films. The slight difference of the thickness values can have multiple reasons. One reason lies for sure in the nature of TEM investigations. The thickness of thin films can only be measured very locally, whereas the RHEED method gives a more averaged thickness value of the whole sample. Given the fact that the plume during PLD is quite narrow, the thickness of the deposited film is thicker in the center of the sample and, averaged, thinner than the TEM investigation of a center part of the structure. To show the morphology of a typical LSMO surface in **Fig. 4.3 c** an AFM image of the latter is presented. In this case, the growth parameters were the same but the usual follow up of another oxide layer was not performed. The reassembly of terraces with step heights of 3.905 Å again proves a single terminated surface.

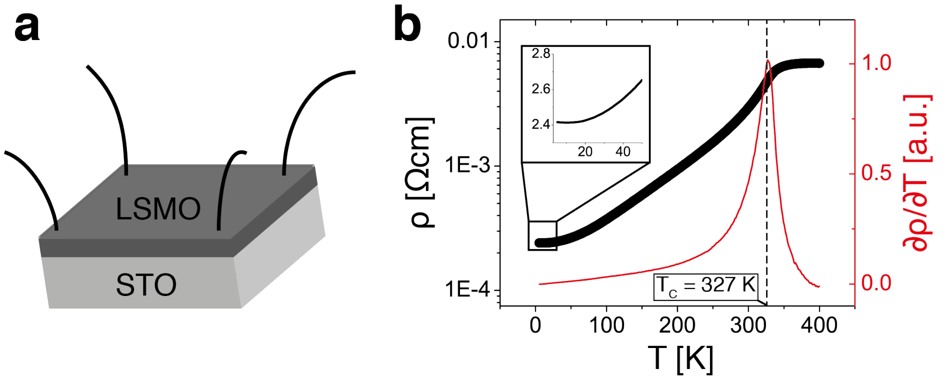

Figure 4.4: Electrical properties of LSMO. a, Scheme of the sample with four contact wires at the corners. **b**, Logarithmic plot of the measured resistivity ρ (black curve) and linear plot of the derivative $\delta\rho/\delta T$ (red curve) against the temperature. The maximum of the red curve occurs at a temperature of $T_C = 327\,\mathrm{K}$. The inset shows a magnification of the lower-temperature part of the curve.

Lanthanum strontium manganite bottom electrodes were chosen to be in the thickness range of $20 - 30\,\mathrm{nm}$. This mainly results from the fact that the sheet resistance declines for conductive thin films with increasing thickness. As the measured tunnel capacitors are to be treated like a serial resistance of tunnel junction and bottom electrode, the resistance-contribution of the bottom electrode should be as small as possible to not dominate the electrical measurements. The LSMO resistivity was therefore measured with the method of Van der Pauw [129]. By exploiting the rectangular shape of the sample, it is possible to obtain ρ by attaching four wires at the outmost corners of the sample as it is sketched in **Fig. 4.4 a** and measuring the resistance in different geometries. In **Fig. 4.4 b**, the resistivity ρ is plotted logarithmically versus temperature for a 20 nm thin LSMO film together with the derivative $\delta\rho/\delta T$. The maximum of the derivative curve is very well pronounced and indicates the ferromagnetic phase transition of LSMO at a Curie temperature of 327 K. The correlation between the drop in resistivity and the ferromagnetic phase transition in LSMO can be explained by the reduction of carrier scattering by thermal spin fluctuation [131], which can be understood within the double exchange theory. The minimization of the relative t_{2g} spin angle $\Delta\Theta_{ij}$ due to the ferromagnetic spin arrangement leads to an increase of the carrier mobility. The measured value of $T_C = 327\,\mathrm{K}$ is lower than reported bulk values, which are slightly higher than 350 K [44, 132].

4.3 Growth of the ferroelectric tunnel barriers

Of crucial importance is the high quality of the tunnel barriers. A good method of thickness control is necessary to create tunnel junctions with a high yield and reliable reproducibility. *In situ* RHEED controlled growth is absolutely necessary to produce samples of comparable thicknesses, because slightly varying laser fluence, substrate-sample distance and other minor factors add up to sometimes significant errors regarding the ablated material per laser pulse. This does not necessary lead to worse growth quality of the eventually grown films, but *in situ* thickness control is nevertheless the only reliable way to investigate and compare several types of MFTJs with different FE tunnel barrier material of the same thickness, as it is done at a later point in this thesis.

4.3.1 Lead zirconate titanate

Following the chronological progress of work that was performed in order to study multiferroic tunnel junctions, the optimized growth parameters and characterization of PZT thin films are presented in the following section. Ferroelectric tunnel barriers should have a thickness of several nanometers only, but for interface studies *via* synchrotron radiation it was necessary to grow relatively thick films of PZT, which is from a certain perspective rather more difficult than growing just several unit cells. On the one hand, the crystal structure tends to relax with increasing thickness at around 50 nm, which leads to a reduction of the tetragonality [133] and thus to a decrease of the ferroelectric polarization value [50]. On the other hand, although it is possible to grow PZT in layer-by-layer mode for relatively thick films up to 90 nm [47], the overall roughness becomes large (RMS of 1.66 nm in **Fig. 4.5 b**), making it hard to see any RHEED oscillations for more than 8 unit cells (**Fig. 4.5 a**). This could result from competing nucleation and reconstruction phenomena that take place at the same time. As a result, for ultrathin films and films in the 50 nm-range, two different growth methods had to be found that both give the best possible interface morphology and the opportunity to control the thickness *in situ*.

Growth kinetics can be considerably influenced by the deposition rate per pulse, i.e. the laser energy fluence, and the overall deposition rate, given mainly by the laser pulse repetition rate (ablation frequency) f. Of course other parameters like substrate temperature, substrate step-width [134] and oxygen pressure [123] are of similar importance, but since heterostructures are grown *in situ*, those parameters were preferably only changed in small values in order to allow a rapid follow-up of the next epitaxial deposition. To optimize the surface morphology for PZT films of several tens of nanometer thickness and still being able to control growth speed, an interrupted rapid ablation technique, called "interval-deposition" growth [128], was applied. As an example, in **Fig. 4.5** the latter method is compared to the continuos growth method. RHEED intensity, morphology and ferroelectric behavior are presented: The upper row shows the data for continuos ablation of PZT with a constant ablation frequency $f = 5$ Hz, and the lower row for the interval-deposition growth, respectively. During interval-deposition the material is ablated with the highest possible (in this case 50 Hz) ablation frequency. The number of laser pulses of each burst with high f delivers the amount of material needed to deposit one monolayer which was calibrated by measuring the thickness of a reference sample *via* TEM, that was grown with the continuos method. The assumption was made that the amount of deposited material per pulse is the same in both cases with same parameters other than f. The shape of RHEED oscillations (**Fig. 4.5 d**) is supporting the assumption of complete closure

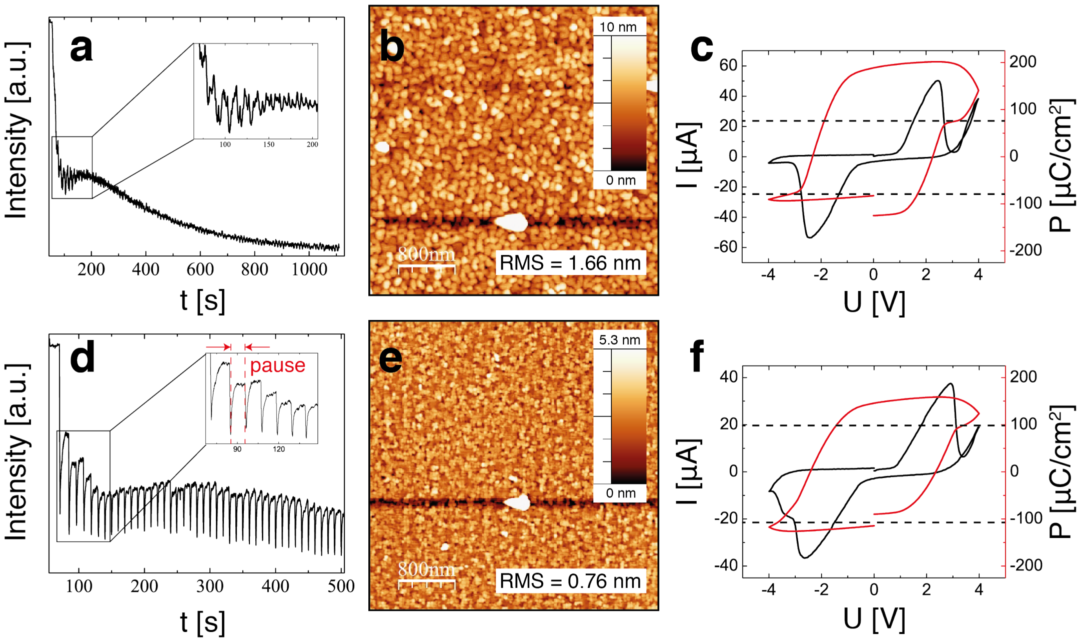

Figure 4.5: Continuous vs. interval deposition. Upper row: Continuos deposition, lower row: Interval deposition. **a** and **d**, Intensity of the specular reflection over time during growth. In the lower case, the inset shows the time interval in which the laser did not shoot. During this period of time, the surface reconstructs, as visible from the intensity recovery. **b** and **e**, AFM pictures of PZT surfaces. The RMS value for the interval-deposited film is less than half of the other one. The step terraces of the underlying STO substrate can be seen as well. **c** and **f**, $I(V)$ (black) and $P(V)$ (red) loops for the differently grown PZT films. The dashed lines represent the values for the polarization after substracting the contribution from the leakage current.

of one monolayer after each burst. The fact that the intensity always climbs up to a similar value as before, is a good indication of a fully reconstructed surface [128].

In addition to the possibility of film thickness control even for relatively thick PZT, an increase of surface quality (**Fig. 4.5 e**) and ferroelectric polarization behavior was achieved by interval deposition. In order to measure ferroelectric hysteresis loops of the samples, cobalt top electrodes of about 40 nm thickness were deposited *via* magnetron sputtering and patterned by a wet-etching process to achieve capacitor top-electrodes of 1600 μm^2 area. In **Fig. 4.5 c** and **f**, the measured room temperature $P(V)$-loops (red) are presented for both discussed cases. In either case, the polarization values are in the region of 100 $\mu C/cm^2$. Besides asymmetric leakage that lead to the non-matching $P(V)$-loops and an overall widening, no significant asymmetry in the coercive fields of about 2.5 V can be observed. This is a good indication that in neither case the interfaces accumulate charge carriers (i.e. due to oxygen vacancies), which would lead to an offset/imprint in the $P(V)$ loops [135]. Although for ultrathin films in the tunneling regime it is expected to obtain a certain asymmetry due to the large interaction of the asymmetric barriers [136], for thicker films the interface contributions should be less pronounced and thus the coercive field values be symmetric.

Ultrathin films of PZT in the range of $2-4$ nm thickness show a very good sur-

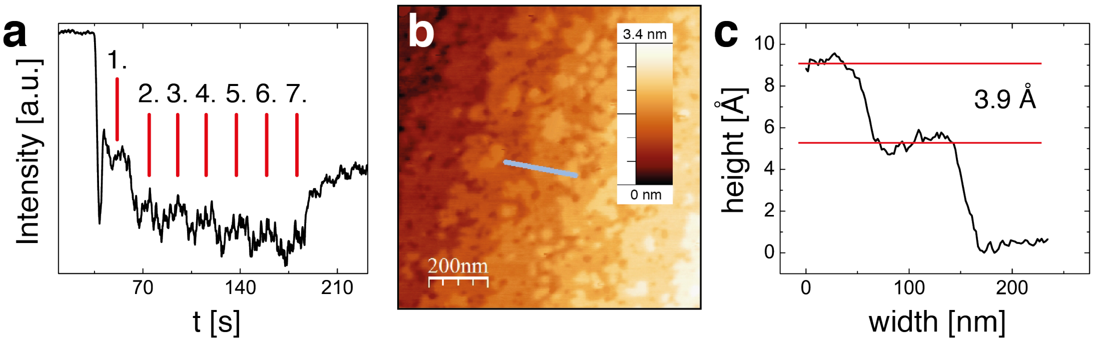

Figure 4.6: Growth of a PZT tunnel barrier. **a**, Specular reflection intensity oscillations during the growth of a PZT film of 7 unit cell thickness. The single oscillations are marked by red bars. **b**, AFM image of the PZT surface morphology. **c**, Profile of the grey line in **b** with emphasize on the step height of around 3.9 Å.

face morphology with continuos growth. Because specular reflection RHEED intensity oscillations are a very reliable indicator to control the thickness in this regime, continuos deposition was used. A summarizing data sheet of the structural and morphology properties is shown in **Fig. 4.6**. The specular reflection intensity oscillations (**Fig. 4.6 a**) are, compared to those for LSMO (**Fig. 4.3 b**) rather noisy. This is a result of the two times higher oxygen pressure inside the chamber, which widens, weakens and diffuses the electron beam of the RHEED system. The surface morphology shows strong signs of layer-by-layer growth and resembles the step heights of 3.9 Å of the underlying STO substrate. This assures not only a homogeneous thickness of the film, but also a single termination. The not perfectly closed last layer of the film is most probably due to the fact that the deposition was not stopped exactly at the maximum of the RHEED specular reflection intensity.

4.3.2 Lead titanate

Lead titanate was only optimized for ultrathin film growth. Morphology and crystalline structure resemble the expected values for epitaxial growth on STO. Epitaxial 2D growth was obtained, which enabled RHEED oscillation counting and thus thickness control during PLD (**Fig. 4.7 a**).

The surface morphology of PTO is very smooth and clearly shows layer-by-layer growth characteristics, visible on the islands of around 4 Å height (**Fig. 4.7 b**). A line profile (**Fig. 4.7 c**) along the grey line inside the AFM picture indicates the reassembly of STO terrace steps, assuring a uniform surface termination. Lead titanate grows epitaxially in respect to LSMO as a bottom electrode, which can be verified by a reciprocal space map around the (103)-reflections of the materials (**Fig. 4.7 d**). In this case, a 15 nm thick PTO film was grown fully strained with a measured c-lattice constant of $c_{PTO} = 4.12$ Å, which is 0.8 % smaller than a recently reported bulk value of $c_{PTOlit} = 4.1526$ Å [137]. Due to the tensile strain given by the larger in-plane lattice parameter of STO, the tetragonality of the measured film is reduced to $c/a_{strained} - 1 = 0.055$, which is 15.4 % less than the bulk tetragonality of $c/a_{bulk} - 1 = 0.065$.

Furthermore, SXRD measurements were performed on a tunnel junction with a PTO-barrier of 8 unit cells (**Fig. 4.7 e**), using 20 keV X-rays at an incidence angle

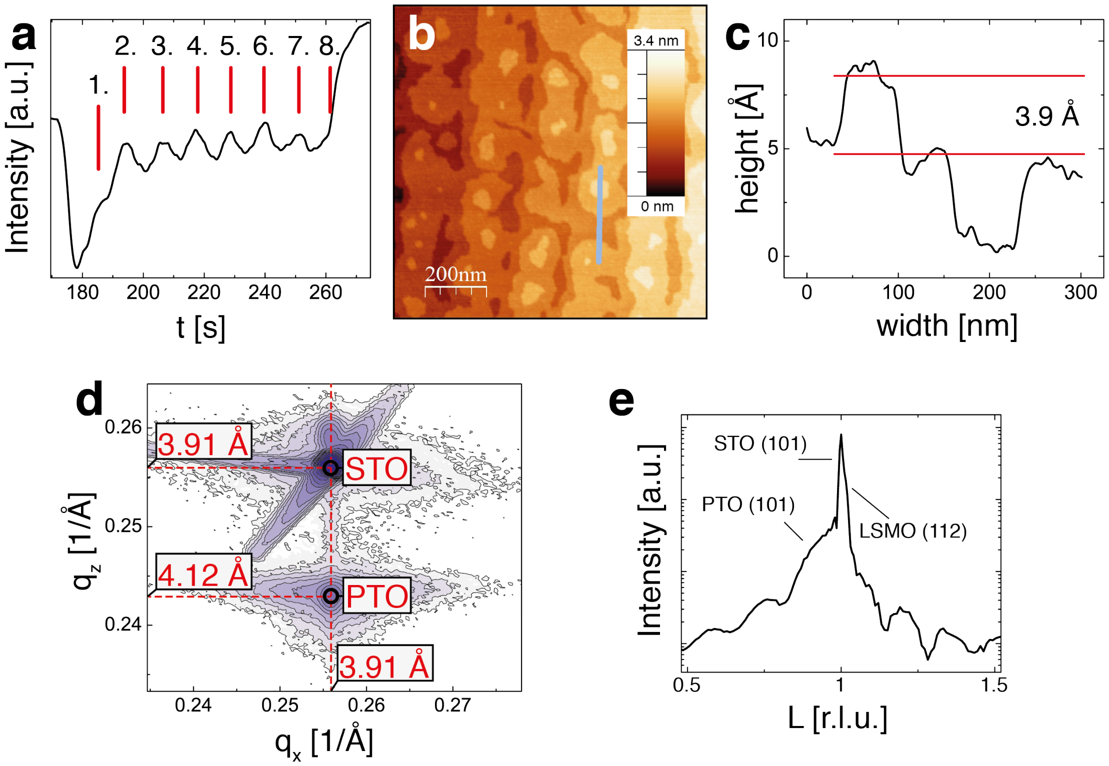

Figure 4.7: PTO ultrathin film structure and morphology. **a**, Thickness control *via* counting of RHEED oscillations during deposition. Red bars indicate the local maxima, representing full closure of one monolayer. **b**, Characteristic signs of layer-by-layer growth, visible on this surface morphology picture taken with AFM. **c**, Height profile taken from the grey line in **b** with indication of the 3.9 Å lattice constant value of STO, showing that the islands and terrace heights are of comparable size. **d**, Reciprocal space map around the (103)-reflections of a 15 nm thick PTO film grown on LSMO/STO. The number values in the map are the lattice constant values for the respective materials in q_x and q_z direction. **e**, SXRD data from (10L) crystal truncation rods for an 8-unit cell thick film. Reflections coming from STO, PTO and LSMO are marked.

of 0.5 ° at the synchrotron beam-line 107 of the Diamond Light Source in UK. Clear Kiessig oscillations prove the good long-range quality of the epitaxial ultrathin PTO layer.

4.3.3 Lead zirconate

The antiferroelectric lead zirconate is used to engineer the termination of the FE/Co interface of multiferroic tunnel junctions as it will be discussed later in this thesis. Therefore one monolayer of PZO was introduced before cobalt deposition on top of the ferroelectric tunnel barriers PTO and PZT.

The RHEED signal in **Fig. 4.8 a** was used to control the growth of PZO that was deposited inside the time window that is marked in the figure by the red area. The intensity notably drops after the first few laser pulses, than recovers and even shoots over the original value, probably because the PZO fills valleys of the not completely

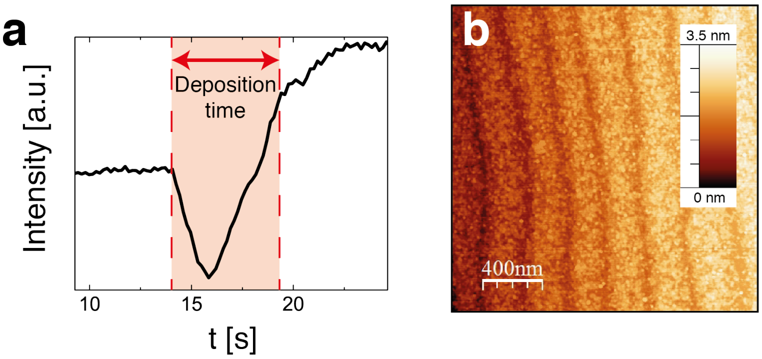

Figure 4.8: PZO terminated layer morphology. **a**, Specular reflection intensity curve of one monolayer PZO. The red shaded area marks the time window during pulsed laser deposition. **b**, Lead zirconate surface on top of PTO.

closed underlying PTO surface. For longer deposition times (not shown), the intensity of RHEED would not change, which is a strong indication for step-flow growth. Accordingly, to obtain exactly one monolayer of PZO, the deposition was ended after the complete recovery of the RHEED intensity signal. However, the rather rough surface, demonstrated on the AFM image in **Fig. 4.8 b** indicates that at least after deposition of the first PZO monolayer, the growth mode tends towards island formation and 3D growth, although the latter would lead to 3D RHEED patterns (square shapes), which have not been observed. These contra indications could mean that the surface morphology significantly roughened during the cool down process, which could not be expected.

In order to show that an ultra thin PTO tunnel barrier with one monolayer of PZO on top is still ferroelectric, this stacking structure was investigated with PFM in dual AC resonance tracking (DART) mode with an applied AC bias of 100 mV (**Fig. 4.9**). As it can be seen on **Fig. 4.9 a** and **b**, both the PFM phase and amplitude of multiple successive loops (phase/amplitude vs. applied DC voltage) show clear signs of ferroelectric switching. The remanence was demonstrated by writing a pattern electrically into the film (**Fig. 4.9 c** and **d**) using applied DC biases of ±3 V. The time between writing the pattern and scanning it was several minutes, indicating good retention of the ultrathin tunnel barrier.

To study the surface quality and stoichiometry in detail, high-angle annular dark field (HAADF) scanning transmission electron microscope (STEM) and energy dispersive x-ray spectroscopic (EDX) experiments were performed on lamellas that were prepared with focused ion beam. The results of an EDX line scan on a PTO/PZO/Co structure are presented in **Fig. 4.10**, together with a HAADF/STEM image that shows the position of the line scan as well (**Fig. 4.10 a**).

The curves in **Fig. 4.10 b, c, e** and **f** give the percentage of respective elements in relation to overall intensity (**Fig. 4.10 d**), following the position along the orange line in **Fig. 4.10 a** from bottom to top. The amount of lead (**Fig. 4.10 b**) compared to the amount of cobalt (**Fig. 4.10 e**) demonstrates that there is a certain overlap of the element specific signals versus the scan position. The spot size of the electron beam, which is in the order of 0.1 nm, should not contribute significantly to this. Cobalt and lead, since they form the interface between the perovskite and pure metal, should

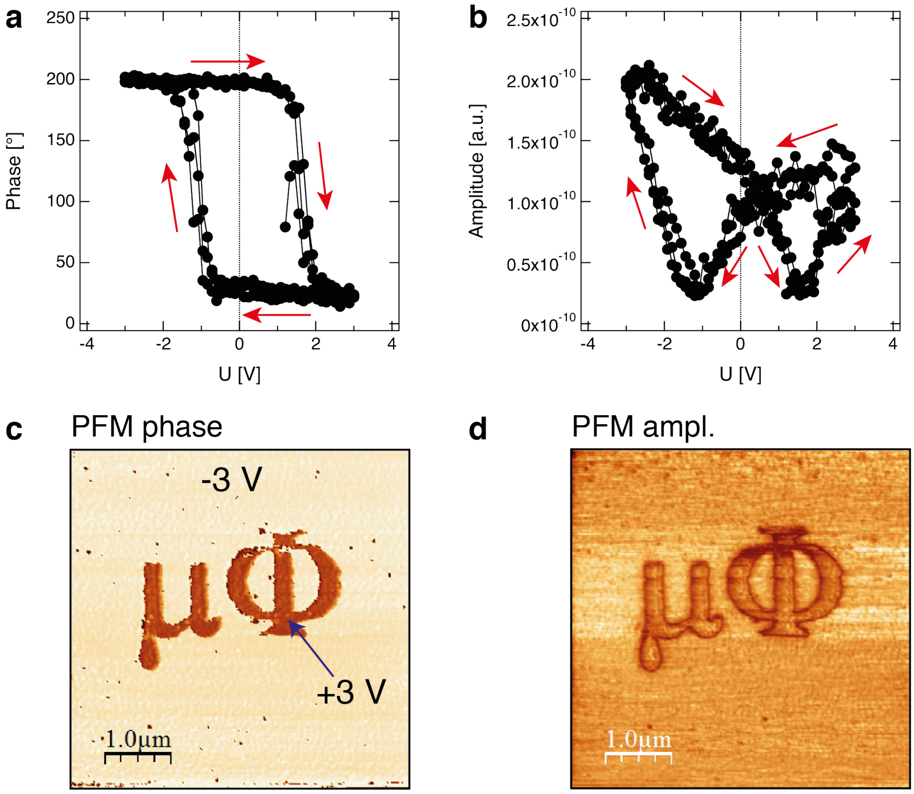

Figure 4.9: DART PFM on a PZO/PTO/LSMO ultrathin (3.2 nm) film. **a**, Multiple loops of the PFM phase versus the applied voltage measurement at fixed tip position. **b**, PFM amplitude from the same measurement as in **a**. **c**, PFM phase signal picture of a structure that was written with the CAFM tip at an applied voltage of ±3 V. **d**, PFM amplitude signal of the same picture as in **b**.

be mutually exclusive at one position. Diffusion processes of Co into the oxide film and vise versa can be ruled out since the metal top electrode was deposited at room temperature, which energetically should not allow inter-layer diffusion. However, the overlap of the cobalt and lead signals happens in a region of approximately 0.8 nm, which is a seizable value. The reason for this relatively large super-imposition of signals could be beam broadening due to crystal defects and the fact that step terraces normal to the picture-plane (direction parallel to the electron beam) lead to overlapping monolayers of material. Both effects would broaden the measured element specific signals especially at the interface and thus lead to less resolution.

With diminishing titanium in the region of the interface, the amount of zirconium notably increases. The zirconium rich area is identified to be 0.7 nm wide (indicated by the red double arrow in **Fig. 4.10 c**) in which the amount of titanium significantly declines. Taking into account that the line profile is the diagonal of a square, the width of zirconium rich material calculates with $w = \frac{0.7\,\mathrm{nm}}{\sqrt{2}}$ to 0.5 nm, emphasized inside the STEM image in **Fig. 4.10 a**. The fact that the relative amount of zirconium does not reach the same value as titanium inside PTO could be the result of the already discussed possible presence of step terraces that lead to an overlap of the signals.

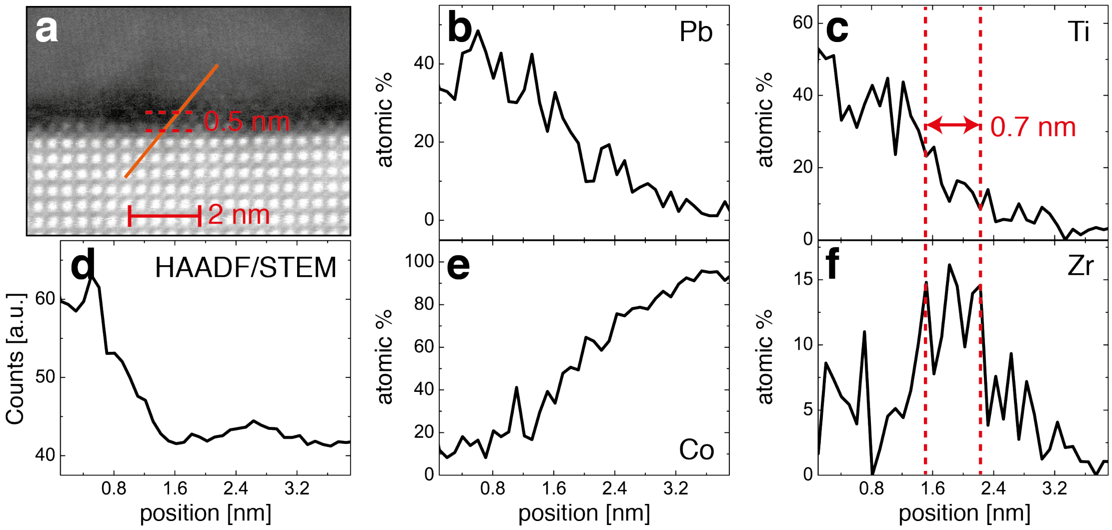

Figure 4.10: EDX investigation at an engineered PTO/PZO/Co interface. a, HAADF/STEM image of the investigated structure. The orange bar is the line, along which the EDX signal was acquired. The Zr-rich area of around 0.5 nm thickness is marked by the two confining dashed red lines. b and e, Relative amount of lead and cobalt along the scan line. c and f, Atomic percent of titanium and zirconium with emphasize of the interface-area, marked by the double arrow. d, HAADF/STEM total counts.

4.4 Crystallinity of the cobalt electrode grown on top of the ferroelectric barrier

In order to model transport [138] and magnetoelectric coupling phenomena inside comparable material systems [139, 140], knowledge of the crystallographic properties at the interfaces becomes important. In bulk, cobalt appears in two crystallographic phases α and β with a phase transition from α to β at 400 C°. α cobalt is stable in the (for metals typical) *hcp* structure, with lattice constants of $a = 2.5$ Å and $c = 4.07$ Å [141]. Above 400 C° however, β cobalt possesses an *fcc* structure with lattice parameter $a = 3.57$ Å [142]. Grown as a thin film on top of the ferroelectric PTO, cobalt forms a face-centered tetragonally distorted structure, which is fully strained in respect to the in-plane lattice parameter of STO [143]. As it is calculated very recently in the work of Borisov [143], adjacent to the interface, cobalt tends to form an inclined tetragonal *hcp* unit cell with $\Theta = 42.8\,°$ for the polar- and $\phi = 46.1\,°$ for the azimuth angle according to the [110] and [100] directions respectively. In this structure, the interface cobalt atoms are nearest neighbors with oxygen atoms of the titanate-terminated PTO (**Fig. 4.11 d**). To further investigate the Co structure experimentally, intensive surface sensitive XRD studies should have been performed that was not done in the framework of this thesis.

However, the color coded high resolution electron microscopy (HREM) image in **Fig. 4.11 a** shows that the investigated cobalt film region is mostly epitaxial. Other regions however left rather the impression of a mild texture. The fast Fourier transform pattern (**Fig. 4.11 c**) obtained from the HREM image in **Fig. 4.11 a**, clearly shows the diffraction spots of cobalt that are tetragonally distorted ($a < b$). A high

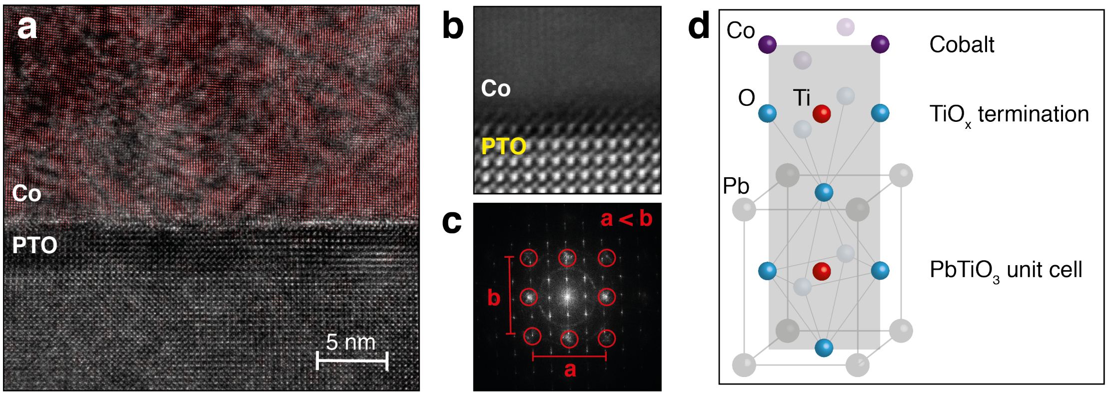

Figure 4.11: Crystallinity of cobalt on PTO. **a**, Color coded HREM image of a PTO/Co heterostructure. **b**, HAADF/STEM image of the same structure as in **a**, but with focus on the interface. **c**, FFT of **a**. The red circles mark the identified cobalt diffraction spots. Inside the image, the bars labeled with a and b demonstrate the tetragonal distortion of Co. **d**, Schematic of the titanate terminated PTO at the cobalt interface as it is proposed by Borisov et al. [143].

magnification HAADF/STEM image in **Fig. 4.11 b** demonstrates the atomically sharp interface between oxide and metal. These qualitative measurements indicate that theory and experiment might be comparable from the structural point of view.

4.5 SQUID measurements on the separated films

In later paragraphs of this thesis, the magnetic properties of tunnel junctions play a very important role, hence the magnetic properties of similar cobalt and LSMO films have been measured *via* a Superconducting Quantum Interference Device (SQUID, performed by G. Apachitei at Warwick University). With this technique, it was possible to acquire the in-plane magnetic coercive fields of the used ferromagnetic thin films separately, by measuring two different samples: The first comprising only a LSMO layer of 32 nm thickness and the second one with Co(40 nm) / PTO(2.46 nm) / LSMO(4 nm) for measuring the stronger influence of the Co electrode. Both samples were not structured and in case of the first one $3 \cdot 5\,\mathrm{mm}^2$ in size, whereas the second sample was $5 \cdot 5\,\mathrm{mm}^2$ large. The magnetic experiments have been conducted at room temperature (300 K) and 5 K, leaning on the used parameters of the following experiments, which were mainly done at the latter temperature.

In **Fig. 4.12 a**, the magnetic hysteresis loops for both samples are plotted for 300 K. Parasitic linear contributions of paramagnetic parts in the system were subtracted, so that the saturation branches of the hysteresis loops are constant. The derivative of the data was simply calculated using the difference quotient.

At this temperature, the coercive fields are with $H_{C,Co} = \pm 4.0\,\mathrm{mT}$ and $H_{C,LSMO} = \pm 0.4\,\mathrm{mT}$ relatively small (**Fig. 4.12** b), which is expected since thermal energy competes with the inner order and therefore reduces the anisotropy of magnetic materials. However, magnetic remanence is visible for both films, which is a proof for ferromagnetism up to 300 K. The saturation magnetic moment is reached for higher applied magnetic fields then the coercive fields of cobalt (with around 50 mT) and LSMO (from

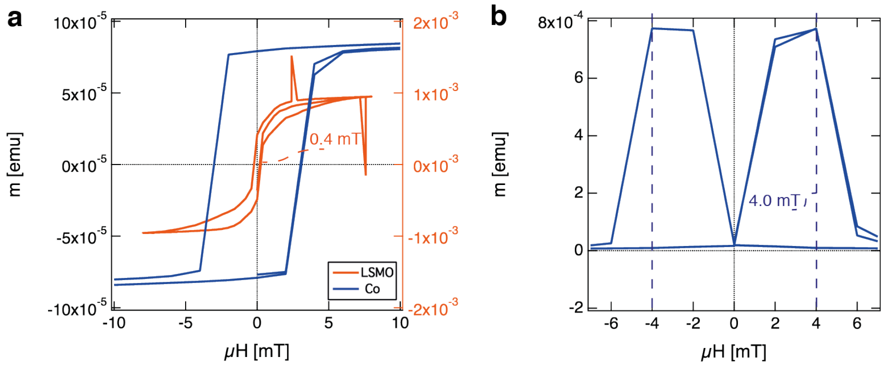

Figure 4.12: SQUID measurements on LSMO and cobalt films at 300 Kelvin. **a**, SQUID signal m [emu] versus applied magnetic field μH [mT] for a Co/PTO/LSMO heterostructure (blue line) and for a 23.4 nm thin LSMO film (orange line). **b**, Emphasis on the coercive field of the Co/PTO/LSMO sample *via* the derivative of the signal dm/dH [emu/mT].

7 mT on). It should be pointed out that the magnetic easy axis of neither of the investigated samples has been experimentally determined. Although measuring in the easy magnetic plane, a difference in coercivity both in LSMO and in Co should be expected as a function of the rotation axis perpendicular to the plane. The LSMO easy axis for instance is strongly dependent on the orientation of the step terraces of the underlying STO substrate. In all experiments, however, magnetic measurements have been carried out with a magnetic field applied in plane and in parallel to a particular edge of the respective sample, which grants reproducibility and comparability with the SQUID and TMR data that are carried out later in this work.

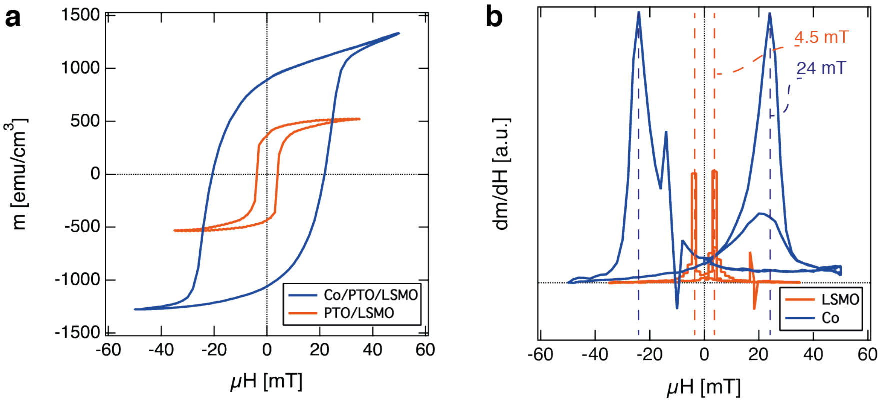

Figure 4.13: SQUID measurements on LSMO and cobalt films at 5 Kelvin. **a**, SQUID signal m [emu] versus applied magnetic field μH [mT] for a Co/PTO/LSMO heterostructure (blue line) and for a 23.4 nm thin LSMO film (orange line). **b**, Comparison of both measurements *via* the derivative of the signal dm/dH [emu/mT]. The coercive fields for both samples are emphasized inside the graph for cobalt (blue) and LSMO (orange) by the dashed, vertical lines.

The situation changes for much lower temperatures (**Fig. 4.13 b**), where the coercive fields become with 24 mT for cobalt and 4.5 mT for LSMO more than 5- respective 10-fold larger and thus very usable for spin filtering junctions, a.k.a. TMR junctions. The big difference in the coercivity should make it easy to select between parallel and antiparallel alignment of the top and bottom electrodes with applied in-plane magnetic fields.

Additionally to the presented results, in-field cooling measurements were carried out to look for exchange bias effects in both samples.[1] The applied magnetic field was therefore set to 800 mT, after which the samples were cooled down to the measuring temperature of 5 K. The graphs for these measurements are not shown here, because they do not differ measurably from the data in **Fig. 4.12** and **4.13**, meaning that no "macroscopic" exchange biasing effects occur in the measured samples and that potential CoO antiferromagnetic top layers do not have any influence on the symmetry of the coercive fields. This detailed question will be discussed in a later chapter, dealing with exchange bias effects that most probably occur at one of the FE/FM interfaces.

The absolute values of the magnetization of the measured films (in saturation and remanence) are not discussed here and show some ambiguity. The calibration of the sample inside the SQUID was not completely successful, which could have had many reasons. The coercive fields were, however, in all cases very reproducible and sensible for further analysis.

4.6 Summary of the chapter

The high quality of the interfaces in tunneling structures was approached by carefully optimizing oxide growth parameters with *in situ* RHEED control of thickness and surface morphology. For the used equipment it was shown that thickness control *via* specular intensity RHEED oscillations is a reliable method for ultrathin film ferroelectrics and the LSMO bottom electrode. Resistivity and structure of LSMO were measured, which agree with literature values and show the expected ferromagnetic phase transition. SQUID measurements reveal non-exchange biased ferromagnetism for the two used electrodes LSMO and cobalt from 5 K to 300 K. HAADF/STEM and EDX investigations confirm the atomic sharpness of the grown interfaces and the possibility to introduce only one monolayer of PZO at the FE/Co interface. AFM and XRD experiments approve the high morphological and structural macroscopic quality of all samples. It was pointed out that poorly treated STO substrates (mixed termination), even when buffered by a relatively thick LSMO bottom electrode, lead to fissured ultra thin ferroelectric films, which were not appropriate to be used as a tunnel barrier. In order to grow thick PZT films in a controlled way with comparable surface morphology to the tunnel barriers, an interval-deposition growth method was applied. It was shown that this method produced comparable ferroelectric properties for PZT films of about 50 nm thickness that were grown with a continuos deposition method. The cobalt top electrode shows mainly signs of epitaxial growth in respect to the underlying ferroelectric, especially at the interface. This is important for comparison with theoretical models that rely on interface-termination and crystal arrangement.

---

[1] This will become crucial for supporting arguments in later presented results.

5

Tunneling in multiferroic junctions

The topic of the following main chapter comprises the evaluation and discussion of electron tunneling transport measurements on multiferroic junctions. In particular, resistive switching effects will be discussed that depend on the polarization direction of the confined ferroelectric tunnel barrier (TER), the spin polarization dynamics of the tunneling electrons (TMR), or a mixture of both, which enables the electric control of the electron spin polarization. In order to confirm the electric transport mechanism to be direct tunneling, temperature dependent measurements were performed.

To switch between two digital resistance states R_{ON} and R_{OFF}, electric pulses of up to $\pm 7\,\mathrm{V}$ were applied to the junctions with pulse widths of up to $0.5\,\mathrm{ms}$. Repetitive measurements of the resistances at low voltage (usually in the range of $200\,\mathrm{mV}$) after switching between the TER states were always performed in order to confirm the reproducibility.

The transmission coefficient of tunneling electrons is proportional to the conductance $G = \frac{1}{R}$ and mainly depends on the thickness of the barrier, the barrier potential height, the magnetic moments of the electrodes and the potential energy of the electrons, *viz.* the applied voltage. The potential shape and height of the barrier is given by the work functions at the interfaces of the junction, which are in the presented cases cobalt/FE interfaces at the top of the tunnel barrier and FE/LSMO interfaces at the bottom. The interface work functions, or potentials Φ_i are, in case of half metallic electrodes, also dependent on the spin of the tunneling electrons in respect to the majority and minority DOS of the metals, which is the TMR effect (see chapter **2.3.1** on page 8). Since direct tunneling is most dominantly dependent on the barrier thickness, only the vicinity of the interfaces plays a role for the conductance of the electrons, which can possess totally different properties than bulk materials.

To study the importance of these above mentioned interface effects for tunnel structures experimentally, four different samples have been realized with different ferroelectric barrier and electrode compositions. Firstly, the TER, TMR and temperature dependent conduction behavior of a PZT tunnel structure will be presented. The further discussion will include junctions, where PZT was replaced by pure PTO and a stacked structure of one monolayer PZO on top of PTO. The importance of the cobalt - FE interface will be discussed based on the results and further supported by magnetic measurements of a Cu/PZT/LSMO junction.

5.1 Temperature dependence of the tunnel resistance

As demonstrated in chapter **4.2**, the electric transport properties of LSMO follow metallic behavior in the range of 5 to about 300 K. The sheet resistance of the bottom electrode (in the oder of several tens of Ohms), compared to that of a tunnel junction can be neglected, since the overall resistance of the measured junctions at low temperature is in the order of several hundreds of kΩ. The resistance behavior over temperature should therefore be mainly dominated by the conduction through the ultrathin insulating tunnel barrier. An exemplary tunnel junction containing Co/PZT/LSMO with a barrier thickness of 4.1 nm was measured inside a Quantum Design physical property measurement system (PPMS) by contacting it with a platinum wire.

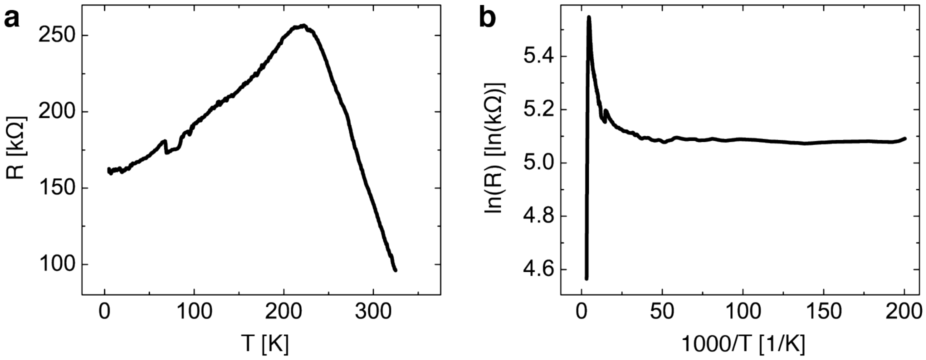

Figure 5.1: Temperature dependence of the tunnel resistance for a Co/PZT/LSMO junction. **a**, Resistance versus temperature over a broad temperature range of about 350 K. **b**, Arrhenius plot of the resistance versus inverse temperature to demonstrate that the slope at low temperature is almost equal to zero. The extrapolated resistance value at 0 K is 161 kΩ.

In **Fig. 5.1 a**, the resistance evolution for decreasing temperature between 325 and 5 K is presented. In the R versus T plot, a resistance increase of more than 150 % can clearly be seen during the cool-down from room temperature to about 220 K. Down to 5 K, the resistance declines to 161 kΩ, but never reaches lower values than at room temperature again. The Arrhenius plot (**Fig. 5.1 b**) does not reveal thermal activated processes in the low temperature region (below 20 K).

However, by plotting the conductance ($G = \frac{1}{R}$) versus temperature, three conduction mechanism regimes can be identified that are emphasized by the colored regions (**Fig. 5.2**).

Those three regions are divided into: Region **I** (yellow area), for temperatures below 20 K, region **II** (light green area) for temperatures between 20 K and 240 K, and region **III** (grey area) for temperatures above 240 K. In region **III**, a thermally activated mechanism plays a major role for the conductance.

The GM model (see chapter **2.3.1** on page 8) was used in the present case as a fitting function (equation 2.4) for the data in region **III**. The resulting fit (green line in **Fig. 5.2**) with the parameters $d = 4.1\,\text{nm}$, $G_{DT} = 3 \cdot 10^{-6}\,1/\Omega$, $N = 7$ and $\alpha = 0.207\,\text{Å}$ represents the data with good agreement. The number of localized states suggests that the conduction model could also be given by directed inelastic hopping

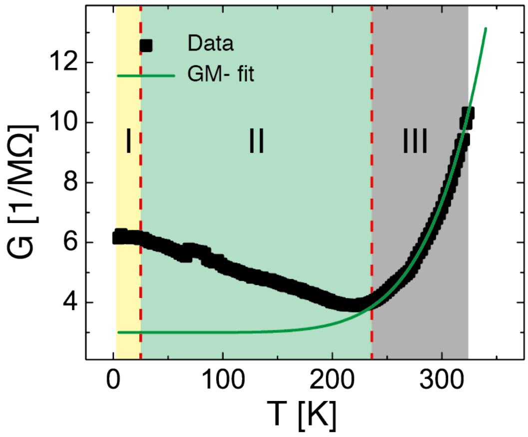

Figure 5.2: Temperature regions of different tunnel conduction mechanisms in a Co/PZT/LSMO junction. Conductance versus temperature plot including the measured data (black symbols) and the fitting based on the GM model (green line). Three regions were identified based on the slope of the data curve that are emphasized by the colored areas.

of electrons [144], which can be true for high order channels of $N > 2$. However, a change of N by only 1 leads to a big variation of the fitting curve, making it impossible to compensate with the other parameters in reasonable ranges. This suggests that the found fitting parameter $N = 7$ is a representative number of localized states inside the tunnel junction.

Given the fact that the thickness of PZT contains around 10 unit cells of the ferroelectric, the localized states might be explainable by the number of Ti atoms (excluding the ones at the interfaces) in the center of tetragonal unit cells in PZT, which could provide electronic states for the tunneling electrons. A comparison with a recently reported result, where the number of localized states was found to be $N = 4$ [73] for a $12\,u.c.$ thick BTO barrier is difficult due to the fact that in this case the resistance consistently increased with declining temperature over the complete temperature range of 50 to 300 K. The measured Co/PZT/LSMO tunnel junction though possesses a transition between the two regions **III** and **II**, which is similar to a metal-insulator transition. Another group who obtained comparable behavior on a LSMO/BTO/LSMO tunnel junction [145] explained this phenomenon by a mix of the already explained inelastic tunneling through localized states in the barrier and the metallization of LCMO underneath the ferroelectric, which increases the effective tunnel barrier thickness. Although LSMO alone does not possess such a phase transition at any point inside the temperature region of interest, interface mediated phase transitions of the bottom LSMO film can not be ruled out. Reported studies on spin valve LSMO/STO/LSMO [98, 146], Co/STO/LSMO [147] and (CFO/FE)/STO/LSMO [148] tunnel junctions show maxima of the junction resistance below room temperature as well. The transition into decreasing resistance with decreasing temperature has been explained by a reduction of the interface order inside the LSMO. This leads to the conclusion that in the temperature region above 20 K, competing transport phenomena play a role that can not be separated just based on the present measurements.

However, the fact that the resistance is almost constant at temperatures below 20 K (region I) suggests that only temperature independent direct tunneling conductance is measured. For this reason, the following measurements were conducted well below 20 K, which should lead to the quantum mechanical direct tunnel resistance that can be well described with the Brinkman model.

5.2 Tunnel electro- and magnetoresistance of a Co/PZT/LSMO tunnel junction

In this section, tunnel junctions with a PZT tunnel barrier of 3.2 nm thickness and electrode surface area of 1600μm^2 will be discussed. Results that show TER and TMR, measured inside the cryoprobing station (see chapter **3.4.1** on page 28), will be presented. Based on the assumption that direct tunneling is the dominating transport mechanism as it is discussed in chapter **5.1**, fits with the Brinkman model were performed in order to obtain several important electrical parameters of the tunnel junction. Based on these parameters, the origin of the TER will be discussed comprising the possibility of an effective tunnel barrier thickness variation that is supported by *ab initio* calculations of theoretical groups on very similar devices. The TMR effects were illustrated by plotting the total junction resistance versus the applied magnetic field, which includes both the resistance of the background and the magnetic switching effect. This way of presenting the data was chosen to be able to easily compare the effects of TER on TMR on the junction resistance.

5.2.1 Electric switching of the tunnel resistance

At 5 K, the junction was switched into the high resistance state (R_{OFF}) with applied voltage pulses of +2 V and into the low resistance state (R_{ON}) with −1.5 V, meaning that the ferroelectric polarization for the R_{ON} and R_{OFF} states were pointing towards the cobalt (P_{up}) or away from the cobalt electrode (P_{down}), respectively. In both cases, a pulse width of $\Delta t = 500\,\mu$s was sufficient to switch into the corresponding fully saturated resistance states. The reason for applying pulse amplitudes with a difference of 0.5 V was not motivated by anything else than trying to find the minimum bias that would lead to the same resistance states. Switching the ferroelectric polarization many times can cause fatigue [149, 150, 151] for bulk ferroelectrics but must also be considered for ultra-thin films. However, using switching pulses with amplitudes just above the ferroelectric coercive field can produce robust tunnel junctions that are switchable up to $4 \cdot 10^6$ times [27]. The asymmetry of the coercive field most probably originates from the built-in electric field that can lead to a strong ferroelectric imprint [136] that explains the difference of the pulse amplitudes in order to switch between the two resistance states.

After each pulse, the IV-characteristics were measured (**Fig. 5.3 a**). A range of ±200 mV was chosen for two reasons: On the one hand, applying voltages significantly less than the coercive field of the ferroelectric will not change the polarization state and thus the resistance. On the other hand it is important to stay inside the direct tunneling regime and therefore the applied bias must not exceed the potential barrier height at the interfaces. These are 0.6 eV in the case of PZT/LSMO [152] and well above 0.2 eV in case of Co/PZT, as the Brinkman fitting parameters in this thesis and values for the (in terms of carrier density) comparable Pt/PZT interface [153] suggest. Measured at 100 mV, the resistances of the measured junction are 2.2 kΩ and 9.1 kΩ for the R_{ON} and R_{OFF} states respectively. The resulting TER value of $\frac{R_{OFF}}{R_{ON}} \approx 4.1$ is seizable, but compared to literature values rather small [17]. A thickness dependence, which plays a crucial role in the magnitude of the TER [65], is not investigated in the framework of this thesis, but it is expected that an increase of tunnel barrier thickness leads to an increase of the TER. Additionally, it cannot be ruled out that pinholes or defects in the tunnel barrier itself contribute to parasitic current leads, which would decrease the resistance value for the R_{OFF}-state and thus decrease also the overall magnitude of the TER.

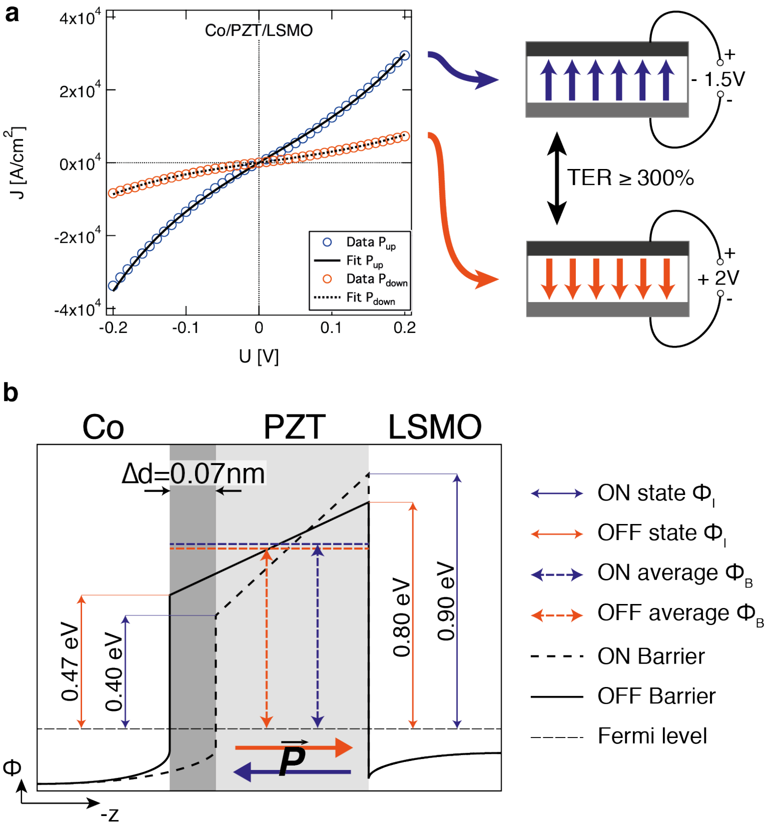

Figure 5.3: Tunnel electro resistance of PZT at 5 K. a, Current vs. applied bias U in the range of ±200 mV. The data points (cubes) are the measured data points for the ON (blue, after a −1.5 V pulse) and OFF (red, after a +2 V pulse) states, respectively. Black lines represent fitting curves with the Brinkman model. **b**, Band diagram based on parameters from Brinkman fitting. The different shaded areas indentify the respective material, whereas the dark grey area is the thickness difference of the ferroelectric barrier that results upon polarization reversal.

The data were fitted using the Brinkman model (**Fig. 5.3 a**, lines) and taking into account all fitting parameters within reasonable boundary conditions of 3 nm $< d <$ 5 nm for the tunnel barrier thickness, 0.1 m$_e$ $< m_{eff} <$ 5 m$_e$ for the effective electron mass and 0.1 eV $< \Phi_{i1,i2} <$ 5 eV for the barrier heights at the interfaces for Co/PZT ($i1$) and PZT/LSMO ($i2$), respectively. Although being performed as a 2-point measurement, IV sweeps on isolated LSMO of the same thickness grown on STO and contacted in the same way with a tungsten probe show an absolutely linear behavior with resistance values of two orders of magnitude less. The contribution of contact and LSMO sheet resistances should therefore play a less dominant role and would otherwise only lead to a systematic and symmetric error. The resulting parameters (two upper lines in **Table 5.1** on page 71) are graphically visualized on a band-diagram in **Fig. 5.3 b**.

Obviously, the thickness for both polarization values differs by $\Delta d = 0.7\,\text{Å}$, which is only 1.6 % of the overall tunnel barrier thickness (sketched by the dark grey area in the schematic). However, although the average potential barrier height for the polarization down (towards the LSMO electrode) state is actually less than in the opposite case, the resistance of the first is much higher. For this reason, the influence of an effective thickness variation must be stronger than that of the average potential barrier height, resulting in an inverse TER. The shapes of the triangular potential barriers in terms of the values Φ_{i1} and Φ_{i2} for the Co/PZT and PZT/LSMO interfaces, respectively, reflect the direction of ferroelectric polarization.

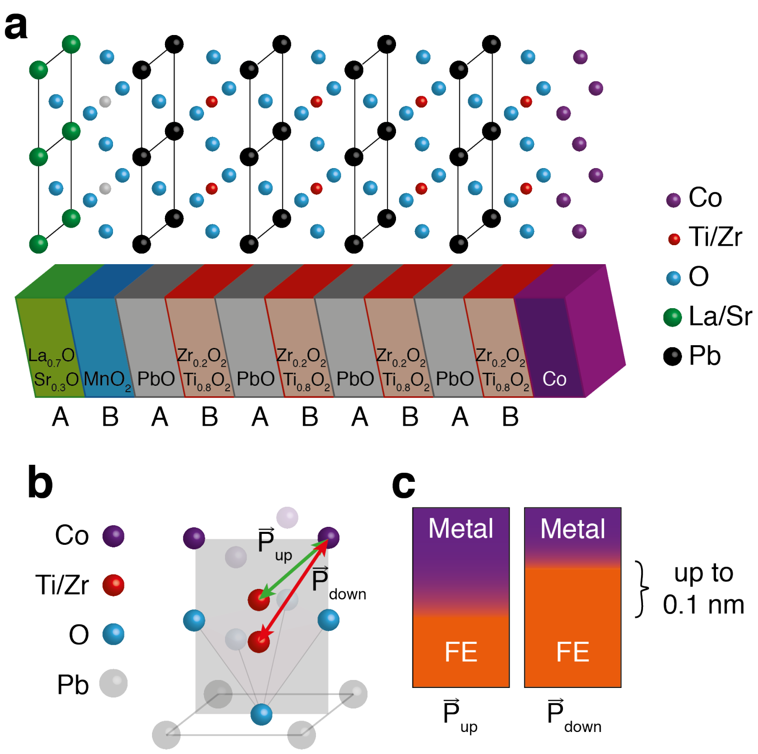

Figure 5.4: Schematics of Co/PZT/LSMO interface terminations. This figure emphasises the termination at the interfaces that are given for the Co/PZT/LSMO tunnel structure. **a**, Stacking of the perovskite structure for the ultra thin film with ABAB... stacking sequence. **b**, Atomic configuration at the interface. The green and red arrows are the distances of titanium to the next cobalt atom for polarization down and up, respectively. **c**, Illustration of the effective interface, consisting of metal and ferroelectric, based upon the ferroelectric polarization.

For the discussion of this result one of the earliest publications on ferroelectric tunnel junctions by Kohlstedt et al. [12] will be consulted. Mainly three possible reasons for TER effects in FTJs were theoretically analyzed in this work. First, it is important to recall that all of the given explanations need a source of asymmetry along the tunnel current axis, which would result in a change in resistance upon either changing the ferroelectric polarization of the tunnel barrier, or flipping the tunnel junction by 180° with respect to the positive and negative poles of the voltage source. This can be easily seen on the following approximation of the current density after Brinkman (see equation 3.4 on page 32) [72]:

$$J(V) = C_1 V + C_2 V^2 + C_3 V^3 \tag{5.1}$$

The only coefficient in eq. 5.1 that has an asymmetric influence is C_2, which is proportional to the difference $\Delta\Phi$ of the potential barriers Φ_{i1} and Φ_{i2}.

As described in chapter 2.3.2.1, one of the proposed reasons for TER could stem from the depolarization field, which is asymmetric upon ferroelectric polarization reversal of the barrier due to different screening lengths of the confining metal electrodes. The structural "microscopic interface effect", which was discussed by Kohlstedt on PTO in tunnel junction capacitor geometry, is explained with the "displacements of Ti^{4+} ions" that "modify the microscopic structure of an interfacial region" and thus also change the barrier heights $\Phi_{i1,i2}$ at the interfaces. This explanation might be crucial as a starting point to understand the reason for the variation of the effective tunnel barrier thickness and the resulting opposite sign of the expected TER.

A closer look at the two given interfaces of the tunnel junction reveals that an asymmetry is created by different terminations of the ferroelectric PZT towards its confining electrodes. The grown heterostructure, where the TiO_2-terminated substrate (B-site termination) dictates the subsequent stacking sequence (AB-AB-...) of the perovskites, exhibits A-site terminated PZT at the LSMO interface. At the cobalt interface, however, PZT is B-site terminated as it is sketched in **Fig. 5.4 a**, which is due to the strong chemical stability of the TiO_2 surface [154].

Following this logic, a major contribution to the TER must be expected to stem from the Co/PZT interface, because the ferroelectrically switchable displacement of the titanium atom inside the tetragonal unit cell should play a stronger role in the direct proximity to the cobalt top electrode than at the PZT/LSMO interface. The continuity of the perovskite structure at the PZT/LSMO boundary can be assumed to result in less variation of the electronic properties at this interface upon polarization reversal, because the oxidation state of titanium is not supposed to change dramatically. Of course, a slight modification in the DOS of LSMO at the PZT interface resulting from polarization switching can not be ruled out, but it must be comparably less dominant, because the distance of titanium to the next manganese atom is roughly one unit cell, which is twice as much as the Ti-Co distance.

The displacement of titanium in PZT at the cobalt interface can reach up to 1 Å upon polarization switching [143], which leads to a variation of its bonding character with its nearest cobalt neighbor. This means that the last conducting region for the electrons to pass before tunneling can be shifted upon ferroelectric polarization reversal. It would be too speculative to state that titanium at the FE interface can be a controllable conductive layer, which can be switched on and off by polarization reversal, although it has been already shown by *ab initio* DFT calculations that the surface of B-site terminated PTO and BTO ferroelectrics behaves metallic at low temperatures [139]. However, the tunnel resistance is mainly given by the DOS at the interfaces that strongly varies in the Co/PZT region, which can be translated into a shift of the effective interface in z-direction upon polarization reversal (**Fig. 5.4 c**) and would thus lead to an effective change in tunnel barrier thickness.

This termination induced asymmetry was in fact the reason for the observation of TER in an independently conducted theoretical study. *Ab initio* calculations of a Co/PZT/Co material system reveal that a different termination of opposite Co/PZT/Co interfaces alone would lead to a seizable TER [138]. Importantly to note at this point is that the sign of the TER is precisely the same as in the experiments. The model assumes, like in the real case of the junction, A-site (PbO) terminated PZT at one and B-site ($(\mathrm{Ti/Zr})\,\mathrm{O}_2$) terminated PZT at the other interface. The B-site terminated interface (sketched in **Fig. 5.4 b**) comprises titanium atoms close to cobalt, which must be oxygen reduced, because the interface cobalt forms a CoO_X layer and thus shares the interfacial oxygen atoms with the titanium. This unambiguously changes the electric and magnetic properties of titanium and cobalt and thus has an impact on the DOS at this interface [155], leading to a strong dependence of the resonant tunnel current on the ferroelectric tunnel barrier polarization.

Interestingly, the measured change (**Fig. 5.3 a**) in effective thickness $\Delta d = 0.7\,\text{Å}$ is comparable with the reported displacement of titanium which indeed indicates that the major contribution to the observed TER could be dominated by the effective tunnel barrier thickness variation rather than purely by the asymmetrically screened polarization charges at the interfaces (depolarization-field picture).

Another strong contribution to the TER could be of structural nature. As a result of similar theoretical studies on a Co/PZT/LSMO junction with differently terminated PZT interfaces, the distance between the last cobalt (!) atom and the first manganese atom of LSMO was found to change upon ferroelectric polarization reversal. This effect could be concluded solely from the fact that the bonding nature of cobalt at the PZT interface changes. With values of $\Delta d = 0.6\,\text{Å}$, the calculation is very close to the measured variation of the effective thickness and also here, the sign of TER was the same as in the experiments.

However, since it could be pointed out that titanium inside the first unit cell at the titanate-terminated interface experiences a significant change in its band structure with variation of the ferroelectric polarization, a mixture of both described contributions is possible and would nevertheless mean that the observed effective thickness variation of the ferroelectric tunnel barrier plays a crucial role.[1]

A piezoelectric broadening/strain of the barrier as it is mentioned in one of the early publications on ferroelectric tunnel junctions [10] is unlikely to explain the rather large change in the effective barrier thickness. Since the electric potential inside the ferroelectric is not very asymmetric upon polarization reversal with an expected potential difference of about $\approx 0.1\,\mathrm{V}$ [136] the size effect (see **Fig. 5.5 c**) would be in the order of $0.05\,\text{Å}$. This is more than one order of magnitude smaller than the found effective thickness variations in the measured junctions. The assumption is based on the piezoelectric coefficient of PZT that was measured to be $d_{33} = 45 \pm 5\,\frac{\mathrm{pm}}{\mathrm{V}}$ [47] and on the existence of a built-in electric field, which is caused by the asymmetry of the confining metallic electrodes [136].

---

[1] These conclusions were drawn during the collaboration in form of several discussions with Prof. Mertig and PhD student Vladislav Borisov, who very recently investigated this special problem with *ab initio* calculations.

To demonstrate, which influence a piezo-induced broadening[1] of the tunnel barrier alone would have on the TER, fixed averages of the fitting parameters (see table **5.1**) $m_{eff} = 0.29\,m_e$, $\Phi_{low,i1} = 0.47\,eV$, $\Phi_{low,i2} = 0.8\,eV$, $\Phi_{high,i1} = 0.4\,eV$ and $\Phi_{high,i2} = 0.9\,eV$ (taken from the fits in **Fig. 5.3 a**) were used for both polarization directions with high and low average potential barriers. This separates the different TER contributions from each other. Two sets of IV-curves were plotted in **Fig. 5.5 a** and **b** for the low and high potential barriers, respectively. As a result of the small piezo-induced thickness variation (see **Fig. 5.5 d**) of only 0.05 Å, the resistance change apparently only leads to a relatively small TER of around 2 % in both scenarios.

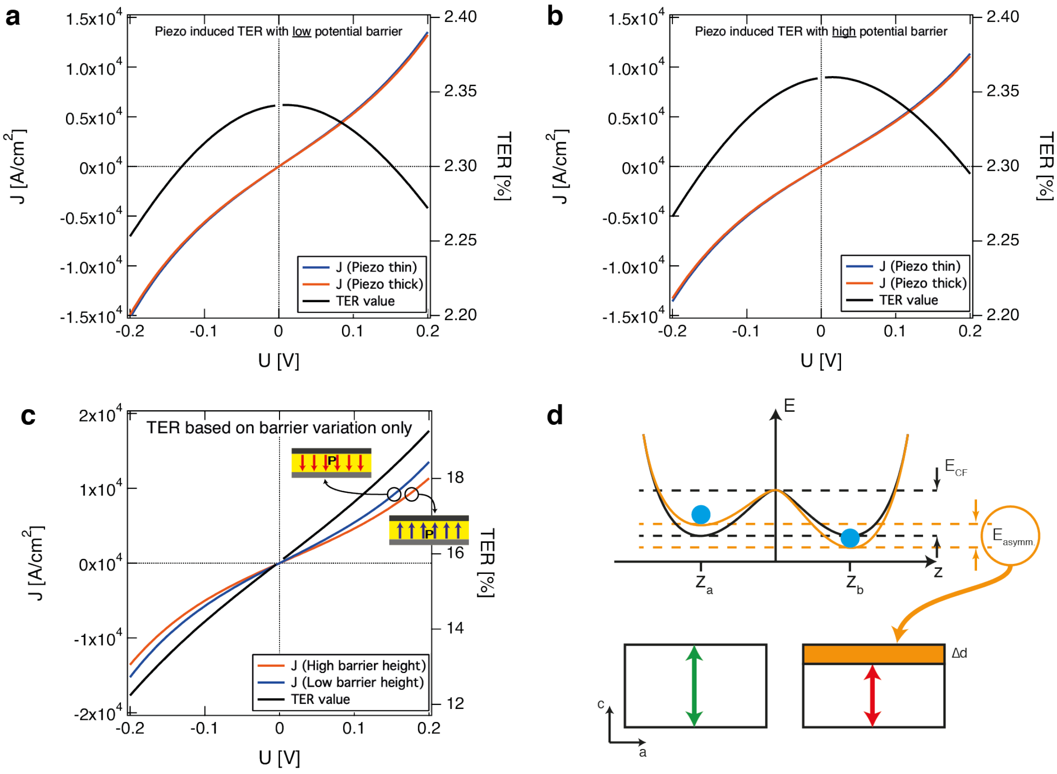

Figure 5.5: Simulation of TER emphasizing separate origins. **a** and **b**, Current density J versus applied voltage U for the two average tunnel barrier heights low and high, respectively. The blue and red lines correspond to the IV simulations for the thin and thick effective potential barrier caused by piezoelectric strain. **c**, Current density J versus applied voltage U with fixed parameters other than the average potential barrier heights in the two opposing ferroelectric polarization directions. The insets emphasize that the polarization direction in the measured case leads to opposite resistance values (red arrows show the OFF state, blue the ON state). **d**, Recalling the schematics from **Fig. 2.1 c**, this sketch should visualize the effect of asymmetry regarding the two opposite FE polarization states on the film thickness due to the inverse piezoelectric effect.

The more interesting case, shown in **Fig. 5.5 c**, is the separation of just the asymmetric screening-induced TER, or in other words the depolarization field induced

---

[1] From now on, "piezo-induced broadening" is reffered to as an electroresistive effect, as it is explained here.

TER, which only takes the average potential barrier height into account. Here, all parameters in the simulation were fixed instead of the work functions at the interfaces, which were taken again from the fits in **Fig. 5.3 a**. It is obvious that the influence of the potential barrier only results in a bigger TER effect of up to 20 %, which interestingly shows an almost linear behavior over the applied measuring bias. The sign of this TER though is opposite from the measured one, emphasized on the schematics of the samples inside **Fig. 5.5 c** by the red and blue arrows, indicating that the resistance in the polarization-down case is the high resistance state (R_{OFF} state) in the measured sample. The size of the isolated resistance ratio is with about 20 % much smaller than that of the measured one with 300 %. The demonstrated, isolated situation would well represent the case which was introduced by Zhuravlev [13].

According to the discussed observations, one can speak about an "inverse TER" that was measured on the Co/PZT/LSMO sample, which might be explainable by an effective thickness variation of the tunnel barrier due to the structural change at the cobalt-PZT interface upon ferroelectric polarization switching. The displaceable titanium ions in the PZT matrix seem to play a key role within the B-site terminated cobalt-FE interface. Apparently, the isolated case of a TER that is purely based on the interfacial barrier heights $\Phi_{i1,i2}$ competes with the presumably found effective thickness induced TER. The latter effect has the much bigger dominance on the resistance change.

The quantitative comparison of experiment and theory are subject of future collaborative projects.

5.2.2 Electric switching of electron spin polarization

In previous work, it was observated that the TMR of a Co/PZT/LSMO junction showed reversible electrical switching of the spin polarization upon polarization reversal [24], which was ascribed to result most probably from the interface of PZT at the cobalt side. This assumption was made based on *ab initio* calculations that showed a change of the induced magnetic momentum of the interfacial titanium upon polarization reversal in the ferroelectrics PTO and BTO [155]. Here the reproducibility and robustness of the effect is shown mostly due to the modification of the experimental conditions including the PLD chamber, targets and substrates.

In **Fig. 5.6**, two TMR loops of the investigated Co/PZT/LSMO junction are shown. Both the red and the blue curves, which represent the measured resistance for the ferroelectric P_{down} and P_{up} states, respectively, show a TMR of about 15 %. Assuming that LSMO acts as a perfect spin filter with at least 95 % spin polarization [41], the reason for the relatively low measured value should therefore originate from the Co/PZT interface. Other reported values of TMR within multiferroic tunnel junctions are for instance: 20 % in Fe/BTO/LSMO structures [156], around 90 % in a Au/$La_{0.1}Bi_{0.9}MnO_3$/LSMO composition [86] and a comparable value of 30 % on a CoO/Co/BFO/LSMO junction [157]. The difference in resistance between the R_{ON} and the R_{OFF} TER states is about a factor of 4, which was subject of the chapter before.

Generally, the sign[1] of TMR can have multiple origins, but is in general not pre-

---

[1] The sign of TMR is defined by the arrangement of the magnetic moments of the electrodes and the corresponding resistance state and is normal for a low resistance state for parallel, and inverse for

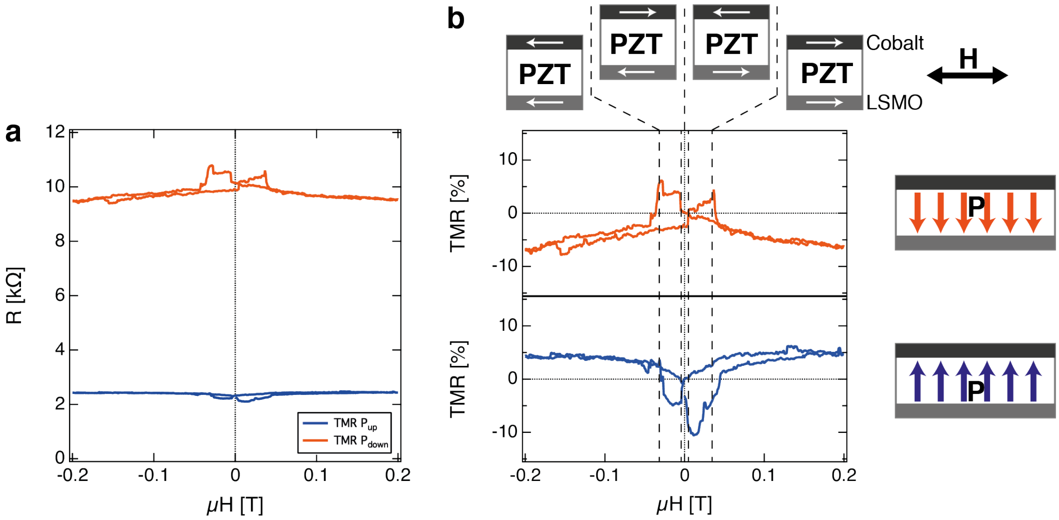

Figure 5.6: Electric switching of electron spin polarization. a, Resistance versus magnetic field, measured at 100 mV applied bias. The red curve represents the resistance of the junction with the ferroelectric polarization pointing towards the LSMO bottom electrode after a positive applied voltage pulse, the blue curve for the opposite polarization direction after a negative applied voltage pulse. **b**, TMR in percent versus magnetic field. The schematics in the figure emphasize the four different regimes of parallel and antiparallel magnetization $\vec{M}$ of the electrodes plus the two ferroelectric polarization directions as it is illustrated *via* the white arrows ($\vec{M}$) and the colored arrows ($\vec{P}$) inside the junction sketches.

dictable with certainty. Studies demonstrate different mechanisms that suggest a dependence of the TMR sign on the applied measuring bias [158] and interface stoichiometry [147, 158, 159, 160, 161]. In the present case, a reversible change of the sign of the TMR is caused by ferroelectric polarization reversal of PZT. The measurement bias was always set to be constant during all measurements. This supports the assumption of a change in the oxidation state of the interfacial titanium, and therefore the DOS at the Co/PZT interface, based on the displacement of titanium in the PZT unit cell at the cobalt interface.

The measurement was performed after cooling down in field (FC := "field cooled"). In this case, the sample was exposed to a magnetic field of $-800\,\mathrm{mT}$, while it was cooled down from room temperature to a measurement temperature of 5 K. The coercive field of LSMO is rather small and can be identified by the uprising of the resistance in the low magnetic-field region. The relatively high coercive field can be ascribed to the cobalt electrode, which should possess a relatively strong crystalline in-plane magnetic anisotropy (see synchrotron measurements in chapter **7** on page 85 and the comparison with SQUID measurements in chapter 5.6.2 on page 72) and has a higher magnetic momentum with $1.6\,\mu_{Co}$ per atom, whereas LSMO possesses a lower total magnetic momentum with $3.7\,\mu_{Mn}$ per unit cell [162, 163] and usually shows relatively weak magnetic anisotropy, which leads to reported coercive fields in the order of 1 mT [164].

The reason for the controllable electron spin flip could not unambiguously shown

---

a high resistance state for parallel magnetic moments of the confining electrodes.

with experiments yet. However, as it is discussed in chapter **5.2.1**, the displacement of titanium at the interface could possibly explain both the inverse TER and the reversible spin-flip with an easy picture. Considering that the above presented reason for the existence of a strong inverse TER is true, the last conduction layer moves into the anticipated antiferromagnetically coupled region of the titanium. As one would expect, the resulting spin flip in such a scenario would occur, when the titanium is in the proximity of the cobalt, which consistently could be shown in the measurements.

5.3 Magnetic and electric properties of a Co/PTO/LSMO tunnel junction

In the following, PZT is replaced by the ferroelectric PTO, which is of the same thickness and possesses comparable ferroelectric polarization properties. Measurements were also conducted with very similar parameters for temperature and measuring biases. The electric (TER) and magnetic (TMR) results are presented and discussed.

5.3.1 Tunnel electro resistance

Removing zirconium from the ferroelectric composition leads to Co/PTO/LSMO tunnel structures based on ultrathin PTO films (see chapter **4.3.2** on page 41). Until now, lead titanate has not been used in capacitor tunnel junction geometries but was reported to possess a "giant" TER of up to 50,000 % according to CAFM measurements [165]. In this work, TER on tunnel junctions of 8 u.c. ≈ 3.3 nm thickness was observed, which has seizable values of around 230 %. CAFM measurements that lead to the dramatically larger TER are not really comparable to the experiments on tunnel junctions in capacitor geometry. Adsorbates at the surface and the electric field geometry at the CAFM tip can lead to very specific results that do not necessarily predict possible TER values coming from material interfaces. It is already known that the barrier height of electrode-PZT interfaces is strongly dependent on the chosen electrode material [166] and thus should have a major impact on the resulting TER.

In **Fig. 5.7 a**, the IV characteristic curves for the two polarization states P_{up} and P_{down} are presented, which were measured at a temperature of 5 K and for a voltage range of ±100 mV. The relatively small bias range was chosen due to the fact that the fitting parameters for the interface-work functions were smaller than 0.2 eV, meaning that a wider range would have caused errors due to the risk of entering the Fowler-Nordheim tunneling regime. The used switching voltages were ±3 V with pulse widths of 0.5 ms. Like in PZT tunnel junctions, positive pulses consistently lead to high resistance states, whereas negative pulses result in low resistant R_{ON} states. However, in the case of PTO, the potential barrier does not have the expected shape (**Fig. 5.7 b**), considering only the polarization charge of the ferroelectric. At the cobalt interface, for example, the potential would have to be larger for the FE polarization pointing towards the LSMO electrode than *vice versa* (recalling Laplace's equation $\Delta\Phi = -\frac{\rho}{\epsilon_0}$), if the screening lengths of the electrodes would not change with the FE polarization. A way of explaining this behavior could be to take into account non-symmetric screening lengths of the metals for both polarization directions. As already addressed before,

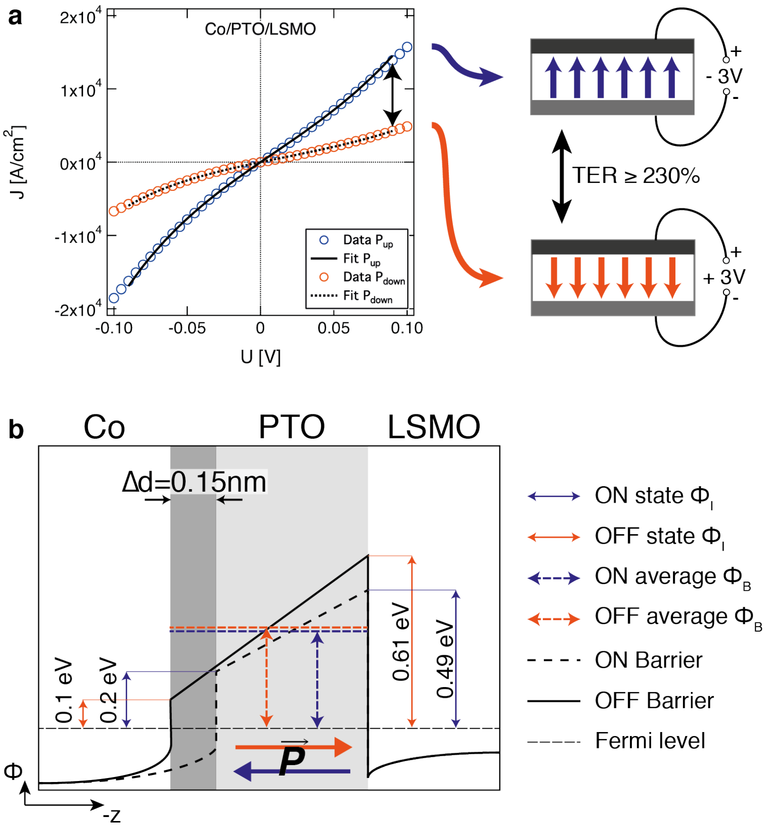

Figure 5.7: Tunnel electro resistance of a PTO tunnel junction at 5 K. a, Current density J vs. applied bias U in the range of $\pm 100\,\mathrm{mV}$. The data points correspond to the two opposite ferroelectric polarization directions ON (blue, after a $+3\,\mathrm{V}$ pulse) and OFF (red, after a $-3\,\mathrm{V}$ pulse) states. The lines represent fitting curves with the Brinkman model. **b**, Band diagram based on parameters from Brinkman fitting. The different shaded areas indentify the respective material, whereas the dark grey area is the thickness difference of the ferroelectric barrier that results upon polarization reversal.

upon switching of the ferroelectric polarization, the effective interface(s) can shift in z-direction together with a change in the DOS.

This change in DOS leads to a variation of the Fermi screening length with $l \propto \left[\sqrt{D\left(E_F\right)}\right]^{-1}$ [167]. Obviously, the depolarization field thus is larger for larger l and smaller DOS, which is given in the case of ferroelectric polarization pointing towards cobalt (recalling $E_z = -\partial\Phi/\partial z$). The screening length in pure cobalt can be as small as 0.56 Å (calculated with a carrier density of $n_{Co} = 5.8 \cdot 10^{22}\mathrm{cm}^{-3}$ [168]). Increasing the screening length by just half a unit cell in terms of changing the DOS along the z-direction by switching the ferroelectric polarization is a gain of more than 100 %. Due to the ultra thin thickness of the barrier, the opposite interface (PTO/LSMO) could be immediately influenced in the same way as **Fig. 5.7 b** suggests. According to this argumentation and based on the fact that the only difference between the two so far analyzed tunnel junctions based on PTO and PZT is the chemical dilution of titanium with zirconium, it seems that the screening lengths of the adjacent electrodes at the interfaces (!) is influenced by the stoichiometry of the used ferroelectrics quite significantly. The TER is, as before in the presented Co/PZT/LSMO tunnel junction, dictated by the effective tunnel barrier thickness variation upon FE polarization reversal.

5.3.2 Temperature dependence of the tunnel electro resistance

To measure the TER of the Co/PTO/LSMO tunnel junction as a function of temperature, it was stabilized inside the cryo probing station for each step, at which one junction was switched back and forth between the ferroelectric P_{up} and P_{down} states electrically. In **Fig. 5.8**, the resulting data points are presented.

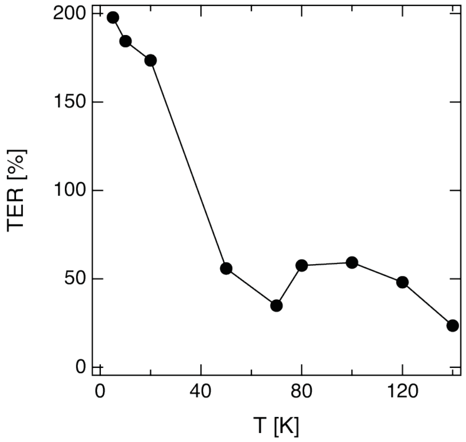

Figure 5.8: Temperature dependence of the TER. $\frac{R_{OFF}}{R_{ON}}$ ratio versus temperature of a measured Co/PTO/LSMO tunnel junction.

It is obvious that between the measured temperatures 20 K and 50 K there is a large decrease of the TER value from around 200 % to less than 50 %. An explanation of this behavior could be a strong correlation of TER and the type of electronic transport that was discussed before in chapter **5.1**, which was also given as an explanation for a similar temperature dependence of a TER based on BTO tunnel junctions [73].

5.3.3 Interface induced exchange bias-like behavior

The TMR in magnetic [97] and multiferroic [86, 157, 169, 170] tunnel junctions is mainly given by the magnetic anisotropy of the confining magnetic layers. In presence of an antiferromagnetic (AMF) layer, the anisotropy can be unidirectional and thus shift magnetic hysteresis loops along the magnetic field axis. This exchange bias [171, 172] is commonly realized by antiferromagnetic layers such as cobalt oxide, which can be achieved by etching of metallic Co after deposition inside an oxygen plasma [157], or by direct cobalt evaporation inside oxygen gas. However, in thick top electrode films, the oxidation of cobalt at the surface should not interfere with the magnetic transport measurements. One reason for this is that only a very thin layer of around 1 nm CoHO on top of cobalt films forms during the first few seconds after being exposed to air at room temperature [173], which is reported to not possess exchange biasing properties [174].

In the following experiments, the gold capped top electrodes possess at least a cobalt film thickness of around 40 nm, assuring that any eventual CoO top layer does not contribute to a possible exchange biased electron tunnel transport.

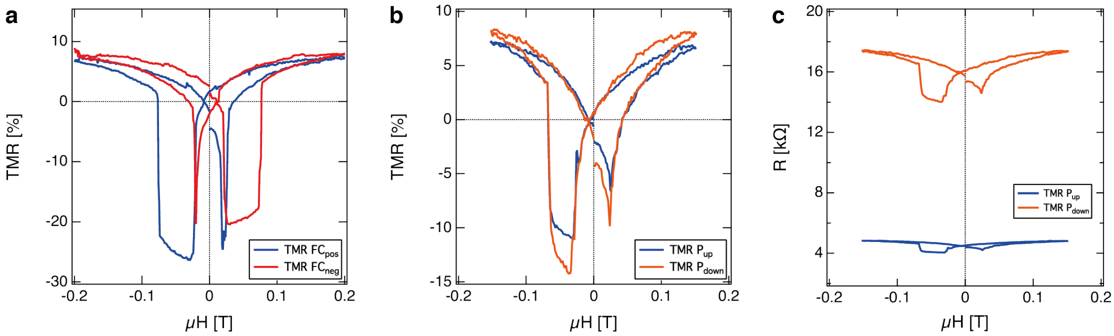

Figure 5.9: Exchange biased TMR of a PTO based MFTJ. a, Two magnetic hysteresis loops, measured after field cooling in two different directions (FC$_{neg}$ and FC$_{pos}$) with applied fields of ±800 mT from 140 K down to 5 K. **b**, TMR loops for another junction of the same sample, showing a small increase of the TMR upon FE switching from the P$_{up}$ (blue) into the P$_{down}$ (orange) state. **c**, Resistance R versus magnetic field μH for the two opposite polarization states, to point out the absolute difference in the junction resistance.

In **Fig. 5.9 a**, two TMR curves of one device are shown. Each curve was measured after cooling down from above 140 K inside an applied magnetic field of +800 mT in the blue case and −800 mT in the red case. Besides the comparable size of the effect in both cases of about 35 %, the shape obviously differs strongly. In both cases, one can observe a clear broadening into the opposite direction to the magnetic field that was applied during FC, which is a strong indicator for a magnetic unidirectional anisotropy due an EB effect [175] (pinning). The strength of the antiferromagnetic pinning in both cases asymmetrically increases the magnetic coercive field of the hard magnetic material by up to 50 mT.

Not so obvious but still observable is also a finite shift along the magnetic axis of the crossing points of both TMR curves, which shows that the magnetic unidirectional anisotropy not only changes the coercive fields, but also influences the hysteretic behavior of the sample. This effect will be quantified and exploited later in this thesis (chapter **5.3.4** on page 65).

In comparison to the discussed PZT case, the ferroelectric polarization direction of the PTO tunnel barrier does not have any influence on the sign of the TMR, although its size increases from 17.9 % to 22.3 % by switching from the P_{up} (R_{ON}) state into the P_{down} (R_{OFF}) state. Although the change of the effect is rather small, the tendency would be opposite to that observed in the PZT case, which means that the TMR and thus the spin filtering for antiparallel magnetized electrodes became more effective in the polarization-down case. However, the asymmetric magnetic anisotropy does not seem to change at all upon reversal of the ferroelectric polarization.

It was only possible to switch the sign of the asymmetric broadening by heating the sample up to a temperature above 140 K. At lower temperatures than that, no sign change of the broadening could be achieved with applied magnetic fields of up to 1 T. In **Fig. 5.10 a**, TMR curves of an investigated device were measured after FC

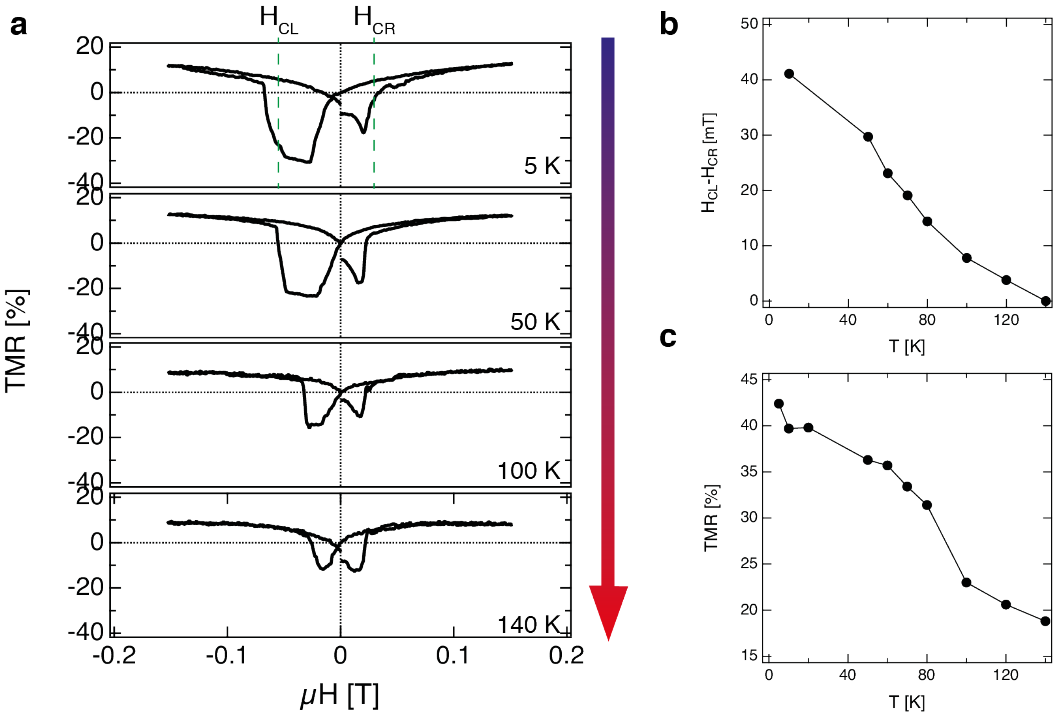

Figure 5.10: Temperature dependence of the antiferromagnetic pinning. a, Magnetic hysteresis curves taken at different, increasing temperatures. **b**, The difference of the strong magnetic coercive fields $\mathrm{H_{CL}} - \mathrm{H_{CR}}$ as a measure of the asymmetry in the TMR loops in **a**. **c**, TMR in % over temperature.

in +800 mT starting at low temperature, which was incrementally increased until the asymmetric broadening vanished.

It thus appears that an antiferromagnetic phase transition can be observed at Néel temperature of around $T_N = 140\,\mathrm{K}$. For a better analysis, the difference of the strong coercive fields on the left (H_{CL}; negative) and right (H_{CR}; positive) side of the TMR curves, $H_{CL} - H_{CR}$ was plotted over the temperature in **Fig. 5.10 b**, which is a measure of the asymmetric broadening. Together with the value of the TMR (**Fig. 5.10 c**), both effects decrease with temperature and eventually reach zero in case of the asymmetric broadening and a two times reduced value for the TMR. Apparently, the spin filtering attributes of the tunnel junction show the anticipated behavior with increasing temperature, which is the reduction of the spin filtering mechanism due to excitation of spin waves with $\propto T^{3/2}$ [94]. However, in conjunction with the fact that it is possible to change the unidirectional anisotropy of the AFM contributor in the system above $T_N \approx 140\,\mathrm{K}$, the vanishing of the asymmetric broadening at a blocking temperature of $T_B \approx 140\,\mathrm{K}$ shows that both the Néel and the blocking temperature are very close and and are much lower than the Néel temperature of CoO, which is in the range of $T_{N,CoO} = 291\,\mathrm{K}$ [176] (bulk) and even tends to further increase for thin films to higher T_N [177, 178] due to the magnetic proximity effect [179]. This could be another indicator for the fact that a potential CoO layer on top of the electrode is very unlikely to be the origin for the observed exchange bias. However, due to the uncertainty regarding the oxidation state of Co at the tunnel barrier interface, a clear conclusion based on the comparison of Néel temperatures is not possible to be drawn, since T_N can strongly depend on the quality of the cobalt oxide layer.

Without the deliberate introduction of an antiferromagnetic layer, it is now possible to exploit the exchange biased TMR in order to achieve robust memory functionality.

5.3.4 Realization of four remanent resistive states

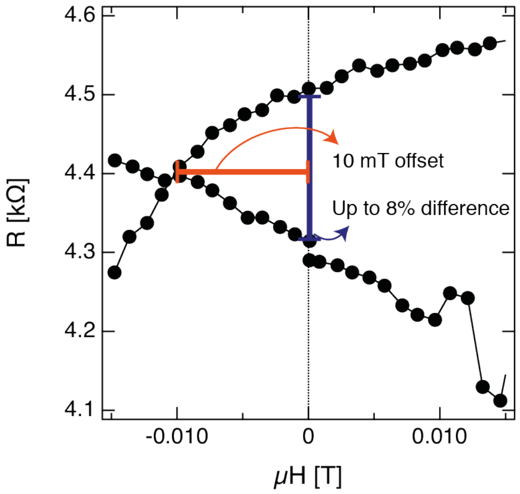

Figure 5.11: Closeup of the exchange biased TMR. Detailed plot of the TMR hysteresis loop around zero magnetic field, measured with an applied bias of 50 mV. The maximal applied field was ±150 mT in order to measure this curve. Red and blue bars indicate the offset and remanence resistance states respectively. The sample was field cooled with a positive applied magnetic field of 800 mT from 140 K down to 5 K.

The observed EB leads to two magnetically addressable remanent resistance states of the investigated junction at zero applied magnetic field. In **Fig. 5.11**, a close up of a TMR loop measured at 5 K, shows the region around zero magnetic field. Here, the applied magnetic field during FC was +800 mT, resulting in an asymmetric broadening and a shift along the magnetic field axis towards negative magnetic fields. The offset of the crossing point is with around 10 mT significant and allows two resistive states in remanence (zero magnetic field) of up to 8 % separation.

Although earlier presented multiferroic tunnel junctions possess in principle up to 8 resistive states [180], the big advantage of exchange biased memory devices is the robustness of the resistive switching, which allows to switch between resistive states with applied magnetic fields of a certain minimum in field strength and read them out in remanence with zero applied magnetic field. In order to switch between two resistance states in the reported non EB multiferroic tunnel junctions, the applied magnetic field needs to be set precisely to the maximum of one of the resistance loops, in order to switch from parallel to antiparallel aligned magnetic moments. Because the coercive fields and therefore the maxima of the TMR loops usually vary from device to device, it is therefore necessary to characterize each junction and apply the corresponding magnetic fields, which is virtually impossible for real device application.

By applying positive and negative magnetic fields of ±150 mT, it is now possible to switch between two magnetic resistance states on top of the already known ferroelectric

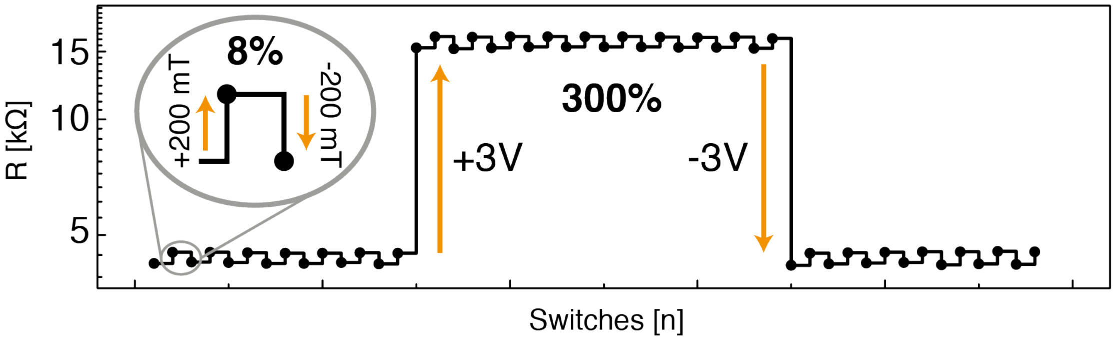

Figure 5.12: Four remanent resistance states at 5 Kelvin. Semi-logarithmic plot of R over number of the switching event. The points are measurements that were taken in remanence (zero applied magnetic field). This visualization should summarize the impact of TMR and TER effects on the resistance of the Co/PTO/LSMO tunnel junction.

resistance states of 300 % difference that are accessible with small voltage pulses. As a result, a ”zig-zag” curve over time was measured after successively applying different magnetic and electric fields to the measured junction and reading the tunnel current with a small applied bias of 50 mV. In summary, the data is shown in **Fig. 5.12**, which demonstrates the combination of the two effects TMR and TER, leading to successively programmed tunnel resistance states.

To visualize the recorded resistance state statistics, the event counts were plotted against the junction resistance in **Fig. 5.13**. In this way, the stability of the measured junction is demonstrated over tens of repetitive switching events. The four resistance logic states are visualized by the color coded numbers inside the inset boxes.

There are no overlaps in the measured resistances after the magnetic and electric switching events, which ensures the reliability of the measurements and allows to discern all defined logic states.

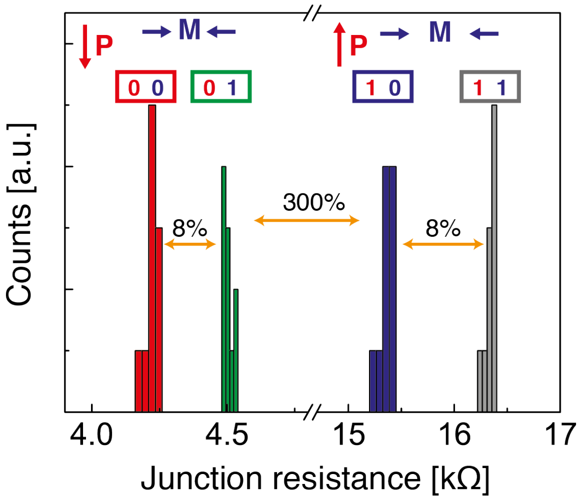

Figure 5.13: Counts of events versus junction resistance. Diagram of the statistics from the successive measurements of the junction resistance in remanence. The insets show the possible four logic states that are magnetically and eletrically accessible, which is visualized by the arrows for magnetization (blue) and ferroelectric polarization (red).

5.4 Enhancement of tunnel electro resistance *via* interface engineering

In this chapter, the electric and magnetic influences on the electron conduction through a PZO-terminated PTO tunnel barrier will be investigated. The introduction of such a PZO layer between PTO and cobalt mimics pure zirconate termination at a ferroelectric interface. This would not be possible by growing just PZO alone, since it is a (bulk) antiferroelectric material and thus not suitable for the direct comparison with tunnel junctions that show TER, based on compositions that comprise ferroelectric properties. And indeed, as it is discussed in the characterization chapter, ultra thin PZO-terminated PTO behaves as a ferroelectric film (see chapter 4.3.3 on page 42).

5.4.1 Influence of ferroelectric-cobalt interface termination on TER

To further increase the amount of zirconium at the ferroelectric-cobalt interface, one monolayer of PZO was introduced between cobalt and PTO as described in chapter **4.3.3** on page 42. The termination of the ferroelectric was hereby changed to a complete ZrO_X monolayer. This engineering induced a dramatic increase of the TER, plus a sign-change regarding the applied voltage pulses to switch between the resistance states compared to the other discussed cases.

In **Fig. 5.14 a**, the corresponding IV characteristics including the Brinkman fits are shown for the tunnel junction with a total tunnel barrier thickness of $\approx 3.2\,\text{nm}$, measured at 5 K. The semilogarithmic plot in **Fig. 5.14 b** demonstrates that the fitting curves represent the data points with good agreement. This way of plotting also has the advantage that the actual TER value can be better visualized. The fitting parameters (**Table 5.1** on page 71) for the IV curves were used to draw the potential lines inside the PZO/PTO barrier (**Fig. 5.14 c**). Noticeable at this point is the big difference in both the thickness for the ON and OFF states (the difference is about 1 Å, whereas the effective barrier thickness in the OFF case is larger) and the very big change of 155 % in the effective electron mass, which was not observed in the other measured heterostructures, yield as fitting parameters of the experimental data with the Brinkman model. The latter is a strong indicator of a change in the conducting mechanism, in this case, the tunneling mechanism. As it is reported in literature, the effective electron mass for tunnel phenomena in junctions based on oxides is usually less than $1\,m_e$, indicating high carrier velocity. In the present case though, a large effective mass of $1.74\,m_e$ was calculated as a Brinkman fitting parameter for the ferroelectric polarization pointing towards the cobalt electrode. This could be a sign for a switch between electron (low effective mass) and hole (high effective mass) conduction, which would be selectable by the ferroelectric polarization direction.

Here, the explanation given for the change of the effective barrier thickness for the above mentioned cases does not fit anymore. The interpretation of the resulting fitting parameters indicates a strong interaction of four phenomena that can have an impact on the TER. The change in effective barrier thickness is still comparable with that of the Co/PZT/LSMO junction, although the sign of polarization, which leads to this thickening, is now reversed. The effective potentials are concurring with the

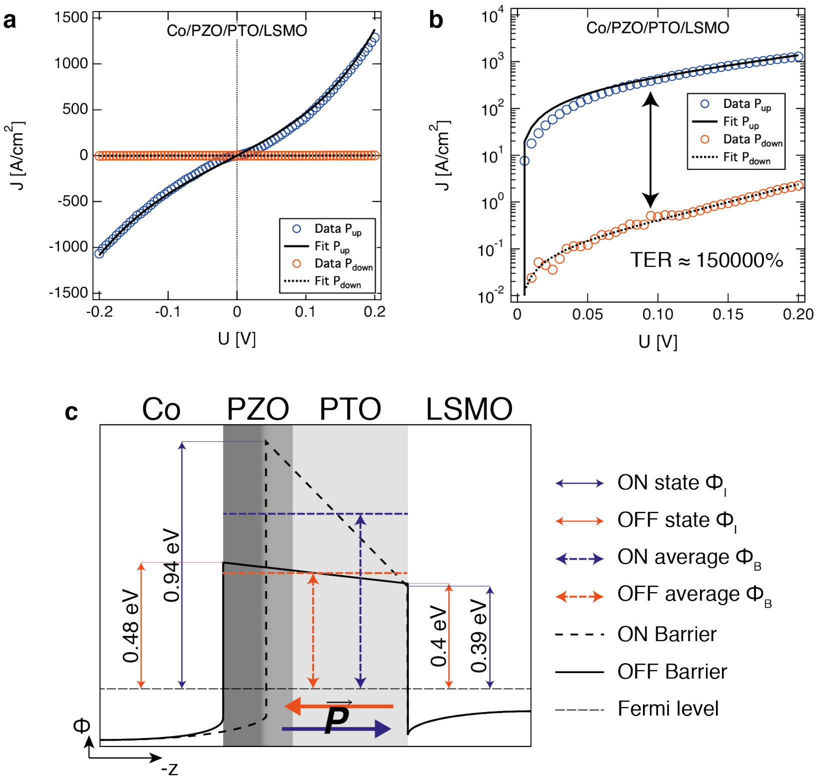

Figure 5.14: Tunnel electro resistance of PZO-terminated PTO at 5 K. **a**, Current density J versus applied bias U in the range of ±200 mV. Shown are the measured data points for the ON (blue, after a +7 V pulse) and OFF (red, after a −7 V pulse) states respectively. The lines represent fitting curves with the Brinkman model. **b**, Same data as in a, but with logarithmic y-scale for the positive bias branch to better compare the currents and visualize TER values. **c**, Band diagram based on parameters from Brinkman fitting. The different shaded areas indentify the respective material, whereas the darker grey area represents the monolayer of PZO termination and the medium grey area the thickness difference of the ferroelectric barrier that results upon polarization reversal.

actual resistance states, which means that the low average potential barrier relates to the high resistance state and vice versa. The form of the drawn potentials hint at a strong dependence of the TER on asymmetric screening lengths, meaning that for the polarization down case (blue thick arrow in **Fig. 5.14 c**), the negative charges at the Co/PZO/PTO interface are much less effectively screened than anticipated. This is given due to the fact that in both prior discussed samples, the electric potentials were always smaller at the Co interface than at the LSMO side. Finally, the effective electron mass dependence on the ferroelectric polarization seems to have the strongest influence on the TER, resulting in this huge effect, which is unique amongst all measured samples.

The fact that, compared to the other junctions, rather large voltage amplitudes had to be applied in order to reach resistance saturation values is a result of the introduced PZO monolayer that probably acts as a spacer between ferroelectric and cobalt, which results in a damping of the applied electric field that drops across the PTO film. Although the antiferroelectric properties of PZO vanish for thinner layers than 10 nm [62], coupled to PTO, its electronic behavior cannot easily be predicted. A possible explanation, supported by the anticipated change of the effective screening length at the cobalt interface, could be a switchable metallization of PZO, depending on the underlying PTO polarization. This would explain the larger variation of the effective tunnel barrier thickness, compared to the tunnel structures based on PZT and PTO.

5.4.2 Tunnel magnetoresistance

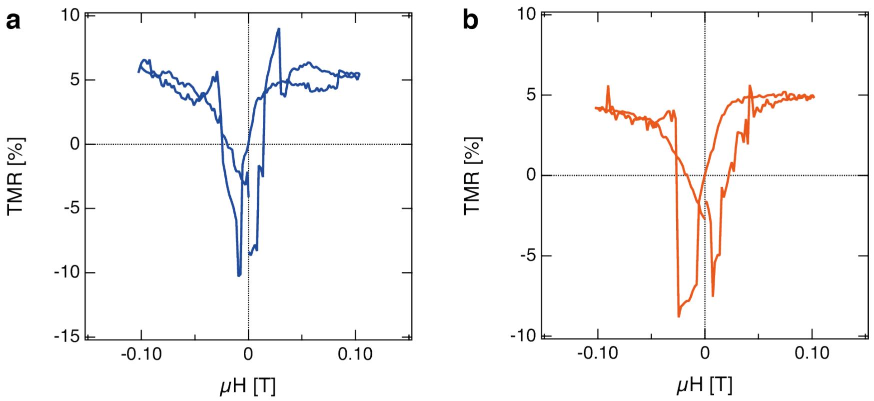

Figure 5.15: Tunnel magnetoresistance of PZO-terminated PTO at 5 K. TMR vs. applied magnetic field μH for the TER states ON (**a**) and OFF (**b**), respectively.

Again for the PZO-terminated PTO tunnel junction, the TMR was measured at 5 Kelvin with an applied bias of 150 mV. The big TER ratio, however, leading to extremely high resistances for the OFF state did not influence the relative TMR effect as it can be seen in **Fig. 5.15 a** and **b** on the loops that were measured for both ferroelectric resistive states. From peak to base line, the effect is about 15 %, which is again an indicator for a good spin filtering mechanism. The magnetic coercive fields in these measurements do not show strong signs of asymmetry, although FC was applied, which would mean that this composition does not possess strong antiferromagnetic contributors that would cause an EB effect on the TMR measurements.

The sign of the TMR is inverse and also unaffected by polarization reversal. It seems that in case of a magnetic proximity effect between cobalt and titanium, which shows asymmetric pinning and EB (see chapter **5.3.3** on page 62), one unit cell of PZO is able to successfully suppress it. Although in literature, asymmetric pinning was achieved by CoO/Co stacks with not less than 10 nm of cobalt [22], there is no evidence of any antiferromagnetic contribution in PZO terminated FE tunnel junctions, suggesting that antiferromagnetic contributors most likely stem from a Ti-Co interaction at the interface.

5.5 Tunnel anisotropic magnetoresistance of a copper capped junction

Another way of probing the interface is the replacement of the top electrode with another, nonmagnetic layer. For this purpose, the relatively well known PZT composition was used as a 3.1 nm thick ferroelectric tunnel barrier. Unlike cobalt, the copper electrode was deposited by thermal evaporation through a shutter mask with $60 \cdot 60\,\mu\text{m}^2$ capacitor size.

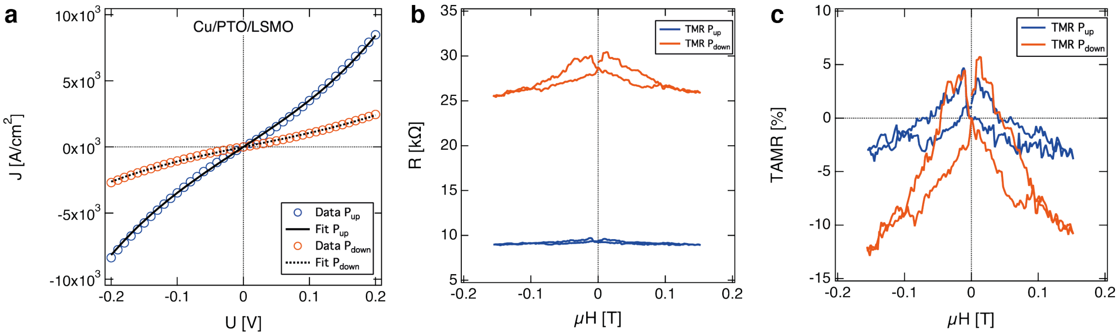

Figure 5.16: TER and TMR of a copper capped MFTJ. a, Current density J versus applied bias U in the range of ±200 mV. Like in the TER images before, the blue and red data points correspond to the measured current density values for the ON and OFF TER states, respectively. The lines inside this graph are the analytical fits with the Brinkman model. **b**, Resistance R versus applied magnetic field μH for both ferroelectric polarization directions ON (blue) and OFF (red). **c**, TMR in % over the applied magnetic field μH.

While the replacement of the cobalt layer by a copper electrode did not significantly change the TER properties (see **Table 5.1** on page 71), the observation of a (normal) tunnel magneto resistance is remarkable, yet anticipated (**Fig. 5.16**). Although two magnetic electrodes are necessary to obtain a spin filter in the TMR sense, the anisotropic magnetoresistance of LSMO alone can lead to a change in resistance of the tunnel junction and is then called tunnel anisotropic magnetoresistance (TAMR) [181]. In fact, since a tunnel junction is extremely interface sensitive, it is a very precise way to probe the change of the DOS of the ferromagnetic layer (in this case LSMO) at the FE interface in dependence of applied magnetic fields [182]. Due to the high amplitude of reported TAMR values, it is believed to be caused by a combination of uniaxial strain and Bychkov-Rashba spin-orbit interaction [183], which are only present at the 2-dimensional like interface [182, 184]. However, since the anisotropic magnetoresistance is very dependent on the in-plane magnetic field angle [181, 185], in case of tunnel structures, in-plane angle variation can even lead to a sign change of the TAMR [181, 182]. The absence of a vector magnetic field inside the used cryo prober thus did not allow angular magnetic-field dependent measurements, which is certainly an interesting approach to be addressed.

Reported TAMR values reach from negative (inverse) 11 % [182] up to positive (normal) 3 % [181] measured on Co/AlO$_X$/Al and (Ga,Mn)As/(Al,Ga)As/(Ga,Mn)As junctions, respectively. The measured values of TAMR vary in magnitude by a factor of more than 2, reaching from 7 % to almost 17 % (**Fig. 5.16, c**) and are thus comparable to reported values. The big change of TAMR upon ferroelectric polarization reversal is interesting, suggesting that spin dependent screening exists, which is supposed to be controllable by the dependence of spin transfer torque on the ferroelectric polarization direction [186].

5.6 Comparison of the measured junctions

In the following subsections, a comparison of all investigated samples and the effects they show will be presented. A focus on the differences of the engineered interface stoichiometries and the influence on TER and TMR effects shall be pointed out. Since the results of this work are primarily based on the fitting with the Brinkman model, the list of all used fitting parameters is given in **Table 5.1**.

System	Barrier thickness	Effective e$^-$ mass	$\Phi_{i,1}$	$\Phi_{i,2}$
Co/PZT (ON)	4.04 nm	0.27 m_e	0.40 eV	0.90 eV
Co/PZT (OFF)	4.11 nm	0.31 m_e	0.47 eV	0.80 eV
Co/PTO (ON)	3.09 nm	0.90 m_e	0.20 eV	0.49 eV
Co/PTO (OFF)	3.24 nm	0.92 m_e	0.10 eV	0.61 eV
Co/PZO/PTO (ON)	3.10 nm	0.69 m_e	0.94 eV	0.39 eV
Co/PZO/PTO (OFF)	3.22 nm	1.74 m_e	0.48 eV	0.40 eV
Cu/PZT (ON)	3.30 nm	0.42 m_e	0.79 eV	0.70 eV
Cu/PZT (OFF)	3.35 nm	0.44 m_e	0.66 eV	0.91 eV

Table 5.1: Brinkman fitting parameters of different tunnel junctions. - Summarizing the values of the fitting parameters.

5.6.1 Tunnel electro resistance

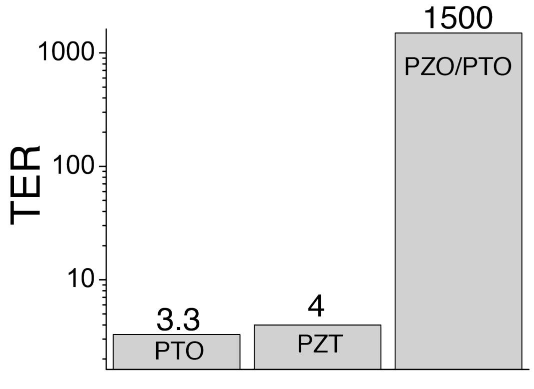

Figure 5.17: TER ratio versus zirconium content of the ferroelectric/Co interface. Semilogarithmic diagram of the TER ratio versus the measured ferroelectric tunnel barrier material.

Based on the presented measurements of ferroelectric tunnel junctions, it can be concluded that digital switching between the two TER resistance states is not caused by the size of the work functions at the interfaces alone. In all cases, one would anticipate an inverse resistance switching response to the applied voltage sign, based on the given values for Φ_i. This would mean that a positive voltage pulse should lead to a low resistance ON-state, because the average potential height of the tunnel junction is lower for polarization pointing towards the LSMO electrode (after positive voltage) than in the opposite case.

Fitting the IV-curves with the Brinkman model however, delivered that the thickness fitting-parameter d changes upon polarization reversal by up to 1.5 Å, whereas the effective electron mass m_e is rather constant for the PZT and pure PTO based tunnel junctions. For those two cases, the thickness variation is apparently the dominant contributor to the TER. In the PZO-terminated ferroelectric tunnel junction, the huge TER can be mainly contributed to the large change in the effective mass, which cannot be explained at this point.

The TER values for the three discussed junctions systematically increase with increasing amount of zirconium at the cobalt interface (see **Fig. 5.17**). Certainly, in case of PZT, the increase of the TER ratio $\frac{R_{OFF}}{R_{ON}}$ also results from the higher polarization value of PZT ($P \approx 105\,\frac{\mu\mathrm{C}}{\mathrm{cm}^2}$ [47]) compared to that of strained PTO ($P \approx 94\,\frac{\mu\mathrm{C}}{\mathrm{cm}^2}$ [187]). The huge effect of PZO-terminated PTO however, cannot be explained by an unrealistically large increase of ferroelectric polarization and thus must be contributed to a mechanism that exclusively originates from the cobalt-ferroelectric interface.

Although the fitting function 3.5.1 possesses several parameters, the good agreement with the measured data in all cases can be seen as good evidence for the reliability of this method.

5.6.2 Tunnel magnetoresistance

For all investigated FM/FE/FM samples, the effective size of the TMR is comparable. This leads to the assumption that the spin filtering process might be controlled mostly by the bottom LSMO electrode, which is supposed to be a perfect half metallic material [40, 41]. The sign of TMR though cannot be controlled by the interface stoichiometry, although the spin flipping effect in PZT tunnel junctions would supposedly mean that the interface to the cobalt electrode could lead to a change of spin polarized tunneling transport. However, the experimental data show that only in case of the PZT composition, a switch from inverse to normal TMR can be observed.

An asymmetric broadening of the TMR loops, meaning an asymmetric magnetic anisotropy of the sample, was already slightly visible on the data in the PZT case. Recalling **Fig. 5.6 b** one can see that a slight broadening of the TMR curve for negative applied magnetic fields, and of the blue curve for positive magnetic fields occurs. Although just tiny, it is observable that, besides the flip of spin polarization upon ferroelectric polarization reversal, also the unidirectional magnetic anisotropy changes sign. In case of the discussed picture of an induced magnetic momentum in titanium [24], this observation would mean that an induced antiferromagnetically coupled magnetic momentum inside the titanium at the interface would change sign by switching the ferroelectric polarization.

The two extreme cases of pure TiO_X- and ZrO_X-terminated ferroelectric interfaces with the cobalt top electrode show strong EB for PTO and no EB for the PZO terminated tunnel barrier. This finding is crucial in the explanation of where to search for a

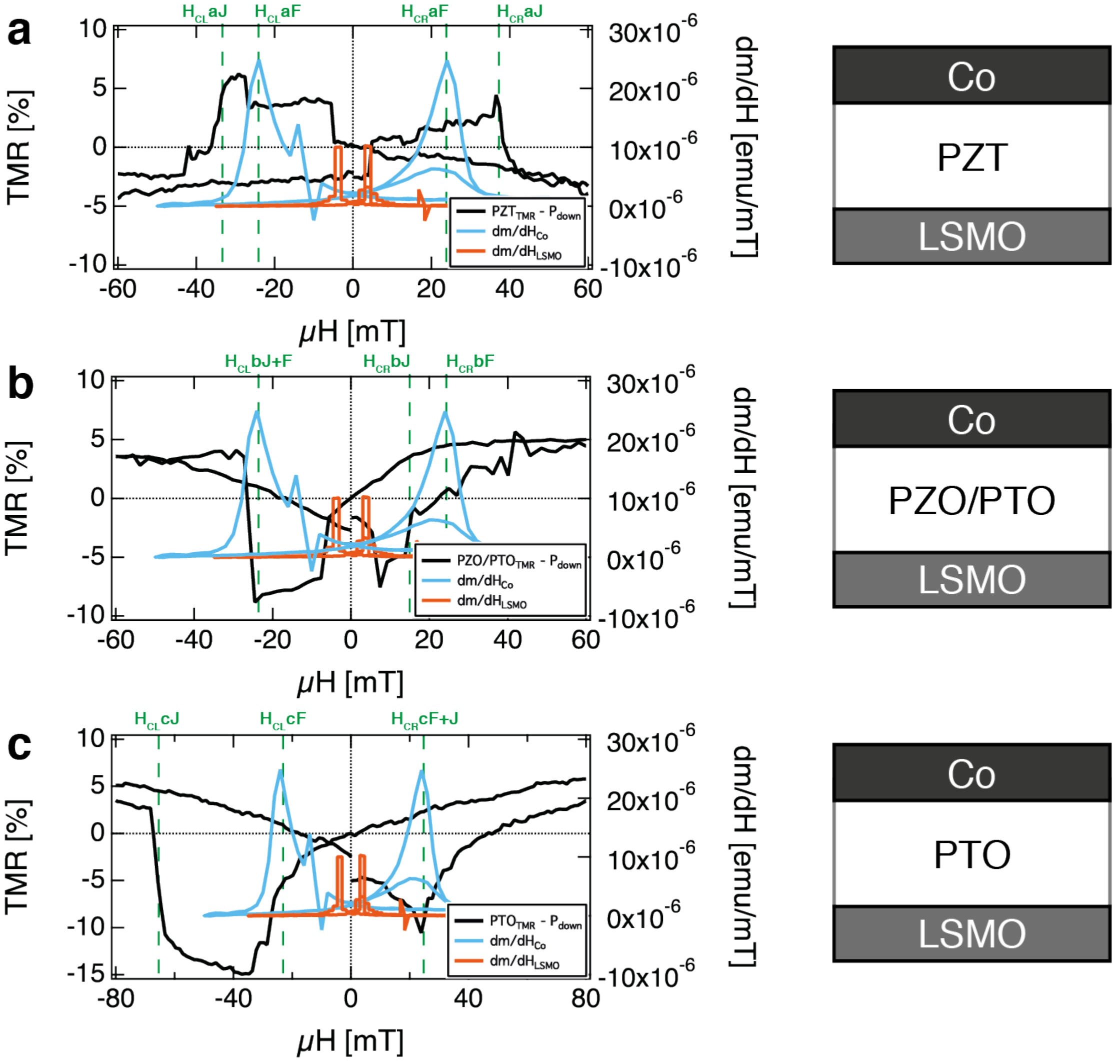

Figure 5.18: Comparison of the magnetic coercive fields of each layer in all junctions at 5 Kelvin. a-c, Overlays of the TMR and the derivative of the magnetization dm/dH versus applied magnetic field H. The TMR values are measurements of the discussed junctions (P_{down} state) in this chapter, the magnetization loops are taken from the SQUID measurements in chapter 4.5 on page 46. The dashed, green lines indicate the respective measured cobalt magnetic coercive fields H_{CL} for negative and H_{CR} for positive applied magnetic fields to junctions and films (J:= junction, F:= film). The shown TMR curves are measured on Co/PZT/LSMO (**a**, in section 5.2), Co/PZO/PTO/LSMO (**b**, in section 5.4) and Co/PTO/LSMO (**c**, in section 5.3) multiferroic tunnel junctions.

potential coupling between titanium and cobalt, which apparently shows a proximity effect not only by displacing them with PZO, but also upon polarization reversal in the PZT composition.

The magnetic coercive fields (interface coercive fields) of the junctions show, compared to the coercive fields that were macroscopically measured *via* SQUID (see chapter 4.5 on page 46), an interesting derivation in almost all cases (**Fig. 5.18**). For PZT (**Fig. 5.18, a**), the coercive fields of the hard magnetic electrode (presumably cobalt) is with $H_{CR}aJ - H_{CR}aF = 13.5\,\mathrm{mT}$ significantly larger in the tunnel junction ($H_{CL}aJ$ for negative magnetic field and $H_{CR}aJ$ for positive magnetic field) than in the SQUID measurements ($H_{CL}aF$ for negative magnetic field and $H_{CR}aF$ for positive magnetic field). The interface coercive fields of LSMO though (not marked in the figures, but comparable with help of the orange and black curves) do not seem to differ from the measured ones in the whole film. However, the situation changes completely with terminating the ferroelectric PTO layer with PZO (**Fig. 5.18, b**), where $H_{CL}bJ$ and $H_{CR}bJ$ become equal or smaller than the coercive fields $H_{CL}bF$ and $H_{CR}bF$ of the SQUID measurements. The asymmetric behavior of the coercive fields in this special case might be accounted to the relatively poor resolution, which is caused by the extremely low resistance of that junction. Obviously, the mechanism that increases the magnetic anisotropy of the hard and soft magnetic material in the tunnel junction is totally removed just by the insertion of the PZO monolayer.

The observed behavior becomes even more obvious, comparing the pure PTO terminated barrier TMR curves (**Fig. 5.18, c**) with the SQUID measurements. Here, the interface coercive fields of the interface magnetic anisotropy behave strongly different from the layer ones. The asymmetric broadening due to the supposedly unidirectional magnetic anisotropy and the offset of the crossing point in the TMR loop, which is caused by exchange bias, are dramatically different from that of the SQUID measurements. This could be seen as evidence to the fact that the observed EB effects in section 5.3 of this chapter are originating from the localized interface magnetic properties of the tunnel junction that are very different from the properties of the whole cobalt and LSMO films in the devices.

However, it must be stated at this point that the difference of the measured samples might occur due to the fact that they were actually physically different. Although nothing on the growth parameters changed and every characterizing method showed, in all of the samples, very good and comparable quality, the magnetic behavior might change a bit from sample to sample. A broader set of samples would be necessary in order to obtain statistics that would give rise to a much clearer answer. However, the importance of titanium at the interface is systematically present in all the executed experiments and as such it was worth to do this comparison, which supports the picture.

5.7 Summary of the chapter

Electroresistance effects of tunnel junctions comprising different FE material systems have been investigated magnetically, electrically and as a function of temperature. The conduction mechanism was shown to obtain many signs of proper direct electron tunneling, which makes the analyzing method of fitting voltage-current characteristics feasible by using the Brinkman model (see chapter 3.5.1). The influence of different contributors that lead to TER was separately discussed and a possible explanation for the found magnitude and sign of the TER was given. All MFTJs possess resistive responses upon magnetic field variation, resulting in observable TMR effects, from which all are inverse and, in case of the PZT-based tunnel junction, ferroelectrically switchable from inverse to normal. Investigations on a sample with a non-magnetic top electrode strongly suggest, in addition to theoretical predictions, that the FE/Co

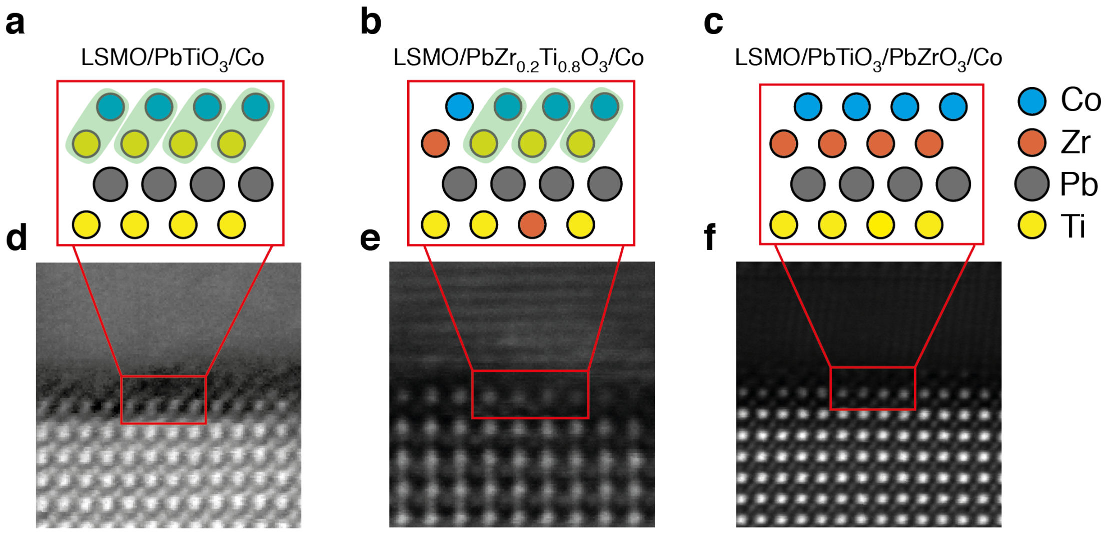

Figure 5.19: Interface-engineering summary. a - c, Schematics of the interface-atomic compositions of the engineered samples. The green shaped areas around the Co and Ti atoms should emphasize a potential coupling between the two elements. **d - f**, HAADF/STEM images of the respective interfaces.

interface is the source of the observed exchange biased phenomena.[1]

The chemical variation of interface stoichiometry at the cobalt interface (**Fig. 5.19**) lead to the observation of exchange bias in a tunnel junction only in case of a pure TiO_X terminated FE. It is remarkable that no junction possessed a deliberately introduced antiferromagnetic layer, which strongly suggests that EB stems only from the interfacial titanium. A comparison of the measured TMR loops with SQUID experiments gives more evidence that the EB originates from magnetic coupling phenomena that in turn originate from the interface of the ferroelectric to the cobalt electrode. The existence of such an intrinsic EB allowed the design of a four state multiferroic memory, combining the functionality of FTJs and MTJs.

As a result of the introduction of a PZO monolayer in between the FE PTO and magnetic top electrode, the TER was increased by several magnitudes. According to fits with the Brinkman model, this dramatic change is due to a large change in the effective mass, which might be explainable by a change of the type of charge carrier from electron to hole conduction.

---

[1] This will be further investigated with the help of synchrotron experiments in a later chapter.

6

The ferroelectric tunnel memristor

The possibility of analogously programming the resistance of a two-terminal device with short voltage pulses by utilizing Kolmogorov-Avrami-Ishibashi (KAI) [106, 188, 189, 190, 191] switching kinetics will be presented and the usability of the studied device as memristor will be discussed.

When electric pulse parameters are varied, the resistance of a ferroelectric tunnel junction can be tuned virtually analogously [18, 19]. In this chapter, the corresponding experimental results and analysis are presented. A model based on the simple analogy of parallel connected resistors is used to interpret the data. The programmability and analytic predictability of resistance states were tested, using KAI ferroelectric domain growth kinetics.

6.1 Dependence of resistive switching on pulse parameters

To access resistive states in between the already discussed digital TER states (**5.2.1**), parameters of the applied electric pulses have to be found that do not totally, but partially switch the ferroelectric domains of the tunnel barrier. Although all investigated samples in chapter **5** demonstrate the reproducibility of this effect, the present studied junction was grown by Daniel Pantel during his work on multiferroic tunnel junctions before me. The device possesses a 3.2 nm thick PZT ferroelectric tunnel barrier confined between two ferromagnetic materials cobalt and LSMO that are used as top and bottom electrodes, respectively. Magnetic and electric properties of this sample have already been studied exhaustively in the above mentioned Phd thesis [192]. It possesses a digital TER ratio of about 4, which is comparable in sign and magnitude with the result presented on a similar tunnel junction in the present thesis. The fundamental mechanisms that lead to TER should be identical due to its identical structural and chemical properties.

As is illustrated in **Fig. 6.1**, the measurements were performed by applying a voltage train similar to that of the PUND method [193]. First, the tunnel junction was set into a predefined reference state by applying a sufficiently strong electric pulse (reset pulse) that switched the system into fully saturated resistance ON or OFF. To give the system enough time to relax into a stable and remanent resistive state, a delay time of several seconds was executed before the next pulse was applied. During that

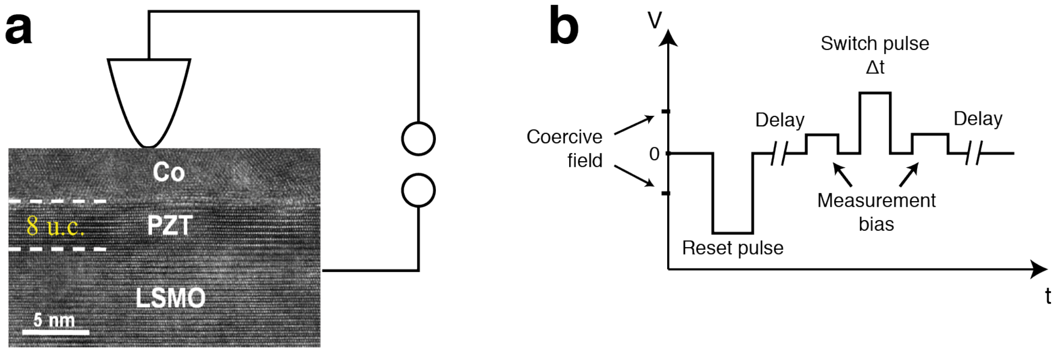

Figure 6.1: Programming and readout pulse chain for ferroelectric tunnel memristors. a, Sketch of the measuring geometry on a HRTEM image. The leads represent the probe that connects to the top cobalt electrode, and the back contact to the LSMO, which is realized *via* silver paste. **b**, Applied voltage train over time. The measurement bias has a lower, the switch and reset pulses have a higher amplitude than the coercive field of the ferroelectric.

time the system was short-circuited to ground potential to allow charge carriers to move freely. Afterwards the resistance was measured by applying a small electric bias well below the coercive field of the ferroelectric in order to confirm the stability of the reference points. The follow-up pulse, called the switching or programming pulse, sets the system into a different resistive state, based on its parameters "pulse width Δt" and "amplitude $U_{pr.}$". Immediately after the programming pulse, the measurement was performed in order to observe potential backswitching phenomena.

The resulting resistance response at room temperature of the above described sample can be seen in **Fig. 6.2**. After (re-)setting the tunnel junction into a low resistance reference state (blue data points) with a negative bias of -5 V and constant pulse width of 10 ms, positive electric pulses of $+6$ V lead to a gradual increase of the junction resistance upon increasing of the pulse width. The successive back-and-forth switching and the effect on the resistance evolution is demonstrated in the closeup (**Fig. 6.2 b**).

To minimize the total amount of pulses over multiple decades of pulse widths, only ten programming processes (switching into reference state plus switching into programmed state) were performed per decade, leading to a total number of 126 switching processes for the obtained data in **Fig. 6.2**. However, for low pulse widths (less than 10^{-6} s), a tendency to lower values of the reference resistance is observable with increasing pulse width. For long pulse widths though, both the programmed, saturated resistance (red) and reference resistance systematically turn to higher values. It seems as if the system possesses a second order hysteretic behavior dependent on the total amount of current that passed through the junction. This systematic change though is not comparable to the size of change in resistance, which is contributed to the TER and thus is not further relevant and discussed.

As reported in literature, switching phenomena in thin film (50 nm to 230 nm) PZT can be described well with the KAI theory of domain formation and domain wall propagation [54]. However, the readout mechanism of the reported studies did not allow to investigate PZT ultrathin films in the nanometer range of thin film thickness due to the fact that tunnel transport phenomena would override any contribution of displacement current of the film and thus not allow to separate the different contributions.

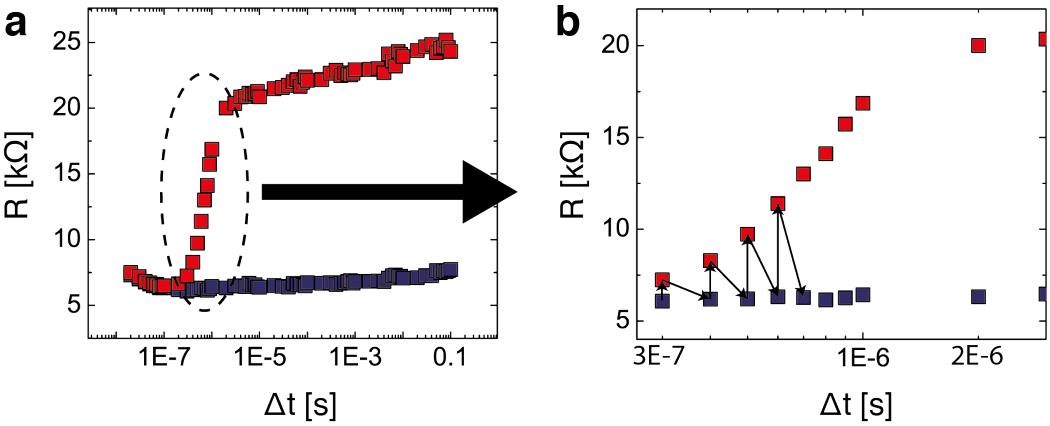

Figure 6.2: Continuous resistance change of a MFTJ by application of short voltage pulses at room temperature. a, Semilogarithmic plot of junction resistance $R\,[\Omega]$ versus pulse width Δt [s] for a relatively big pulse width window up to 100 ms. Each high resistance state (red) is set coming from a reference low resistance state (blue). This back- and forth switching is emphasized in the smaller scaled graph **b**.

What would be called leakage (tunnel) current in that case, is in present case used as the (non-destructive) measuring signal. Based on TER and with knowledge of the fully saturated resistance states, it is possible to conclude that the amount of switched domains leads to the intermediate resistance states (between R_{ON} and R_{OFF}).

6.2 Describing memristive behavior with KAI-domain growth kinetics

One way of showing that the resistance varies according to the amount of switched domains is to visualize them *via* PFM and simultaneously measure the tunnel resistance as it was done by Chanthbouala et al. [18]. In that referred work it was also stated for the first time that the tunnel resistance versus amount of switched domains can be described with a variation of the KAI model that could explain "wavy behavior" of the resistance transients that were not observed in our experiments.

After measuring the saturation values for the resistance states ON (R_{ON}) and OFF (R_{OFF}), the data were normalized with:

$$R_N = \frac{R - R_{ON}}{R_{OFF} - R_{ON}} \tag{6.1}$$

To develop a characteristic function based on the KAI model, which is able to predict a resistance state based on the parameters of the applied bias $\Delta\, t$ and $U_{pr.}$, coexisting ferroelectric domains of opposite polarization are considered as parallel connected resistors.[1] As shown on the schematics in **Fig. 6.3**, the investigated junction should possess domains of both polarization directions $P_{\downarrow}$ (red, high resistance domains) and $P_{\uparrow}$ (yellow, low resistance domains) at an intermediate resistance state.

---

[1] This approach was also used in [18] to model the relative fraction of certain ferroelectric domains.

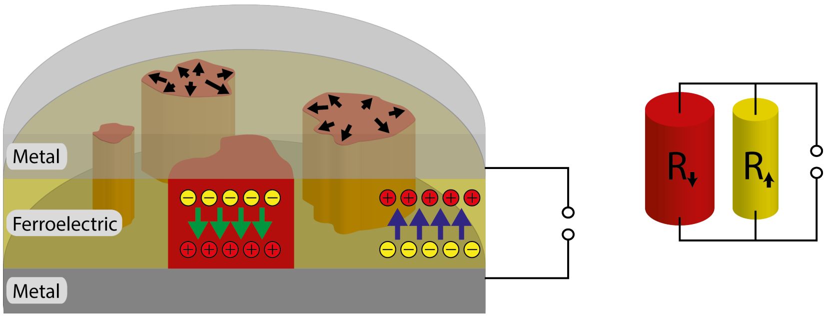

Figure 6.3: Schematics of two-dimensional domain growth. Visualization of ferroelectric domains inside a metal-ferroelectric-metal junction cross section. The yellow area is the ferroelectric ultrathin film with polarization pointing up, the red areas represent domains of the opposite polarization direction. The two parallel connected resistors emphasize the assumption that areas of opposite polarization direction act as resistors of different resistance.

Summarizing the resistance contributions R_d of all ferroelectric domains leads to the values $R_\downarrow = \sum_{i=1}^{N_\downarrow} R_{d,i,\downarrow}$ and $R_\uparrow = \sum_{i=1}^{N_\uparrow} R_{d,i,\uparrow}$, whereas the arrow index notation represents the polarization direction, the index i a certain domain and N the number of domains. Based on these resistance values and the normalized polarization $P_{norm}(t) = \frac{P_\downarrow(t)}{P_S}$ (see chapter 2.4.1 on page 13), a simple equation can be written:

$$\frac{1}{R} = \frac{1}{R_\downarrow} + \frac{1}{R_\uparrow} = \frac{1 - P_{norm}}{R_{ON}} + \frac{P_{norm}}{R_{OFF}} \tag{6.2}$$

Inserting **Equation 6.2** into **Equation 6.1** finally leads to a function for the normalized resistance:

$$R_N = \frac{R_{ON} \cdot P_{norm}}{R_{OFF} + (R_{ON} - R_{OFF}) \cdot P_{norm}} = \frac{R_{ON}}{R_{OFF}} \cdot \frac{P_{norm}}{1 + \left(\frac{R_{ON}}{R_{OFF}} - 1\right) \cdot P_{norm}} \tag{6.3}$$

Which simplifies for very big TER to:

$$R_N \approx \frac{R_{ON}}{R_{OFF}} \cdot \frac{P_{norm}}{1 - P_{norm}} \tag{6.4}$$

The function R_N can now be written in dependence of the pulse parameters using the KAI model (see chapter 2.4.1):

$$R_N \approx \frac{R_{ON}}{R_{OFF}} \cdot \frac{1 - e^{-\left(\frac{t}{\tau}\right)^2}}{1 - \left(1 - e^{-\left(\frac{t}{\tau}\right)^2}\right)} \approx \frac{R_{ON}}{R_{OFF}} \cdot \left(e^{\left(\frac{t}{\tau}\right)^2} + 1\right) \tag{6.5}$$

Equation 6.5 is used to fit the normalized data in **Fig. 6.2** for different pulse amplitudes. In **Fig. 6.4 a** the resulting curves are shown together with the corresponding data points. As expected, the fitting parameter τ decreases with increasing applied voltage (**Fig. 6.4 b**), meaning that the two-dimensional domain wall propagation and thus the switching process accelerates.

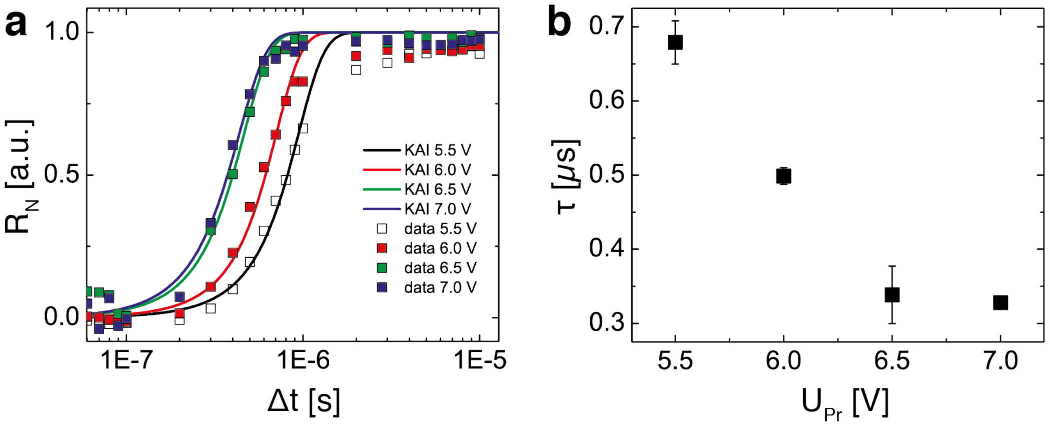

Figure 6.4: Fitting with the KAI model. a, Semilogarithmic plot of the normalized resistance R_N versus pulse witdh Δt for several different pulse amplitudes $U_{pr.}$ (color coded) including data points (symbols) and fits (lines) **b**, Fitting parameter τ versus pulse amplitude $U_{pr.}$.

The good agreement of the fitting curves and the data allows the assumption that the characteristic transfer function (**Equation 6.5**) can be used as a valid analytical prediction and thus delivers a way of programming any desired resistance state, which is just based on two parameters, viz. pulse voltage and width.

6.3 Programming of resistance states

To further support experimentally the analytical behavior of the system, it has to be shown that the total accumulated pulse time t_{acc} should always lead to the same resistance state, independently from the number and width of pulses that lead to this value. Mathematically this means $t_{acc} = \sum_{n} \Delta t$ with $n = \frac{t_{acc}}{\Delta t}$. In order to do so, the above measured sample was set into the reference state ON, followed by a successive train of pulses of constant width Δt until the opposite saturation state OFF was eventually reached. Between each voltage pulse, a waiting time of 20 s was carried out during which the resistance was continuously measured with an applied voltage of +100 mV (**Fig. 6.5 a**).

This experiment has been performed with two voltage pulse widths of $\Delta t_a = 0.8\,\mu$s and $\Delta t_b = 2{\cdot}\Delta t_a = 1.6\,\mu$s. According to the predicted analytical behavior, it can clearly be seen that, after a certain relaxation time, the resistance states of both curves settle to the same value for the same accumulated pulse width.

Although it can be stated that after the waiting time of 20 s the system relaxed into a relatively stable resistance state, resistance transients are rather obvious. To quantify the decay time of such an excited resistance state into the stable remanent state, an exponential fit (**Fig. 6.5 b**) was carried out with the data of one of the transients (green circle in **Fig. 6.5 a**). The exponential fit delivered fitting parameters for the decay time $\tau_d = 14.75\,\mathrm{s} \ \pm 3.57\,\mathrm{s}$ and the remanent resistance value $10.6\,\mathrm{k\Omega} \ \pm 0.08\,\mathrm{k\Omega}$. According to literature, backswitching of ferroelectric polarization is dependent on film thickness and applied bias during the readout process and it was demonstrated that

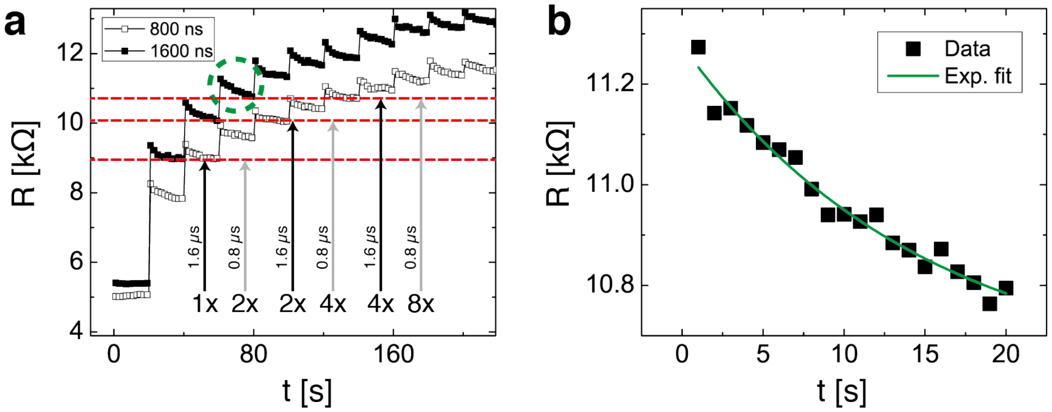

Figure 6.5: Testing the analytical behavior of the memristor. a, Resistance versus time plot for a ferroelectric tunnel junction. Every 20 seconds, a pulse of +6 V and constant width has been applied, until the saturated OFF state was reached. The experiment was repeated for two pulse widths of 800 ns (grey symbols) and 1600 ns (black symbols). The red dashed lines indicate the resistance states, where the accumulated pulse times from both runs match. **b**, Exponential fitting (green line) of one of the transients, marked by a green dashed circle in **a**.

electric biases of as low as 100 mV lead to a large increase of the backswitching time (in the tens of seconds region), due to depolarization field compensation [194].

6.4 Ferroelectric tunnel memristor in the context of other memristive devices

The resistive switching mechanism of most realized memristors is based on the continuous motion of the conduction front inside a capacitor [6, 29, 195] and filament formation [70, 196, 197, 198, 199], which can be classified into (bi-)polar and non polar memristive devices [9], respectively. The mechanism of bipolar memristors is mainly characterized by the migration of a conductive zone in current flow direction, which is attributed to be an electric field-dominated process. A fingerprint of these memristor types is the unique form of IV hysteresis curves, which are pinched with a frequency-dependent opening, being the largest for low and smallest for high frequencies [199]. The ferroelectric tunnel memristor investigated in this work would, following that classification, fall into the category of thermally dominated memristive devices, which is clearly not the case here.

The main difference of ferroelectric tunnel memristors compared to memristors based on filament formation [70, 199] and charge doping drift [29] is the threshold in voltage, namely the coercive (ferro-)electric field, which distinguishes between wether or not the resistance of a devise is changed. With further improvement of resistance retention, this could be the main advantage compared to other kinds of memristors, allowing to operate it as a normal TER device with reliable memory functionality and memristance.

The limiting factors of ferroelectric tunnel memristors are on the other hand their downsizing capabilities. Since in this work, junctions of relatively large ferroelectric thin film area ($3600\,\mu\text{m}^2$) are being measured, the dominant ferroelectric switching process is given by domain wall kinetics, rather than nucleation, and thus allows to state that the partial switching of resistance is (semi) analogue. Downsizing the capacitor area is therefore limited by the finite size of nuclei, the contribution of which to the switching process increases with smaller capacitor sizes. The extreme case, a capacitor with surface area of only one plane of a ferroelectric unit cell, would again be a digital TER switch, without any memristive properties.

Based on the size of ferroelectric nuclei (ferroelectric stable domains have been realized down to 40 nm width, [200]), one could estimate the minimal size of a capacitor area with $A_c = m \cdot A_m$ and desired resistance increment $\Delta R \propto \frac{1}{m}$, where m is the number of nuclei with area A_m and A_c the capacitor area, assuming that the shape does not contribute. A pseudo analogue memristor with 20 resistance increments would therefore have a minimal area of $0.004\,\mu\text{m}^2$. However, it is shown that ferroelectric domain wall kinetics are dependent on shape and size of the capacitor, allowing the existence of vortex domains that can lead to domain wall propagation-dominated switching inside very small devices in the submicrometer width regime [201].

6.5 Summary of the chapter

Exploiting the two-dimensional ferroelectric domain growth according to the KAI growth kinetic model, a programmable ferroelectric tunnel memristor based on multiferroic tunnel junctions was presented. The readout process of this two-terminal device is, based on fundamental ferroelectric properties, non destructive and thus different from other types of memristors, where the current through the system always changes the resistance. This threshold between non destructive readout- and programming voltage allows to potentially combine the functionalities of TER and memristors.

7

Synchrotron experiments on multiferroic heterostructures

This chapter will present and discuss a set of synchrotron measurements that were performed at BESSY II in Berlin. The main motivation was to experimentally prove whether the anticipated magnetic moment of the titanium at the cobalt interface exists, as it was discussed in Chapter 5, and how it behaves as a function of the ferroelectric polarization. For better insights at the interfaces, reflectivity measurements were carried out on three different samples, comprising the aforediscussed heterostructures Co/PZT/LSMO, Co/PTO/LSMO and Co/PZO/PTO/LSMO. The latter two samples were fabricated with ferroelectric barriers of a tunnel junction thickness of around 6-7 unit cells and un-patterned cobalt films of around 80 nm thickness. The first one (PZT), was fabricated to investigate the magnetic behavior as a function of ferroelectric polarization reversal and thus comprises a much thicker (around 80 nm) ferroelectric film deposited on LSMO and covered with 60 nm of cobalt. To ensure a full polarization on the measured area, the cobalt layer of the PZT sample was specially patterned (see Section 3.1.4) and polarized (see **Fig. 7.1 a**) using a probing station together with a thin-film analyzer TF-2000 from AixAcct, Aachen. To obtain a remanent polarization, the devices were first switched successively into both FE polarization states measuring hysteresis loops at the same time to confirm their ferroelectricity like it is described in Section 4.3.1.

This approach rather than *in situ* switching has been chosen, because it was impossible to adjust the polarization in a controlled and measurable way with *in situ* contacting during that time, due to the necessary huge top electrode and the resulting large leakage current. The relatively large thickness of 60 nm cobalt was chosen to make sure that possible interface related magnetic coupling mechanisms are not influenced by any cobalt oxidation at the top of the sample. The passivation layer of an up to 1 nm thick Co(OH)$_2$ film that forms after several seconds [173], ensures that no antiferromagnetic "pinning layers" [157], which have the potential to induce exchange bias [174], can influence the magnetoelectric effects at the cobalt-ferroelectric interface.

Reflectivity experiments give the possibility to probe magnetism of buried layers and interfaces and to perform element-selective magnetic hysteresis curves. Conclusions about the coercive fields and the relative strength of the measurement signals for cobalt and titanium can thus be drawn.

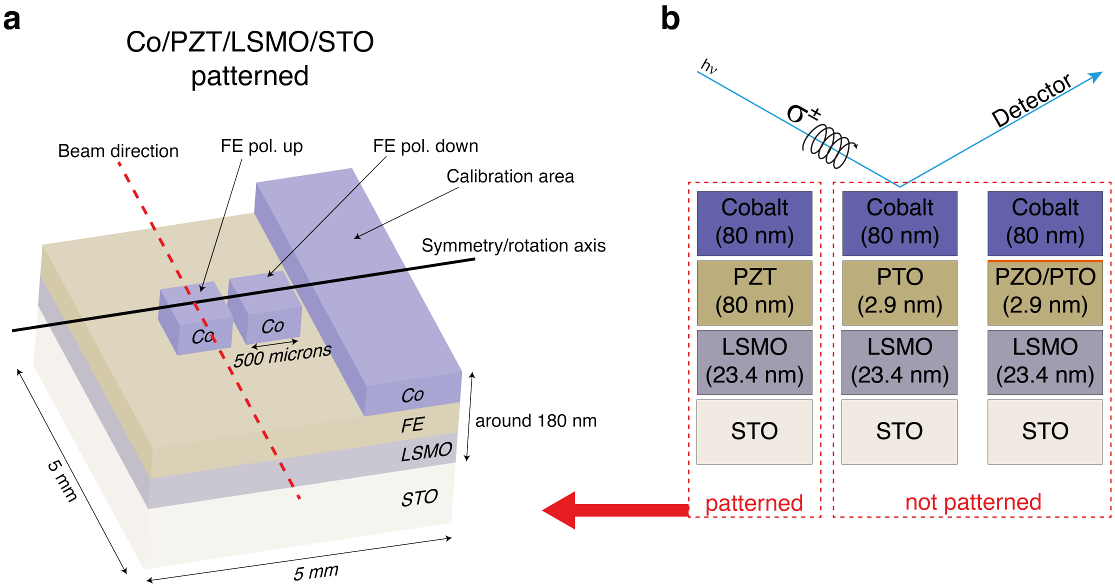

Figure 7.1: Sketch of the measured samples. a, Scheme of the specially designed sample structure to measure the effect of the FE polarization on the induced interfacial magnetic moments. The two patches of $500 \cdot 500\,\mu\mathrm{m}^2$ area are oppositely polarized. **b**, The stacking structure of the samples presented in this chapter is, from top to bottom: Cobalt - the ferroelectric - LSMO and the substrate STO.

7.1 Magnetic characterization of the cobalt layer

All investigated samples own cobalt top electrodes of very similar good surface quality, resulting in high signal reflectivity measurements. This can be concluded from the relatively large reflectivity angles that were still measurable on the unpolarized (calibration) PZT sample (**Fig. 7.1 a**) at the cobalt $L_{3,2} \approx 780\,\mathrm{eV}$ edge (see **Fig. 7.2 a, b**) of up to $2\Theta = 30\,°$. The result of the reflectivity measurement is presented in the semilogarithmic plot in **Fig. 7.2 a** where each curve is measured for a different applied magnetic field. To separate the magnetic part of the reflectivity from the charge one, the so called asymmetry has to be calculated as follows:

$$I_{asymm.} = \frac{I_{\sigma^-} - I_{\sigma^+}}{I_{\sigma^-} + I_{\sigma^+}} \tag{7.1}$$

where I_{σ^+} and I_{σ^-} are the measured intensities for the equivalent helicity signals σ^+ and σ^-. The orange and blue colored curves in **Fig. 7.2** are actually not measured with opposite helicity of the circular light polarization, but with two opposite applied in-plane saturating magnetic fields of $\mu H = \pm 100\,\mathrm{mT}$, which is equivalent to measuring in a constant applied magnetic field in one direction and switching the helicity of the light polarization (see Section 2.5.2).

Interestingly, the asymmetry (see **Fig. 7.2 b**) of the measured reflectivity curves changes sign at an angle of around $2\Theta \approx 15\,°$. For this reason, energy spectra (E-spectra) measurements were carried out with positive and negative applied magnetic fields of $\pm 100\,\mathrm{mT}$ and with σ^+ at angles of $2\Theta = 10\,°$ and $2\Theta = 20\,°$, which are plotted in **Fig. 7.2 c** and **d**, respectively. It is rather obvious that the E-spectra for both measured reflectivity angles are quite different, with different features and strongly

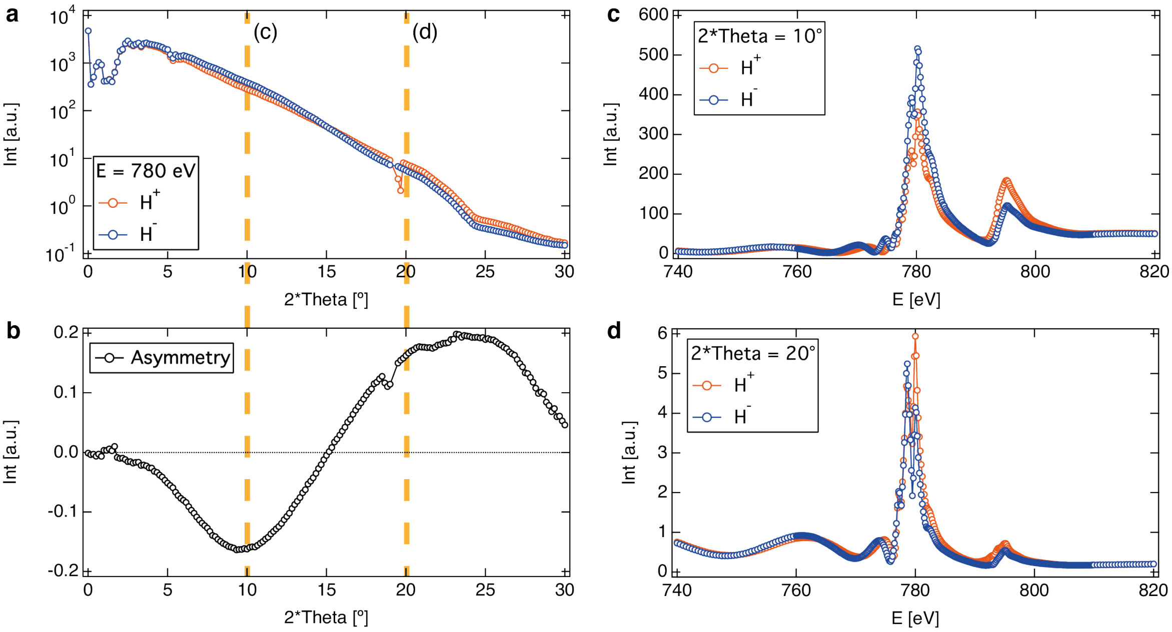

Figure 7.2: Energy and reflectivity scans measured at the Co$_{3,2}$ edges. a, $\Theta - 2\Theta$ scans at the cobalt L$_3 \approx 780\,$eV edge with two different applied magnetic fields. The two examined angles $2\Theta = 10^\circ$ and $2\Theta = 20^\circ$ are marked by the vertical yellow, dashed lines. **b**, Calculated asymmetry. **c** and **d**, Energy spectra performed in reflection at angles of $2\Theta = 10^\circ$ and $2\Theta = 20^\circ$ respectively. The orange and blue lines are the signals with positive (orange) and negative (blue) applied magnetic field.

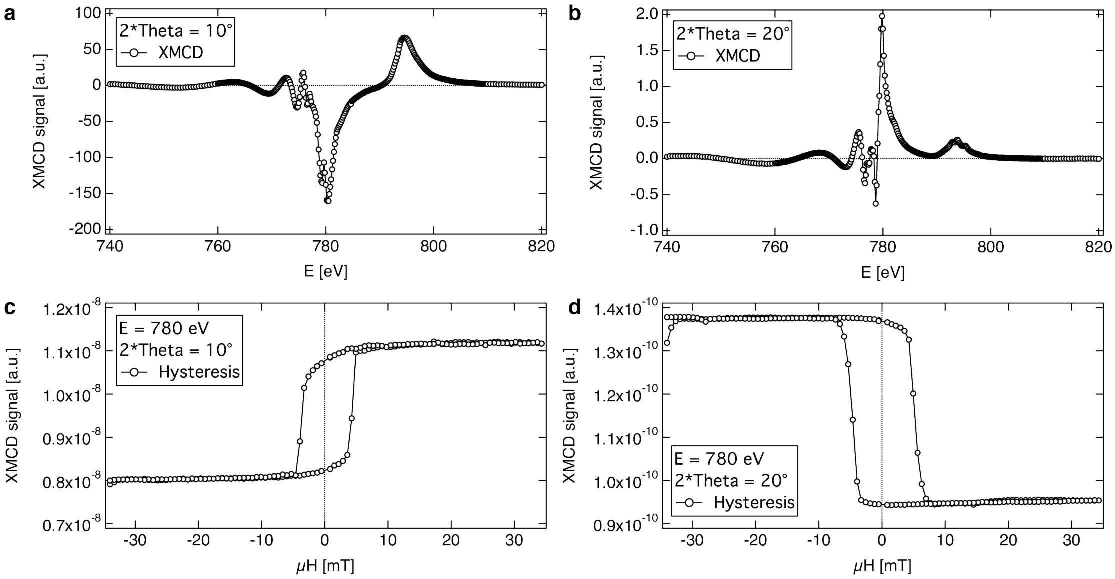

Figure 7.3: XMCD signal of the cobalt top electrode. a and **b**, XMCD signals (difference $\sigma^+ - \sigma^-$) versus photon energy E [eV] for the two reflectivity angles $2\Theta = 10^\circ$ and $2\Theta = 20^\circ$, respectively. **c** and **d**, Magnetic hysteresis loops according to **a** and **b**.

different signal strengths. The latter observation is mainly a result of the intrinsic signal weakening due to the increase of the reflectivity angle.

The asymmetry (see equation 7.1) of the data in **Fig. 7.2 c** and **d** as a function of the photon energy resembles the XMCD signals of cobalt and is shown in **Fig. 7.3 a** and **b**. The visible double-peak feature in **Fig. 7.3 a** indicates the already discussed presence of CoO_X of the sample, which, however, does not show contributive exchange bias for the whole sample.

A true proof of the break in time reversal symmetry is obtained by measuring element selectively magnetic hysteresis curves that show remanence at zero applied fields. Therefore, magnetic hysteresis curves have been measured at a constant photon energy at the cobalt $L_{3,2}$ edge of 780 eV and for the two reflectivity angles $2\Theta = 10°$ and $2\Theta = 20°$. As it can be seen on **Fig. 7.3 c** and **d**, the coercive fields of the cobalt thin film are with $H_C = \pm 5\,\mathrm{mT}$ very well comparable with the previously reported values, measured *via* SQUID. The small difference however could be caused by a slight calibration error of the magnet at BESSYII.

Following the sign change in the reflectivity curves in **Fig. 7.2 a** that occurs between the two angles $2\Theta = 10\,°$ and $2\Theta = 20\,°$, the measured hysteresis curves change their direction accordingly. At a reflectivity angle of $2\Theta = 10\,°$ (**Fig. 7.3 c**), the hysteresis curve possesses a high signal for positive applied magnetic field and weak signal for negative applied magnetic field. At the higher reflectivity angle of $2\Theta = 20\,°$ (**Fig. 7.3 d**) the situation is exactly opposite. Again, the significantly lower signal strength for the hysteresis curve measured at $2\Theta = 20\,°$ is due to the decrease in signal strength with increasing angles as discussed above.

As a result, ferromagnetism of the cobalt electrode is demonstrated for all films without the observation of any exchange biasing effects, which would, however, not be anticipated anyway at room temperature.

7.2 Co/PZT interface magnetism

In proximity to ferromagnets, non-magnetic elements can become ferromagnetic, which has been proven *via* element selective magnetic measurements at synchrotron facilities. A special case is the induced magnetic momentum of the interfacial titanium within a ferroelectric perovskite structure, which can vary upon the direction of the ferroelectric polarization as it was shown in a recent work on BTO [202]. Moreover, *ab initio* calculations of the group of Prof. I. Mertig at Halle University were partly the motivation of a deeper investigation of the magnetic properties at the Co/PZT interface, allowing further discussion around the origin of the spin flip effect (discussed in Section 5.2.2 on page 58) [24].

For that reason, similarly to the cobalt measurements in Section 7.1, the reflectivity curves σ^+ and σ^- for titanium were first measured on the unpolarized sample (see **Fig. 7.1 a**) by selecting the $E = 460\,\mathrm{eV}$ edge of Ti [202]. As it can be seen on **Fig. 7.4 a** and **b**, the reflectivity curves are not easily separable, though the asymmetry shows clear oscillatory behavior in the higher reflectivity angle region between $2\Theta \approx 15°$ and $2\Theta \approx 30°$.

Although magnetism is already visible in the calculated asymmetry from the reflectivity scans, two angles, one showing positive and another negative asymmetry values were chosen from the E-scans. If the two curves for σ^+ and σ^- would possess a constant offset, the resulting XMCD spectra would not show a sign change according to the two

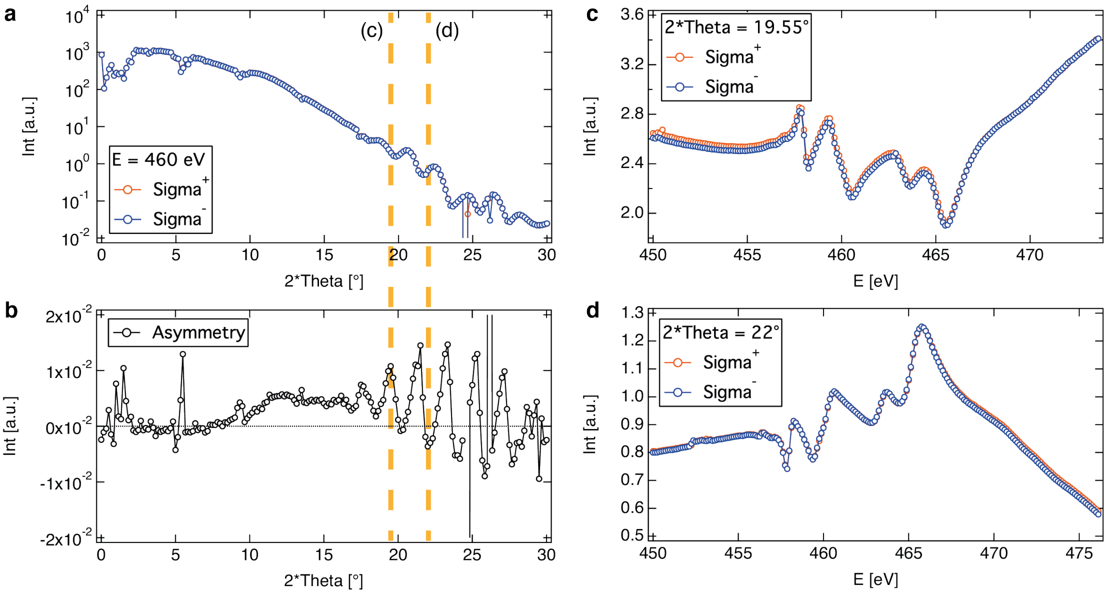

Figure 7.4: Reflectivity and energy scans at Ti edges. **a**, $\Theta-2\Theta$ scans for titanium $E \approx 460\,\mathrm{eV}$ for two light helicities σ^+ and σ^-. The two examined angles $2\Theta = 19.55°$ and $2\Theta = 22°$ are marked by the vertical yellow, dashed lines. **b**, Calculated asymmetry of the signals in **a**. **c** and **d**, Energy spectra performed in reflection at the angles of $2\Theta = 19.55°$ and $2\Theta = 22°$, respectively. The orange and blue lines are the signals with positive (orange) and negative (blue) applied magnetic field.

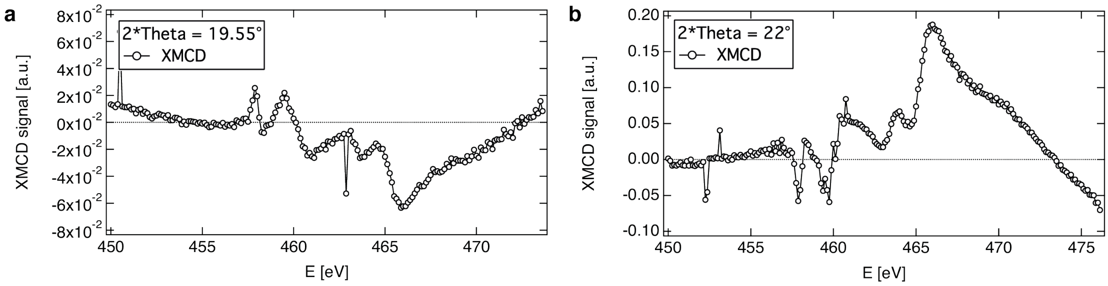

Figure 7.5: XMCD energy scans at Ti edges. **a** and **b**, XMCD signals (difference $\sigma^+ - \sigma^-$) versus photon energy E [eV] for the two reflectivity angles $2\Theta = 19.55°$ and $2\Theta = 22°$, respectively.

chosen angles. At the angles $2\Theta = 19.55°$ and $2\Theta = 22°$, energy scans were performed, which seem to be symmetric reflections at the energy axis from one another (see **Fig. 7.4 c** and **d**).

The XMCD signals presented in **Fig. 7.5** look like systematic difference of the σ^+ and σ^- curves in **Fig. 7.4 c** and **d**. It is therefore important to demonstrate potential ferromagnetic properties *via* element selective XRMS signal hysteresis curves.

Due to the relatively good signal strength at a reflectivity angle of $2\Theta = 19.55°$, two hysteresis curves were measured at the $E \approx 460\,\mathrm{eV}$ titanium edge. This time, the helicity of the circular polarized X-rays was changed, leading to true σ^+ and σ^- hysteresis loop signals in **Fig 7.6**. This is the main evidence for the existence of ferromagnetism in titanium, a clear consequence of the proximity with the ferromagnetic

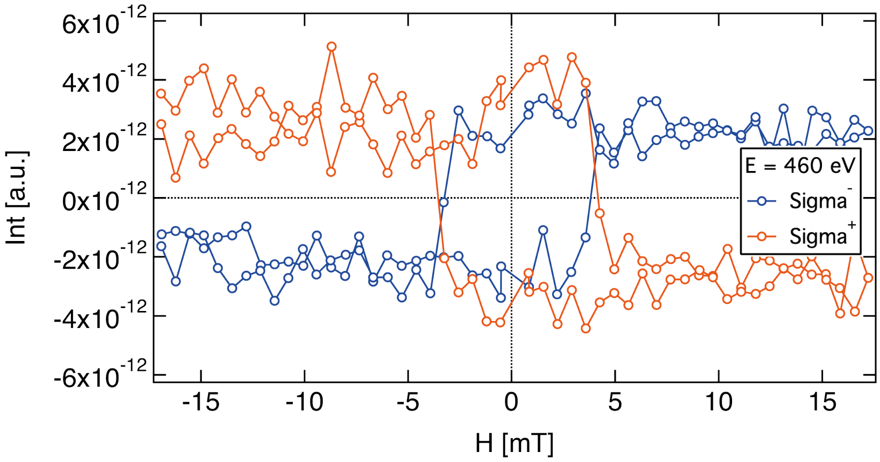

Figure 7.6: Titanium hysteresis loops with opposite light polarization. Magnetic hysteresis loops with opposite circular light polarization, measured at the FE unpolarized PZT sample at an angle of $2\Theta = 19.55°$.

Co layer.

7.2.1 Dependence of the induced interfacial magnetic momentum on the ferroelectric polarization direction

At this point the influence of the FE polarization direction on the already proven induced magnetic moment in titanium shall be investigated. The alignment of the relatively small ($500 \cdot 500\,\mu\mathrm{m}^2$) areas into the X-ray beam ($100 - 120\,\mu\mathrm{m}$) has been performed using the reflected signal at the $L_3 \approx 780\,\mathrm{eV}$ edge of cobalt.

The reflectivity spectra of titanium in the cases of ferroelectric polarization up (P_{up}) and down (P_{down}) are presented in **Fig. 7.7**. It is already visible that the ferroelectric polarization does have a significant effect on the form of the reflectivity curves measured for titanium at $E \approx 460\,\mathrm{eV}$ (**Fig. 7.7 a** and **b**) and on the resulting asymmetry curves (**Fig. 7.7 c** and **d**). For ferroelectric polarization pointing towards the cobalt electrode (P_{up}), the magnetic signal seems to be much stronger than for the opposite polarization direction. Like for the unpolarized part of the sample, the induced ferromagnetism can be proven by showing hysteretic behavior of titanium upon application of magnetic fields.

The left column of **Fig. 7.8** shows the hysteresis loops measured for the sample polarization pointing up (towards the cobalt electrode) and for different points on the reflectivity curves. These points were chosen because of the features of the asymmetry; the sign of the hysteresis curves follows directly the positive-negative behavior of it (see yellow, dashed lines in **Fig. 7.7 c**).

The right column of **Fig. 7.8** shows the same type of hysteresis loops measured for the sample polarization pointing down (towards the LSMO electrode). Since the signal is small and there are no positive-negative features in the asymmetry curve (see **Fig. 7.7 d**), the two measured points were chosen to be close to two points of the opposite polarization measurements in the left column for comparison.

One can identify the direction of the observed hysteresis curves in the cases **Fig.**

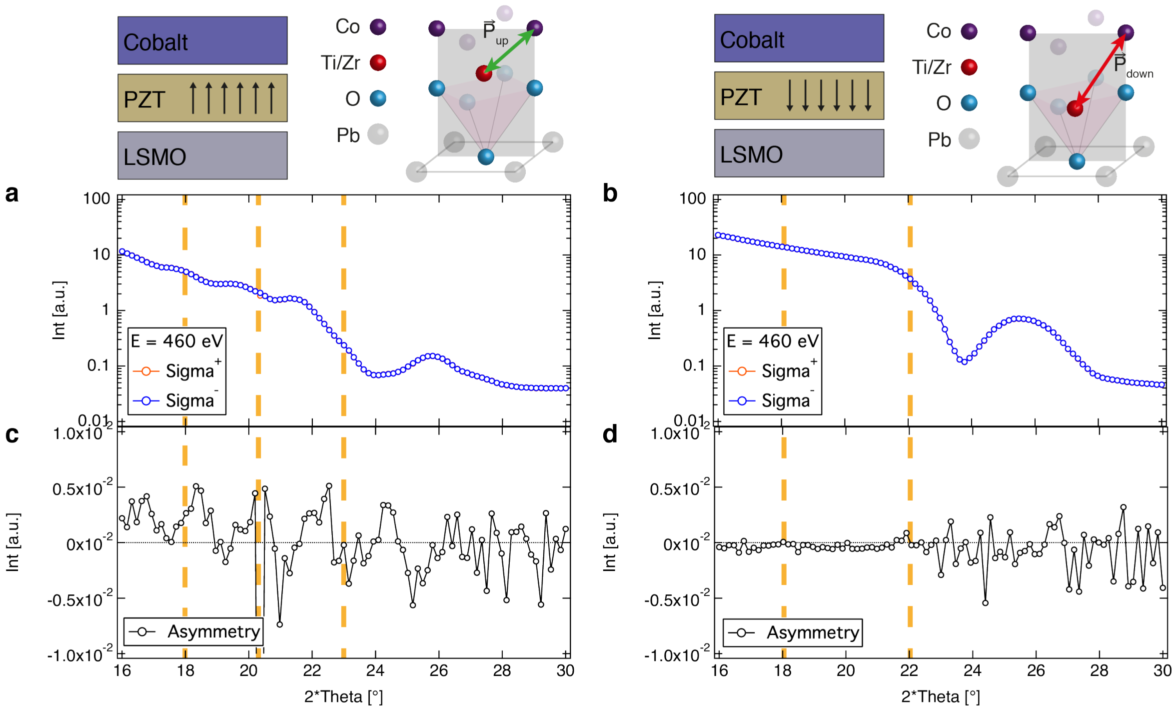

Figure 7.7: Reflectivity measurements for different ferroelectric polarizations. **a** and **b**, Reflectivity curves for the polarized samples with P_{up} (**a**) and P_{down} (**b**), respectively. The yellow, dashed lines emphasize the three angles ($2\Theta = 18\,^\circ$, $2\Theta = 20.35\,^\circ$ and $2\Theta = 23\,^\circ$) that are chosen for the P_{up}-sample to measure element specific hysteresis loops and two angles ($2\Theta = 18\,^\circ$ and $2\Theta = 22\,^\circ$) for the P_{down}-sample. **c** and **d**, Calculated asymmetry from the data in **a** and **b**, showing the magnetic information in dependence of the reflection angle.

7.8 c and **d** for example, which resembles the sign of the asymmetry in **Fig. 7.7** at the corresponding reflectivity angles. The strength of the XRMS signals, however, increases with titanium being physically closer towards the cobalt electrode, which is the case for the P_{up} polarized sample. In fact, the necessary averaging (amount of magnetic field sweep repetitions) of the measurements vary dramatically for the two opposite FE polarized areas, being as high as 120 times for polarization pointing down (P_{down}) and as low as 3 times for polarization pointing up (P_{up}). The coercive fields are, as expected, with $\approx \pm 5\,$mT the same for titanium and cobalt and do not seem to be affected by the ferreoelectric polarization direction.

For better comparison, **Fig. 7.9** summarizes the reflectivity measurements at the titanium $E \approx 460\,$eV edge for all measured polarization cases. Remarkably, there is a strong contrast in the presented reflectivity curves already visible between the three polarization cases (**Fig. 7.9 a**). The curve measured on the as-grown (and therefore never electrically "approached") area of the sample shows much more and stronger oscillatory features than the polarized ones, which are much more comparable. The asymmetry of the reflectivity, however, strongly possesses a clear trend. The unpolarized sample obviously shows the strongest magnetic properties, followed by the area that is polarized towards cobalt (P_{up}) and is obviously phase shifted. The oppositely polarized sample, however, (P_{down}) lags clearly visible magnetic properties

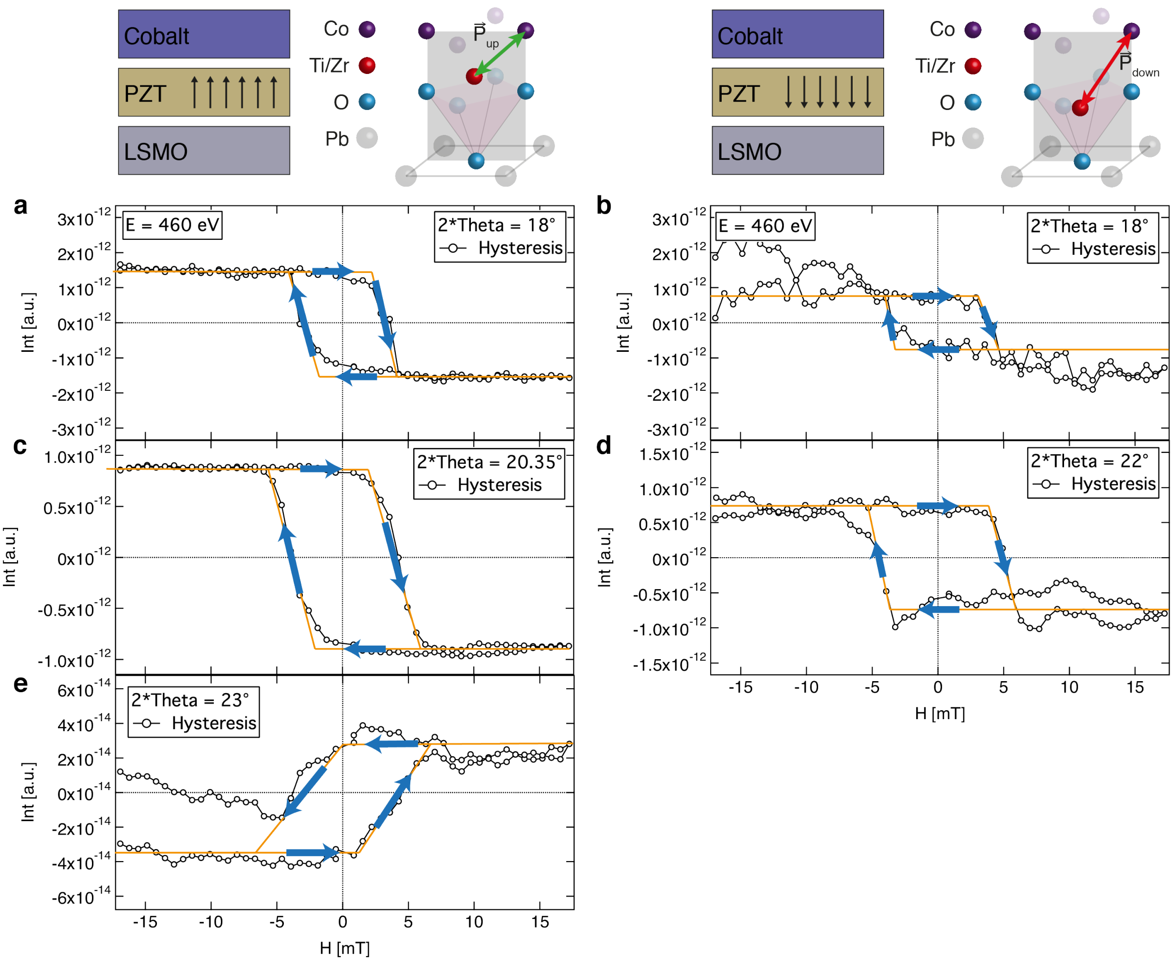

Figure 7.8: Element specific hysteresis loops measured for different ferroelectric polarizations. a and **b**, Magnetic hysteresis curves for a reflection angle of $2\Theta = 18\,^\circ$ for ferroelectric polarizations P_{up} and P_{down}, respectively. Magnetic hysteresis loops for P_{up} at $2\Theta = 20.35\,^\circ$ (**c**) and $2\Theta = 23\,^\circ$ (**e**) and for P_{down} at $2\Theta = 22\,^\circ$ (**d**). The blue arrows inside the loops should point out the hysteresis loop trace direction as it was measured during the magnetic field sweeps. Schemes on top of the figure put the resulting measurements into perspective to the corresponding FE polarization direction of the PZT tunnel barrier.

in comparison to the other samples.

At this point, not much more information can be extracted from these data. A profile of the interface based on present data could potentially only be obtained after a fitting procedure with the Zak-formalism [203].

7.2.2 Interface engineering, using a PZO monolayer

Like it has been demonstrated in Section 5.4 on page 67, increasing the distance between titanium and the cobalt electrode *via* the introduction of a PZO layer in between cobalt and PTO has strong effects on the TER and TMR properties of similar junctions. Therefore, the next step is to investigate the magnetic response element-selectively on Co/PTO/LSMO and Co/PZO/PTO/LSMO samples with FE barrier thicknesses

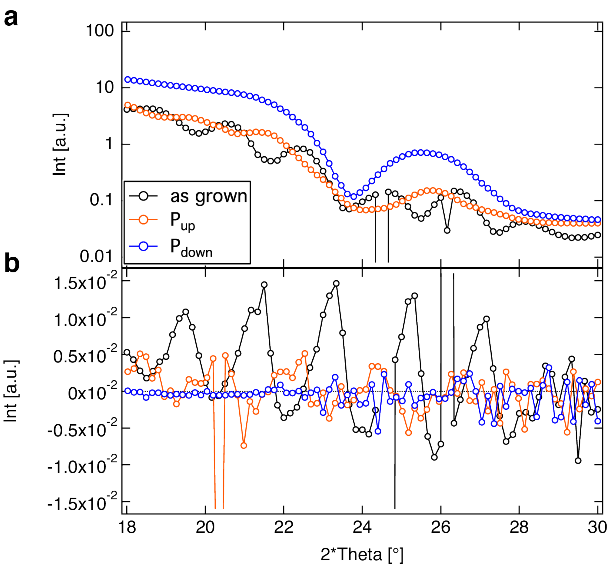

Figure 7.9: Comparison of reflectivity curves measured for different ferroelectric polarization directions. a Reflectivity signal versus 2Θ angle for all three polarization cases: Unpolarized/as grown (black), polarization towards cobalt (orange) and polarization towards LSMO (blue). **b**, Asymmetry of the measurement data in (**a**) with the same legend.

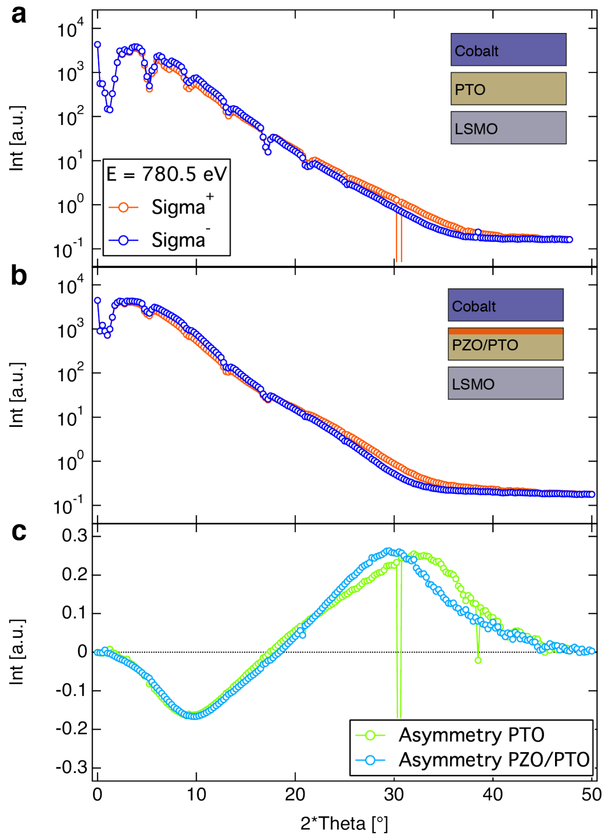

Figure 7.10: Reflectivity curves of cobalt measured for both samples. a and **b**, Reflectivity signal measured at the cobalt $L_{3,2}$ edge ($\approx 780\,\text{eV}$) versus 2Θ angle for the two investigated samples Co/PTO/LSMO and Co/PZO/PTO/LSMO, respectively. **c**, Asymmetry of the data, comparing both discussed samples.

in the tunneling regime[1]. The two grown samples (see **Fig. 7.1 b**) were therefore completely covered by the films without any patterning, resulting in $5 \cdot 5\,\text{mm}^2$ large areas for the investigation. This enabled to use a larger beam size and thus larger overall intensity for the reflected signal, leading to higher reflectivity angles that were able to be resolved and stronger signals at the titanium edge.

The reflectivity curves of the cobalt demonstrate again, similar to the PZT sample

---

[1] This did not allow us to switch between ferroelectric polarization states though.

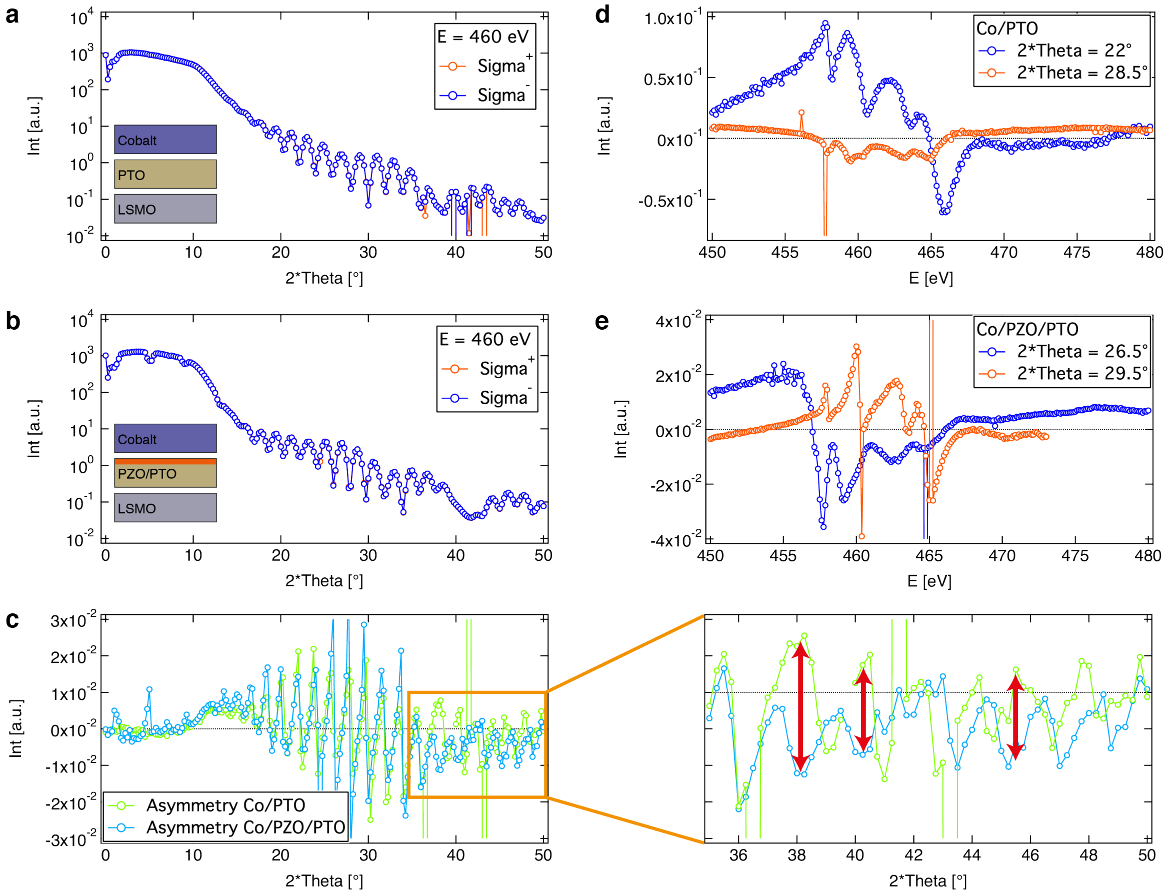

Figure 7.11: Reflectivity curves of titanium measured for both samples. a and **b**, Reflectivity signal measured at the titanium E edge ($\approx$ 460 eV) versus 2Θ angle for the two investigated samples Co/PTO/LSMO and Co/PZO/PTO/LSMO, respectively. **c**, Asymmetry of the data, comparing the measurements in **a** and **b**. **d** and **e**, XMCD spectra for the Co/PTO/LSMO and Co/PZO/PTO/LSMO samples, respectively.

from before, comparable features in terms of signal strength and shape of the curves. In **Fig. 7.10**, the asymmetries of the reflectivity curves for the Co/PTO/LSMO and the Co/PZO/PTO/LSMO samples are, as anticipated, very much alike, possessing a sign change of the asymmetry at around $2\Theta = 18°$, but with a slight shift of the positive maxima in relation to each other.

At the titanium edge $E \approx 460$ eV, the reflectivity measurements and XMCD spectra are summarized for both samples in **Fig. 7.11**. As indicated in the figure, the upper two lines represent the plots for the Co/PTO/LSMO and Co/PZO/PTO/LSMO samples, respectively. For two different angles at each sample, where the asymmetry of the curves has opposite sign, XMCD spectra were measured (see **Fig. 7.11 d** and **e**). Obviously, the spectra show strong dependence on the set reflectivity angle, which makes a comparison obsolete. The asymmetry of the reflectivity signals is preseneted in **Fig. 7.11 c** and possesses a clear visible coherence of the oscillatory signal strength up to an angle of $2\Theta \approx 37°$. For higher angles, a dephasing is present, which is marked by the red arrows in the magnified part on the right side of **Fig. 7.11 c**. This phase shift is an indicator for a structural change of the interface, triggering also the change

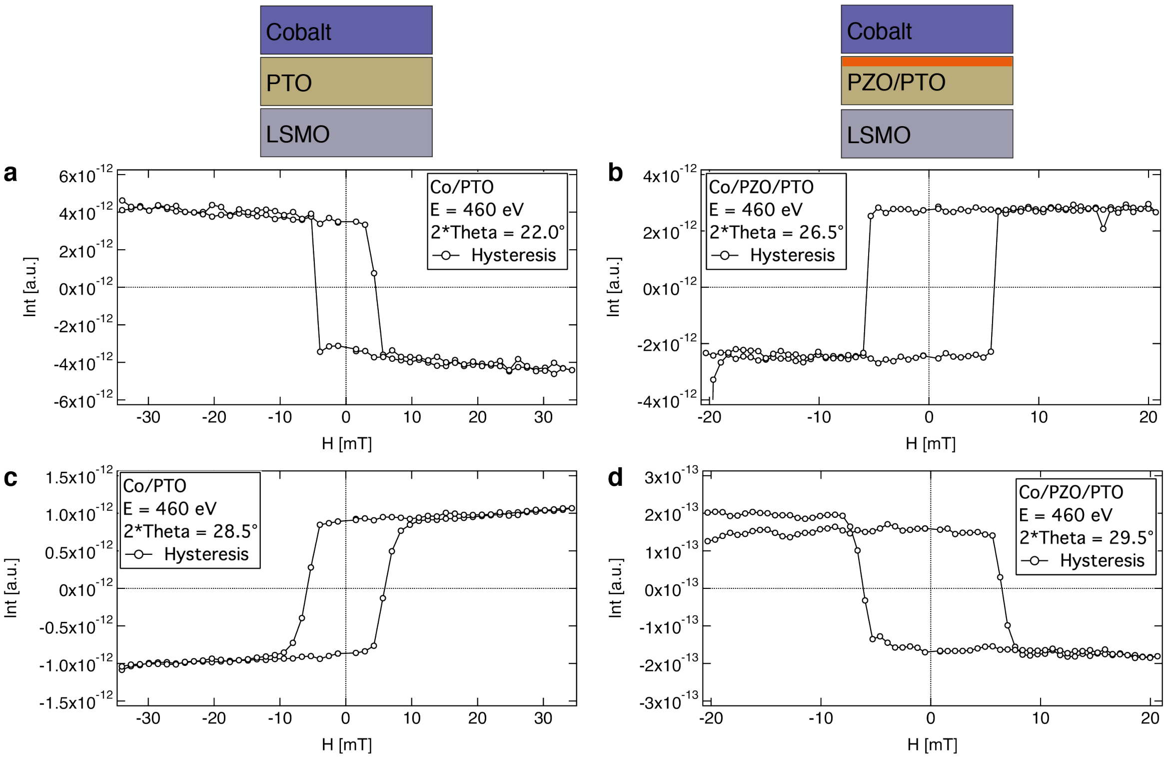

Figure 7.12: Hysteresis curves of titanium for Co/PTO and Co/PZO/PTO interfaces. **a** and **c**, Measured hysteresis curves at $E \approx 460\,\mathrm{eV}$ for the two reflectivity angles $2\Theta \approx 22\,°$ (**a**) and $2\Theta \approx 28.5\,°$ (**c**) for the Co/PTO/LSMO sample. **b** and **d**, Titanium hysteresis curves for the two reflectivity angles $2\Theta \approx 26.5\,°$ (**b**) and $2\Theta \approx 29.5\,°$ (**d**) for the Co/PZO/PTO/LSMO sample.

in the magnetic properties of that interface.

The comparison of magnetic hysteresis curves for titanium in **Fig. 7.12** does not give enough information for quantitative analysis. It can be stated, that titanium behaves ferromagnetically in both cases (Co/PTO/LSMO and Co/PZO/PTO/LSMO) and owns very similar characteristics for both samples in terms of coercive fields of around 6 mT and measured XRMS intensity. The sign-changes of the magnetic hysteresis curves is solely caused by the chosen angles, where the sign of the asymmetry is opposite.

7.3 Summary of the chapter

We were able to confirm that cobalt induces a magnetic moment onto the interfacial titanium at the FE interface. The displacement of titanium by ferroelectric polarization or a buffer layer of PZO shows significant changes in the phases and magnitudes of the measured $\Theta - 2\Theta$ XRMS signals. The fact that an induced magnetic moment at the Ti-edge still exists in the Co/PZO/PTO sample could be a result of the relatively high temperature, 300 K, which probably leads to metallization of titanium inside its surrounding oxygen octahedra within PTO in at least the first several monolayers (see Section 5.1 on page 50). If the chemical potential of titanium does not lie in the band-gap, the existing free electronic states always enable the possibility of magnetism, especially in proximity to magnetic materials due to exchange mechanisms. Thus it is not surprising that the induced magnetic moment of titanium does not vanish in case of the PZO-terminated sample.

The polarization dependence of the magnetic measurements clearly demonstrates magnetoelectric coupling, which leads to different magnitudes of hysteresis signals as well as a slight modification of the magnetic anisotropy. This is very interesting in the context of the effects already discussed in Section 5.6.2 (page 72).

To underline the interface sensitivity towards the Co/FE interface, it was not possible to measure the XMCD spectra of manganese (not shown in this thesis) in case of the Co/PZT/LSMO (thick FE film) sample. The observed changes of the magnetic characteristics of titanium upon ferroelectric polarization reversal should therefore only be contributed to the Co/FE interface.

8

Summary and outlook

This final chapter summarizes all discussions around the performed experiments and will give a comprehensive overview of the conclusions that were drawn. In the Outlook section, possible future experiments that could lead to a significant contribution to the understanding of important interfacial magnetoelectric coupling mechanisms will be presented.

8.1 Summary

In the present thesis, multiferroic tunnel junctions (MFTJs) with new and established material compositions and with a focus on interface-induced effects were investigated. High-quality film growth has been achieved, with the possibility of controlling the thickness of the grown films *in situ via* RHEED. This allowed the design and reproduction of tunnel structures that showed very similar behavior of what had been achieved with different equipment, exhibiting the robustness of the recently found reversible switching of spin polarization [24].

The TER was enhanced by several magnitudes (up to 150000 %) with the introduction of an antiferroelectric PZO monolayer and was demonstrated (in case of a Co/PZT/LSMO junction) not only to possess a digital, but an analogous tunnel electroresistance, which allowed the programming of a virtually infinite number of resistance states. This so called ferroelectric tunnel memristor was investigated at room temperature and exhibited analytical behavior that could be described by a simple characteristic transfer function, which was derived from a parallel resistance model and the Kolmogorov-Avrami-Ishibashi description for ferroelectric domain wall kinetics.

The measured transport data from the fabricated $\mathrm{PbZr}_x\mathrm{Ti}_{1-x}\mathrm{O}_3$-based (with $x = 0$, 0.2 and 1) tunnel junctions suggested that the underlying principle for the TER is dictated by an effective tunnel barrier thickness variation rather than a pure depolarization field asymmetry upon ferroelectric polarization reversal. This conclusion was drawn from analysis using the Brinkman model.

Other origins of the sign and magnitude of the measured TER in all studied junctions (Co/PZT/LSMO, Co/PTO/LSMO and Co/PZO/PTO/LSMO) have been discussed but could be excluded. The inverse piezoelectric effect based on the piezoelectric constant d_{33} of PZT, for example, has been demonstrated to not significantly contribute to the measured TER (around 2 %), which was shown by separating this effect with a simple simulation.

Mathematical modeling methods using the Brinkman model enabled accurate fitting of the data while preserving freedom for the corresponding parameters within reasonable boundary conditions. For either of the two junctions involving PZT and PTO, the mentioned effective barrier thickness variation is the main contribution to the TER. This was independently discovered by theorists[1], who calculated the resonant tunnel conductance on very similar (in case of Co/PTO/LSMO, identical) heterostructures.

The controlled variation of the chemical composition of the upper interface of the ferroelectric barrier resulted in corresponding modifications of the TER and TMR, thus qualitatively demonstrating the responsibility of the upper interface for the observed effects. Furthermore, it allowed the observation of novel ferroic properties in MFTJs such as the exchange-biased TMR without the deliberate introduction of an antiferromagnetic layer. The study of this exchange biased system by chemical variation of the interface termination towards the cobalt electrode indicates that titanium in proximity to cobalt plays the crucial role in obtaining a unidirectional anisotropy. The exploitation of the found exchange-biased TMR (8 % in remanence) in combination with TER (300 %) allowed the creation of a four-state memory device that showed robust resistive switching, accessible with magnetic and electric fields.

Investigations with synchrotron radiation showed the existence of a magnetic moment in titanium induced by an adjacent cobalt film, which revealed a dependence on ferroelectric polarization direction and thus strongly suggests that the observed switching of the spin polarization of the tunneling electrons by polarization switching in a Co/PZT/LSMO junction should stem from the (antiferromagnetic) coupling between the interfacial titanium and cobalt.

8.2 Outlook

During this work, several interesting and unexpected characteristics have been revealed to stem from interface properties of the investigated tunnel junctions. It is thus desirable to more deeply investigate the role of the interfaces in multiferroic tunnel junctions. For example, neutron facilities of the new generation would allow the focussing of neutrons to a much smaller area than before, to increase the accuracy, and ultimately enable the quantifiable study of magnetic momentum at interfaces of small capacitors with nanometer-resolution.

Additional preliminary synchrotron results obtained at BESSYII (conducted very recently) demonstrate that the induced magnetic moment of titanium at the cobalt interface is, indeed, exchange biased. Upon field cooling the magnetic hysteresis curves of titanium evidently showed exchange bias. This could be a starting point for even more detailed investigations of the magnetic structure at the interface, especially with focus on *in situ* ferroelectric switching. Obviously, more emphasis has to be put on new sample designs and structuring that would allow the desired *in situ* switching capabilities, maybe even with ferroelectric films in the tunneling thickness range.

A possible approach would be to use top-down lithographic patterning with better selective structuring methods like time of flight spectrometric supported ion-milling.

---

[1] Working group of Professor I. Mertig.

With this technique, it should be possible to create devices with ferroelectric barriers in the tunnel-current thickness range with higher yield than with wet etching processes. By selectively choosing and contacting pre-characterized junctions of small capacitor area, a macroscopic and thus better accessible area could possibly be investigated as a function of ferroelectric switching with synchrotron or neutron measurements.

Considering the TER effect, an influence on its magnitude by strain tuning should be observable. This could be achieved by using different substrate materials with varying lattice misfit such as $DyScO_3$ with an in-plane lattice constant of 3.952 Å.

Based on the discussion of the huge TER measured on Co/PZO/PTO/LSMO junctions, further optimization and enlargement of this effect could be deliberately conducted. It seems as if the biggest contribution originates from the (ferroelectrically switchable) effective electron mass, indicating a reversible change of the charge carrier type between electron and hole. Interface engineered samples using other (heavier) elements such as hafnium as a replacement for zirconium (the antiferroelectric lead hafnate $PbHfO_3$) might give more insights into interesting interface induced phenomena and will eventually lead to a more complete picture of the mechanisms behind tunnel electro resistance effects.

References

[1] DiVincenzo, D. P. *Quantum Computation. Science*, **270**(5234):255–261 (1995).

[2] Shor, P. W. *Polynomial-Time Algorithms for Prime Factorization and Discrete Logarithms on a Quantum Computer. SIAM Journal on Computing*, **26**(5):1484–1509 (1997).

[3] Backus, J. *Can programming be liberated from the von Neumann style?: A functional style and its algebra of programs. Communications of the ACM*, **21**(8):613–641 (1978).

[4] Di Ventra, M. and Pershin, Y. V. *The parallel approach. Nature Physics*, **9**(4):200–202 (2013).

[5] Owens, J. D.; Luebke, D.; Govindaraju, N.; Harris, M.; Krüger, J.; Lefohn, A. E.; and Purcell, T. J. *A Survey of General-Purpose Computation on Graphics Hardware. Computer Graphics Forum*, **26**(1):80–113 (2007).

[6] Jo, S. H.; Chang, T.; Ebong, I.; Bhadviya, B. B.; Mazumder, P.; and Lu, W. *Nanoscale memristor device as synapse in neuromorphic systems. Nano letters*, **10**(4):1297–1301 (2010).

[7] Strukov, D. B. *Smart connections. Nature Nanotechnology*, **476**(8):403–405 (2011).

[8] Alibart, F.; Zamanidoost, E.; and Strukov, D. B. *Pattern classification by memristive crossbar circuits using ex situ and in situ training. Nature Communications*, **4**(3071):1–7 (2013).

[9] Yang, J. J.; Strukov, D. B.; and Stewart, D. R. *Memristive devices for computing. Nature Nanotechnology*, **8**(1):13–24 (2013).

[10] Tsymbal, E. Y. and Kohlstedt, H. *Tunneling across a ferroelectric. Science*, **313**(5784):181–3 (2006).

[11] Bibes, M. *Towards a magnetoelectric memory. Nature*, **7**(June):425–426 (2008).

[12] Kohlstedt, H.; Pertsev, N.; Rodríguez Contreras, J.; and Waser, R. *Theoretical current-voltage characteristics of ferroelectric tunnel junctions. Physical Review B*, **72**(12):125314 (2005).

[13] Zhuravlev, M.; Sabirianov, R.; Jaswal, S.; and Tsymbal, E. *Giant Electroresistance in Ferroelectric Tunnel Junctions. Physical Review Letters*, **94**(24):1–4 (2005).

[14] Garcia, V.; Fusil, S.; Bouzehouane, K.; Enouz-Vedrenne, S.; Mathur, N. D.; Barthélémy, A.; and Bibes, M. *Giant tunnel electroresistance for non-destructive readout of ferroelectric states. Nature*, **460**(7):81–84 (2009).

[15] Gruverman, A.; Wu, D.; Lu, H.; Wang, Y.; Jang, H. W.; Folkman, C. M.; Zhuravlev, M. Y.; Felker, D.; Rzchowski, M.; Eom, C.-B.; and Tsymbal, E. Y. *Tunneling electroresistance effect in ferroelectric tunnel junctions at the nanoscale. Nano Letters*, **9**(10):3539–3543 (2009).

[16] Pantel, D.; Goetze, S.; Hesse, D.; and Alexe, M. *Room-Temperature Ferroelectric Resistive Switching in Ultrathin Pb($Zr_{0.2}Ti_{0.8}$)O_3 Films. ACS Nano*, **5**(7):6032–6038 (2011).

[17] Pantel, D.; Lu, H.; Goetze, S.; Werner, P.; Jik Kim, D.; Gruverman, A.; Hesse, D.; and Alexe, M. *Tunnel electroresistance in junctions with ultrathin ferroelectric Pb($Zr_{0.2}Ti_{0.8}$)O_3 barriers. Applied Physics Letters*, **100**(23):232902 (2012).

[18] Chanthbouala, A.; Garcia, V.; Cherifi, R. O.; Bouzehouane, K.; Fusil, S.; Moya, X.; Xavier, S.; Yamada, H.; Deranlot, C.; Mathur, N. D.; Bibes, M.; Barthélémy, A.; and Grollier, J. *A ferroelectric memristor. Nature Materials*, **11**(9):860–864 (2012).

[19] Kim, D. J.; Lu, H.; Ryu, S.; Bark, C.-W.; Eom, C.-B.; Tsymbal, E. Y.; and Gruverman, A. *Ferroelectric tunnel memristor. Nano Letters*, **12**(11):5697–5702 (2012).

[20] Scott, J. *Multiferroic memories. Nature Materials*, **6**(4):256–257 (2007).

[21] Hambe, M.; Petraru, A.; Pertsev, N. A.; Munroe, P.; Nagarajan, V.; and Kohlstedt, H. *Crossing an Interface: Ferroelectric Control of Tunnel Currents in Magnetic Complex Oxide Heterostructures. Advanced Functional Materials*, **20**(15):2436–2441 (2010).

[22] Garcia, V.; Bibes, M.; Bocher, L.; Valencia, S.; Kronast, F.; Crassous, A.; Moya, X.; Enouz-Vedrenne, S.; Gloter, A.; Imhoff, D.; Deranlot, C.; Mathur, N. D.; Fusil, S.; Bouzehouane, K.; and Barthélémy, A. *Ferroelectric control of spin polarization. Science*, **327**(5969):1106–1110 (2010).

[23] Rivera, J.-P. *On definitions, units, measurements, tensor forms of the linear magnetoelectric effect and on a new dynamic method applied to Cr-Cl boracite. Ferroelectrics*, **161**(1):165–180 (1994).

[24] Pantel, D.; Goetze, S.; Hesse, D.; and Alexe, M. *Reversible electrical switching of spin polarization in multiferroic tunnel junctions. Nature materials*, **11**(4):289–293 (2012).

[25] Pintilie, L.; Lisca, M.; and Alexe, M. *Epitaxial-quality PZT : insulator or semiconductor? Journal of Optoelectronics and Advanced Materials*, **8**(1):7–12 (2006).

[26] Pintilie, L.; Vrejoiu, I.; Hesse, D.; LeRhun, G.; and Alexe, M. *Ferroelectric polarization-leakage current relation in high quality epitaxial Pb(Zr,Ti)O_3 films. Physical Review B*, **75**(10):1–14 (2007).

[27] Boyn, S.; Girod, S.; Garcia, V.; Fusil, S.; Xavier, S.; Deranlot, C.; Yamada, H.; Carrétéro, C.; Jacquet, E.; Bibes, M.; Barthélémy, A.; and Grollier, J. *High-performance ferroelectric memory based on fully patterned tunnel junctions. Applied Physics Letters*, **104**(5):052909 (2014).

[28] Chua, L. *Memristor-The Missing Circuit Element. IEEE*, **5**:507–519 (1971).

[29] Strukov, D. B.; Snider, G. S.; Stewart, D. R.; and Williams, R. S. *The missing memristor found. Nature*, **453**(5):80–83 (2008).

[30] Pickett, M. D.; Medeiros-Ribeiro, G.; and Williams, R. S. *A scalable neuristor built with Mott memristors. Nature Materials*, **11**(3510):1–4 (2012).

[31] Aizu, K. *Possible Species of Ferromagnetic, Ferroelectric, and Ferroelastic Crystals. Physical Review B*, **2**(3):754–772 (1970).

[32] Lu, H.; Bark, C.-W.; Esque de los Ojos, D.; Alcala, J.; Eom, C. B.; Catalan, G.; and Gruverman, A. *Mechanical writing of ferroelectric polarization. Science*, **336**(6077):59–61 (2012).

[33] Shirane, F. J. G. *Ferroelectric crystals*. Dover Publications, New York (1993).

[34] Meiklejohn, W. H. and Bean, C. P. *New magnetic anisotropy. Physical Review*, **102**(5):1413–1414 (1956).

[35] Koster, G.; Kropman, B. L.; Rijnders, G. J. H. M.; Blank, D. H. A.; and Rogalla, H. *Quasi-ideal strontium titanate crystal surfaces through formation of strontium hydroxide. Applied Physics Letters*, **73**(20):2920–2922 (1998).

[36] Zubko, P.; Catalan, G.; Buckley, A.; Welche, P.; and Scott, J. *Strain-Gradient-Induced Polarization in SrTiO_3 Single Crystals. Physical Review Letters*, **99**(16):167601 (2007).

[37] Tomio, T.; Miki, H.; Tabata, H.; Kawai, T.; and Kawai, S. *Control of electrical conductivity in laser deposited SrTiO_3 thin films with Nb doping. Journal of Applied Physics*, **76**(10):5886 (1994).

[38] Jang, H. W.; Kumar, A.; Denev, S.; Biegalski, M. D.; Maksymovych, P.; Bark, C. W.; Nelson, C. T.; Folkman, C. M.; Baek, S. H.; Balke, N.; Brooks, C. M.; Tenne, D. A.; Schlom, D. G.; Chen, L. Q.; Pan, X. Q.; Kalinin, S. V.; Gopalan, V.; and Eom, C. B. *Ferroelectricity in Strain-Free SrTiO_3 Thin Films. Physical Review Letters*, **104**(19):197601 (2010).

[39] Pickett, W. E. and Singh, D. J. *Chemical disorder and charge transport in ferromagnetic manganites. Physical Review B*, **55**(14):8642–8645 (1997).

[40] Park, J.-H.; Vescovo, E.; Kim, H.-J.; Kwon, C.; Ramesh, R.; and Venkatesan, T. *Direct evidence for a half-metallic ferromagnet. Nature*, **392**(4):794–796 (1998).

[41] Bowen, M.; Bibes, M.; Barthelemy, A.; Contour, J.-P.; Anane, A.; Lematre, Y.; and Fert, A. *Nearly total spin polarization in* $La_{2/3}Sr_{1/3}MnO_3$ *from tunneling experiments. Applied Physics Letters*, **82**(2):233–235 (2003).

[42] Zener, C. *Interaction between the d-Shells in the Transition Metals. II. Ferromagnetic Compounts of Manganese with Perovskite Structure. Physical Review*, **82**:403–405 (1951).

[43] Watanabe, H. *Magnetic Properties of Perovskites Containing Strontium, II. Lanthan-Strontium Manganites. Journal of the physical society of Japan*, **16**(3):433–439 (1961).

[44] Boschker, H.; Huijben, M.; Vailionis, A.; Verbeeck, J.; van Aert, S.; Luysberg, M.; Bals, S.; van Tendeloo, G.; Houwman, E. P.; Koster, G.; Blank, D. H. A.; and Rijnders, G. *Optimized fabrication of high-quality* $La_{0.67}Sr_{0.33}MnO_3$ *thin films considering all essential characteristics. Journal of Physics D: Applied Physics*, **44**(20):205001 (2011).

[45] Holleman, A. F. and Wiberg, N. *Lehrbuch der Anorganischen Chemie.* de Gruyter, Berlin (2007).

[46] Schubert, K. *Ein Modell für die Kristallstrukturen der chemischen Elemente. Acta Crystallographica Section B*, **30**(1):193–204 (1974).

[47] Vrejoiu, I.; Le Rhun, G.; Pintilie, L.; Hesse, D.; Alexe, M.; and Gösele, U. *Intrinsic Ferroelectric Properties of Strained Tetragonal* $PbZr_{0.2}Ti_{0.8}O_3$ *Obtained on Layer-by-Layer Grown, Defect-Free Single-Crystalline Films. Advanced Materials*, **18**(13):1657–1661 (2006).

[48] Hamedi, L.; Guilloux-Viry, M.; Perrin, A.; and Cherkani, M. H. *On the epitaxial growth of PZT films by pulsed laser deposition. Ann. Chim. Sci. Mat*, **23**(33):377–380 (1998).

[49] Lisca, M.; Pintilie, L.; Alexe, M.; and Teodorescu, C. *Thickness effect in* $Pb(Zr_{0.2}Ti_{0.8})O_3$ *ferroelectric thin films grown by pulsed laser deposition. Applied Surface Science*, **252**(13):4549–4552 (2006).

[50] Lee, H.; Nakhmanson, S.; Chisholm, M.; Christen, H.; Rabe, K.; and Vanderbilt, D. *Suppressed Dependence of Polarization on Epitaxial Strain in Highly Polar Ferroelectrics. Physical Review Letters*, **98**(21):217602 (2007).

[51] Fushimi, S. and Ikeda, T. *Phase Equilibrium in the System* PbO-TiO_2-ZrO_2. *Joournal of The American Ceramic Society*, **50**(3):129–132 (1966).

[52] Aggarwal, S. and Ramesh, R. *Point Defect Chemistry of Metal Oxide Heterostructures. Annual Review of Materials Science*, **28**(1):463–499 (1998).

[53] Frantti, F.; Lappalainen, J.; Eriksson, S.; Lantto, V.; Nishio, S.; Kakihana, M.; Ivanov, S.; and Rundlöf, H. *Neutron Diffraction Studies of* $Pb(Zr_xTi_{1-x})O_3$ *Ceramics. Japanese Journal of Applied Physics*, **39**:5697–5703 (2000).

[54] Li, W. and Alexe, M. *Investigation on switching kinetics in epitaxial* $PbZr_{0.2}Ti_{0.8}O_3$ *ferroelectric thin films : Role of the 90° domain walls. Applied Physics Letters*, **91**:262903 (2007).

[55] Cohen, R. E. *Origin of ferroelectricity in perovskite oxides. Nature*, **358**(6382):136–138 (1992).

[56] Pintilie, L. and Alexe, M. *Metal-ferroelectric-metal heterostructures with Schottky contacts. I. Influence of the ferroelectric properties. Journal of Applied Physics*, **98**(12):124103 (2005).

[57] Ghosez, P. and Rabe, K. M. *Microscopic model of ferroelectricity in stress-free* $PbTiO_3$ *ultrathin films. Applied Physics Letters*, **76**(19):2767 (2000).

[58] Akimov, A.; Savchuk, G.; Rubtsov, V.; and Letko, A. *Golden Book of Phase Transitions.* Wroclaw (2002).

[59] Cooper, V. R. and Rabe, K. M. *Enhancing piezoelectricity through polarization-strain coupling in ferroelectric superlattices. Physical Review B*, **79**(180101):5–8 (2009).

[60] Sawaguchi, E.; Shirane, G.; and Takagi, Y. *Phase Transition in Lead Zirconate. Journal of the Physics Society Japan*, **6**(5):333–339 (1951).

[61] Shirane, G.; Sawaguchi, E.; and Takagi, Y. *Dielectric Properties of Lead Zirconate. Physical Review*, **84**(3):476–481 (1951).

[62] Boldyreva, K.; Pintilie, L.; Lotnyk, A.; Misirlioglu, I. B.; Alexe, M.; and Hesse, D. *Thickness-driven antiferroelectric-to-ferroelectric phase transition of thin* $PbZrO_3$ *layers in epitaxial* $PbZrO_3Pb(Zr_{0.8}Ti_{0.2})O_3$ *multilayers. Applied Physics Letters*, **91**(12):122915 (2007).

[63] Jona, F.; Shirane, G.; Mazzi, F.; and Pepinsky, R. *X-Ray and Neutron Diffraction Study of Antiferroelectric Lead Zirconate,* $PbZrO_3$. *Phys. Rev.*, **105**(3):849–856 (1957).

[64] Boldyreva, K.; Pintilie, L.; Lotnyk, A.; Misirlioglu, I. B.; Alexe, M.; and Hesse, D. *Ferroelectric/Antiferroelectric* $Pb(Zr_{0.8}Ti_{0.2})O_3/PbZrO_3$ *Epitaxial Multilayers: Growth and Thickness-Dependent Properties. Ferroelectrics*, **370**(1):140–146 (2008).

[65] Pantel, D. and Alexe, M. *Electroresistance effects in ferroelectric tunnel barriers. Physical Review B*, **82**(13):1–8 (2010).

[66] Sze, S. M. and Ng, K. K. *Physics of Semiconductor Devices.* Wiley (2007).

[67] Frenkel, J. *The Electrical Resistance of Contacts Between Solid Conductors. Physical Review*, **36**:1604–1618 (1930).

[68] Waser, R.; Dittmann, R.; Staikov, G.; and Szot, K. *Redox-Based Resistive Switching Memories - Nanoionic Mechanisms, Prospects, and Challenges. Advanced Materials*, **21**(25-26):2632–2663 (2009).

[69] Waser, R. and Aono, M. *Nanoionics-based resistive switching memories. Nature materials*, **6**(11):833–40 (2007).

[70] Valov, I.; Linn, E.; Tappertzhofen, S.; Schmelzer, S.; Lentz, F.; and Waser, R. *Nanobatteries in redox-based resistive switches require extension of memristor theory. Nature communications*, **4**(1771):1–9 (2013).

[71] Garca, N. *Conducting ballistic magnetoresistance and tunneling magnetoresistance: Pinholes and tunnel barriers. Applied Physics Letters*, **77**(9):1351 (2000).

[72] Brinkman, W. F. *Tunneling Conductance of Asymmetrical Barriers. Journal of Applied Physics*, **41**(5):1915–1921 (1970).

[73] Wen, Z.; You, L.; Wang, J.; Li, A.; and Wu, D. *Temperature-dependent tunneling electroresistance in Pt/BaTiO$_3$/SrRuO$_3$ ferroelectric tunnel junctions. Applied Physics Letters*, **103**(13):132913 (2013).

[74] Ventura, J.; Teixeira, J.; Araujo, J.; Sousa, J.; Wisniowski, P.; and Freitas, P. *Pinholes and temperature-dependent transport properties of MgO magnetic tunnel junctions. Physical Review B*, **78**(2):024403 (2008).

[75] Hund, F. *Zur Deutung der Molekülspektren. III. Zeitschrift für Physik*, **43**(11-12):805–826 (1927).

[76] Gurney, R. and Condon, E. *Wave Mechanics and Radioactive Desintegration. Nature*, **122**(439) (1928).

[77] Glazman, L. I. and Matveev, K. A. *Inelastic tunneling across thin amorphous films. Sov. Phys. JETP*, **67**(6):1276–1282 (1988).

[78] Glazman, L. and R., S. *Inelastic resonant tunneling of electrons through a potential barrier. Journal of Experimental and Theoretical Physics*, **67**(1):163–170 (1988).

[79] Lu, Y.; Tran, M.; Jaffrès, H.; Seneor, P.; Deranlot, C.; Petroff, F.; George, J.-M.; Lépine, B.; Ababou, S.; and Jézéquel, G. *Spin-Polarized Inelastic Tunneling through Insulating Barriers. Physical Review Letters*, **102**(17):176801 (2009).

[80] Oliver, B. *Temperature and bias dependence of dynamic conductance low resistive magnetic tunnel junctions. Journal of Applied Physics*, **95**(2):546 (2004).

[81] Moran, O.; Hott, R.; Schneider, R.; Whl, H.; and J., H. *Inelastic resonant tunneling of electrons through a potential barrier. Journal of Applied Physics*, **94**(19):6667 (2003).

[82] Lu, Y. *Mangetotransport properties of manganite based magnetic tunnel junctions. Journal of Applied Physics*, **102**(12):0–7 (2007).

[83] Slaughter, J. *Materials for Magnetoresistive Random Access Memory. Annual Review of Materials Research*, **39**(1):277–296 (2009).

[84] Fisher, J. C. and Giaever, I. *Tunneling Through Thin Insulating Layers. Journal of Applied Physics*, **32**(2):172–177 (1961).

[85] Parkin, S. S. P.; Kaiser, C.; Panchula, A.; Rice, P. M.; Hughes, B.; Samant, M.; and Yang, S.-H. *Giant tunnelling magnetoresistance at room temperature with MgO (100) tunnel barriers. Nature materials*, **3**(12):862–7 (2004).

[86] Gajek, M.; Bibes, M.; Fusil, S.; Bouzehouane, K.; Fontcuberta, J.; Barthélémy, A.; and Fert, A. *Tunnel junctions with multiferroic barriers. Nature materials*, **6**(4):296–302 (2007).

[87] Mehta, R. R. *Depolarization fields in thin ferroelectric films. Journal of Applied Physics*, **44**(8):3379 (1973).

[88] Nagarajan, V.; Prasertchoung, S.; Zhao, T.; Zheng, H.; Ouyang, J.; Ramesh, R.; Tian, W.; Pan, X. Q.; Kim, D. M.; Eom, C. B.; Kohlstedt, H.; and Waser, R. *Size effects in ultrathin epitaxial ferroelectric heterostructures. Applied Physics Letters*, **84**(25):5225 (2004).

[89] Wen, Z.; Li, C.; Wu, D.; Li, A.; and Ming, N. *Ferroelectric-field-effect-enhanced electroresistance in metal / ferroelectric / semiconductor tunnel junctions. Nature Materials*, **12**(7):617–621 (2013).

[90] Tsymbal, E. Y. and Gruverman, A. *Beyond the barrier. Nature materials*, **12**(July):12–14 (2013).

[91] Lu, H.; Kim, D. J.; Bark, C.-W.; Ryu, S.; Eom, C. B.; Tsymbal, E. Y.; and Gruverman, A. *Mechanically-induced resistive switching in ferroelectric tunnel junctions. Nano letters*, **12**(12):6289–92 (2012).

[92] Mao, H. J.; Miao, P. X.; Cong, J. Z.; Song, C.; Cui, B.; Peng, J. J.; Li, F.; Wang, G. Y.; Zhao, Y. G.; Sun, Y.; Xiao, L. R.; and Pan, F. *Interface-modification-enhanced tunnel electroresistance in multiferroic tunnel junctions. Journal of Applied Physics*, **116**(5):053703 (2014).

[93] Julliere, M. *Tunneling Between Ferromagnetic Films. Physics Letters*, **54**(3):225–226 (1975).

[94] Moodera, J. S. and Mathon, G. *Spin polarized tunneling in ferromagnetic junctions. Journal of Magnetism and Magnetic Materials*, **200**(1-3):248–273 (1999).

[95] Meservey, R.; Tedrow, M.; and Fulde, P. *Magnetic Field Splitting of the Quasiparticle States in Superconducting Aluminum Films. Physical Review Letters*, **25**(18):1270–1272 (1970).

[96] Moodera, J.; Kinder, L.; Wong, T.; and R., M. *Large Magnetoresistance at Room Temperature in Ferromagnetic Thin Film Tunnel Junctions. Physical Review Letters*, **74**(16):3273–3276 (1995).

[97] Parkin, S. S. P.; Roche, K. P.; Samant, M. G.; Rice, P. M.; Beyers, R. B.; Scheuerlein, R. E.; OSullivan, E. J.; Brown, S. L.; Bucchigano, J.; Abraham, D. W.; Lu, Y.; Rooks, M.; Trouilloud, P. L.; Wanner, R. a.; and Gallagher, W. J. *Exchange-biased magnetic tunnel junctions and application to nonvolatile magnetic random access memory. Journal of Applied Physics*, **85**(8):5828 (1999).

[98] Viret, M.; Drouet, M.; Nassar, J.; Contour, J. P.; Fermon, C.; and Fert, A. *Low-field colossal magnetoresistance in manganite tunnel spin valves. Europhysics Letters*, **39**(5):545–549 (1997).

[99] McGuire, T. R. and Potter, R. I. *Anisotropic Magnetoresistance in Ferromagnetic 3d Alloys. IEEE Transactions on Magnetics*, **11**(4):1018–1038 (1975).

[100] Tsymbal, E. Y. and Pettifor, D. G. *Modelling of spin-polarized electron tunneling from 3d ferromagnets. Journal of Condensed Matter*, **9**:L411 (1997).

[101] Chua, L. and Kang, S. M. *Memristive Devices and Systems. Proceedings of the IEEE*, **64**(2):209–223 (1976).

[102] Joglekar, Y. N. and Wolf, S. J. *The elusive memristor: properties of basic electrical circuits. European Journal of Physics*, **30**(4):661–675 (2009).

[103] Yang, S. M.; Jo, J. Y.; Kim, T. H.; Yoon, J.-G.; Song, T. K.; Lee, H. N.; Marton, Z.; Park, S.; Jo, Y.; and Noh, T. W. *Ac Dynamics of Ferroelectric Domains From an Investigation of the Frequency Dependence of Hysteresis Loops. Physical Review B*, **82**(17):174125 (2010).

[104] Ishibashi, Y. and Takagi, Y. *Note on Ferroelectric Domain Switching. Journal of the Physical Society of Japan*, **31**(2):506–510 (1970).

[105] Gruverman, A.; Wu, D.; and Scott, J. *Piezoresponse Force Microscopy Studies of Switching Behavior of Ferroelectric Capacitors on a 100-ns Time Scale. Physical Review Letters*, **100**(9):097601 (2008).

[106] Avrami, M. *Kinetics of Phase Change. II Transformation-Time Relations for Random Distribution of Nuclei. The Journal of Chemical Physics*, **8**(2):212 (1940).

[107] Ishibashi, Y. *Polarization Reversal Kinetics in Ferroelectric Liquid Crystals. Journal of the physical society of Japan*, **24**:126 (1985).

[108] Siddons, D. P.; Hart, M.; Amemiya, Y.; and Hastings, J. B. *X-ray optical activity and the Faraday effect in cobalt and its compounds. Phys. Rev. Lett.*, **64**(16):1967–1970 (1990).

[109] Pfau, B.; Günther, C. M.; Könnecke, R.; Guehrs, E.; Hellwig, O.; Schlotter, W. F.; and Eisebitt, S. *Magnetic imaging at linearly polarized x-ray sources. Optics express*, **18**(13):13608–15 (2010).

[110] Hellwig, O.; Kortright, J. B.; Takano, K.; and Fullerton, E. E. *Switching behavior of Fe-Pt/Ni-Fe exchange-spring films studied by resonant soft-x-ray magneto-optical Kerr effect. Physical Review B*, **62**(17):11694–11698 (2000).

[111] Erskine, J. and Stern, E. A. *Calculation of the M(23) magneto-optical absorption spectrum of ferromagnetic nickel. Physical Review B*, **12**:5016–5024 (1975).

[112] Schütz, G.; Wagner, W.; Wilhelm, W.; Kienle, P.; Zeller, R.; Frahm, R.; and Materlik, G. *Absorption of circularly polarized x rays in iron. Phys. Rev. Lett.*, **58**(737) (1987).

[113] Stanton, L. *Selection rules for pure rotation and vibration-rotation hyper-raman spectra. Journal of Raman Spectroscopy*, **1**:53–70 (1973).

[114] Quindeau, A.; Hesse, D.; and Alexe, M. *Programmable ferroelectric tunnel memristor. Frontiers in Physics*, **2**(February):1–5 (2014).

[115] Chrisey, D. B. and Hubler, G. K. *Pulsed laser deposition of thin films.* Wiley-Interscience, New Jersey (1994).

[116] Martin, L.; Chu, Y.-H.; and Ramesh, R. *Advances in the growth and characterization of magnetic, ferroelectric, and multiferroic oxide thin films. Materials Science and Engineering: R: Reports*, **68**(4-6):89–133 (2010).

[117] Riet, E. V. D.; Nillesen, C. J. C. M.; and Dieleman, J. *Reduction of droplet emission and target roughening in laser ablation and deposition of metals. Journal of Applied Physics*, **74**(3):2008 (1993).

[118] Jordan, R.; Cole, D.; Lunney, J.; Mackay, K.; and Givord, D. *Pulsed laser ablation of copper. Applied Surface Science*, **86**(1-4):24–28 (1995).

[119] Li, T.; Lou, Q.; Dong, J.; Wei, Y.; and Liu, J. *Ablation of cobalt with pulsed UV laser radiation. Applied Surface Science*, **172**(3-4):356–365 (2001).

[120] Christen, H. M. and Eres, G. *Recent advances in pulsed-laser deposition of complex oxides. Journal of Physics: Condensed Matter*, **20**(26):264005 (2008).

[121] Hau, S. K.; Wong, K. H.; Chan, P. W.; and Choy, C. L. *Intrinsic resputtering in pulsed-laser deposition of lead-zirconate-titanate thin films. Applied Physics Letters*, **66**(2):245 (1995).

[122] Rijnders, G. and Blank, D. H. A. *Build your own superlattice. Nature*, **433**(January):369–370 (2005).

[123] Kim, S. and Byung-Teak, L. *Effects of oxygen pressure on the growth of pulsed laser deposited ZnO films on Si(001). Thin Solid Films*, **446**(2):307–312 (2004).

[124] Bozovic, I. and Eckstein, J. N. *Analysis of Growing Films of Complex Oxides by RHEED. MRS Bulletin*, **6**(May):32–38 (1995).

[125] Rijnders, G. J. H. M.; Koster, G.; Blank, D. H. A.; and Rogalla, H. *In situ monitoring during pulsed laser deposition of complex oxides using reflection high energy electron diffraction under high oxygen pressure. Applied Physics Letters*, **70**(14):1888 (1997).

[126] Rijnders, G. J. H. M.; Koster, G.; Blank, D. H. A.; and Rogalla, H. *In-situ monitoring during PLD of YBCO using RHEED at high oxygen pressure. IEEE*, **9**(2):1547–1550 (1999).

[127] Lagally, M. G. and Savage, D. E. *Quantitative Electron Diffraction from Thin Films. MRS Bulletin*, (January):24–31 (1993).

[128] Blank, D. H. A.; Koster, G.; Rijnders, G.; Setten, E. V.; Slycke, P.; and Rogalla, H. *Imposed layer-by-layer growth by pulsed laser interval deposition. Applied Physics A*, **22**:17–22 (1999).

[129] Van der Pauw. *A method of measuring specific resistivity and Hall effect of disks of arbitary shapes. Philips Research Reports*, **13**:1–9 (1958).

[130] Boschker, H.; Verbeeck, J.; Egoavil, R.; Bals, S.; van Tendeloo, G.; Huijben, M.; Houwman, E. P.; Koster, G.; Blank, D. H. A.; and Rijnders, G. *Preventing the Reconstruction of the Polar Discontinuity at Oxide Heterointerfaces. Advanced Functional Materials*, **22**(11):2235–2240 (2012).

[131] Tokura, Y.; Urushibara, A.; Moritomo, Y.; Arima, T.; Asamitsu, A.; Kido, G.; and Furukawa, N. *Giant Magnetotransport Phenomena in Filling-Controlled Kondo Lattice System:* $La_{1-x}Sr_xMnO_3$. *Journal of the physical society of Japan*, **63**(11):3931–3935 (1994).

[132] Urushibara, A.; Asamitsu, A.; and Sr, L. *Insulator-metal Transition and Giant Magnetoresistance In* $La_{1-x}Sr_xMnO_3$. *Physical Review B*, **51**(20):103–109 (1995).

[133] Nagarajan, V.; Junquera, J.; He, J. Q.; Jia, C. L.; Waser, R.; Lee, K.; Kim, Y. K.; Baik, S.; Zhao, T.; Ramesh, R.; Ghosez, P.; and Rabe, K. M. *Scaling of structure and electrical properties in ultrathin epitaxial ferroelectric heterostructures. Journal of Applied Physics*, **100**(5):051609 (2006).

[134] Hong, W.; Lee, H. N.; Yoon, M.; Christen, H.; Lowndes, D.; Suo, Z.; and Zhang, Z. *Persistent Step-Flow Growth of Strained Films on Vicinal Substrates. Physical Review Letters*, **95**(9):095501 (2005).

[135] Chen, F.; Tan, X.; Huang, Z.; Xuan, X.; and Wu, W. *Effect of electrode configurations on the process-induced imprint behavior of epitaxial* $Pb(Zr_{0.52}Ti_{0.48})O_3$ *capacitors. Applied Physics Letters*, **96**(26):262902 (2010).

[136] Liu, Y.; Lou, X.; Bibes, M.; and Dkhil, B. *Effect of a built-in electric field in asymmetric ferroelectric tunnel junctions. Physical Review B*, **88**(2):024106 (2013).

[137] Shahzad, K.; Khan, M. N.; Shabbir, G.; and Bashir, J. *Neutron and X-Ray Diffraction Crystal Structure Rietveld Analysis of* $PbTiO_3$ *Ceramics. Ferroelectrics*, **414**(1):155–161 (2011).

[138] Borisov, V.; Ostanin, S.; Maznichenko, I.; Ernst, A.; and Mertig, I. *Ab initio study of electronic transport in the Co/PZT-based tunnel junctions. DFG conference (talk)* (2014).

[139] Fechner, M.; Maznichenko, I.; Ostanin, S.; Ernst, A.; Henk, J.; Bruno, P.; and Mertig, I. *Magnetic phase transition in two-phase multiferroics predicted from first principles. Physical Review B*, **78**(21):212406 (2008).

[140] Fechner, M.; Ostanin, S.; and Mertig, I. *Effect of the surface polarization in polar perovskites studied from first principles. Physical Review B*, **77**(9):94112 (2008).

[141] Honma, T. and Wayman, C. M. *Epitaxial Growth of Evaporated Cobalt Films. Journal of Applied Physics*, **36**(9):2791 (1965).

[142] Mueller, S. and Scholten, P. *Die Gitterstruktur des Kobalts bei hohen Temperaturen. Zeitschrift für Angewandte Physik*, **20**:498–502 (1966).

[143] Borisov, V. S.; Ostanin, S.; Maznichenko, I. V.; Ernst, A.; and Mertig, I. *Magnetoelectric properties of the Co/Pb($Zr_x Ti_{1-x}$)O_3 (001) interface studied from first principles. Physical Review B*, **89**(5):054436 (2014).

[144] Xu, Y.; Ephron, D.; and Beasley, M. R. *Directed inelastic hopping of electrons through metal-insulator-metal tunnel junctions. Physical Review B*, **52**(4):2843–2859 (1995).

[145] Yin, Y. W.; Burton, J. D.; Kim, Y.-M.; Borisevich, a. Y.; Pennycook, S. J.; Yang, S. M.; Noh, T. W.; Gruverman, A.; Li, X. G.; Tsymbal, E. Y.; and Li, Q. *Enhanced tunnelling electroresistance effect due to a ferroelectrically induced phase transition at a magnetic complex oxide interface. Nature Materials*, **12**(2):397–402 (2013).

[146] Sun, J. Z.; Krusin-Elbaum, L.; Duncombe, P. R.; Gupta, A.; and Laibowitz, R. B. *Temperature dependent, non-ohmic magnetoresistance in doped perovskite manganate trilayer junctions. Applied Physics Letters*, **70**(13):1769 (1997).

[147] Vera Marún, I.; Postma, F.; Lodder, J.; and Jansen, R. *Tunneling magnetoresistance with positive and negative sign in* $La_{0.67}Sr_{0.33}MnO_3SrTiO_3Co$ *junctions. Physical Review B*, **76**(6):064426 (2007).

[148] Sun, J.; Roche, K.; and Parkin, S. *Interface stability in hybrid metal-oxide magnetic trilayer junctions. Physical Review B*, **61**(17):11244–11247 (2000).

[149] Duiker, H. M.; Beale, P. D.; Scott, J. F.; Paz de Araujo, C. a.; Melnick, B. M.; Cuchiaro, J. D.; and McMillan, L. D. *Fatigue and switching in ferroelectric memories: Theory and experiment. Journal of Applied Physics*, **68**(11):5783 (1990).

[150] Ramesh, R.; Chan, W. K.; Wilkens, B.; Gilchrist, H.; Sands, T.; Tarascon, J. M.; Keramidas, V. G.; Fork, D. K.; Lee, J.; and Safari, a. *Fatigue and retention in ferroelectric Y-Ba-Cu-O/Pb-Zr-Ti-O/Y-Ba-Cu-O heterostructures. Applied Physics Letters*, **61**(13):1537 (1992).

[151] Dawber, M. and Scott, J. F. *A model for fatigue in ferroelectric perovskite thin films. Applied Physics Letters*, **76**(8):1060 (2000).

[152] Wu, C.-L.; Lee, P.-W.; Chen, Y.-C.; Chang, L.-Y.; Chen, C.-H.; Liang, C.-W.; Yu, P.; He, Q.; Ramesh, R.; and Chu, Y.-H. *Direct spectroscopic evidence of charge reversal at the* $Pb(Zr_{0.2}Ti_{0.8})O_3/La_{0.7}Sr_{0.3}MnO_3$ *heterointerface. Physical Review B*, **83**(2):020103 (2011).

[153] Sudhama, C.; Campbell, a. C.; Maniar, P. D.; Jones, R. E.; Moazzami, R.; Mogab, C. J.; and Lee, J. C. *A model for electrical conduction in metal-ferroelectric-metal thin-film capacitors. Journal of Applied Physics*, **75**(2):1014 (1994).

[154] Eglitis, R. and Vanderbilt, D. *Ab initio calculations of* $BaTiO_3$ *and* $PbTiO_3$ *(001) and (011) surface structures. Physical Review B*, **76**(15):155439 (2007).

[155] Fechner, M.; Ostanin, S.; and Mertig, I. *Effect of oxidation of the ultrathin Fe electrode material on the strength of magnetoelectric coupling in composite multiferroics. Physical Review B*, **80**(9):094405 (2009).

[156] Bocher, L.; Gloter, A.; Crassous, A.; Garcia, V.; March, K.; Zobelli, A.; Valencia, S.; Enouz-Vedrenne, S.; Moya, X.; Mathur, N. D.; Marthur, N. D.; Deranlot, C.; Fusil, S.; Bouzehouane, K.; Bibes, M.; Barthélémy, A.; Colliex, C.; and Stéphan, O. *Atomic and electronic structure of the* $BaTiO_3$*/Fe interface in multiferroic tunnel junctions. Nano letters*, **12**(1):376–82 (2012).

[157] Bea, H.; Bibes, M.; Cherifi, S.; Nolting, F.; Warot-Fonrose, B.; Fusil, S.; Herranz, G.; Deranlot, C.; Jacquet, E.; Bouzehouane, K.; and Barthelemy, A. *Tunnel magnetoresistance and robust room temperature exchange bias with multiferroic* $BiFeO_3$ *epitaxial thin films. Applied Physics Letters*, **89**(24):242114 (2006).

[158] de Teresa, J. M.; Barthelemy, A.; Fert, A.; Contour, J.; Montaigne, F.; and Seneor, P. *Role of metal-oxide interface in determining the spin polarization of magnetic tunnel junctions. Science*, **286**(5439):507–9 (1999).

[159] Greullet, F.; Snoeck, E.; Tiusan, C.; Hehn, M.; Lacour, D.; Lenoble, O.; Magen, C.; and Calmels, L. *Large inverse magnetoresistance in fully epitaxial* $FeFe_3O_4MgOCo$ *magnetic tunnel junctions. Applied Physics Letters*, **92**(5):053508 (2008).

[160] Zhang, J.; Wang, Y.; Zhang, X.-G.; and Han, X. F. *Inverse and oscillatory magnetoresistance in Fe(001)/MgO/Cr/Fe magnetic tunnel junctions. Physical Review B*, **82**(13):134449 (2010).

[161] Shi, F.; Xiang, H.; Yang, J. J.; Rzchowski, M.; Chang, Y.; and Voyles, P. *Inverse TMR in a nominally symmetric CoFe/*AlO_x*/CoFe junction induced by interfacial* Fe_3O_4 *investigated by STEM-EELS. Journal of Magnetism and Magnetic Materials*, **324**(10):1837–1844 (2012).

[162] Maurice, J.-L.; Pailloux, F.; Barthélémy, A.; Durand, O.; Imhoff, D.; Lyonnet, R.; Rocher, A.; and Contour, J.-P. *Strain relaxation in the epitaxy of* $La_{2/3}Sr_{1/3}MnO_3$ *grown by pulsed-laser deposition on* $SrTiO_3$ *(001). Philosophical Magazine*, **83**(28):3201–3224 (2003).

[163] Ma, C.; Yang, Z.; and Picozzi, S. *Ab initio electronic and magnetic structure in $La_{0.66}Sr_{0.33}MnO_3$: strain and correlation effects. Journal of physics. Condensed matter : an Institute of Physics journal*, **18**(32):7717–28 (2006).

[164] Ziese, M.; Vrejoiu, I.; Setzer, A.; Lotnyk, A.; and Hesse, D. *Coupled magnetic and structural transitions in $La_{0.7}Sr_{0.3}MnO_3$ films on $SrTiO_3$. New Journal of Physics*, **10**(6):063024 (2008).

[165] Crassous, A.; Garcia, V.; Bouzehouane, K.; Fusil, S.; Vlooswijk, a. H. G.; Rispens, G.; Noheda, B.; Bibes, M.; and Barthelemy, A. *Giant tunnel electroresistance with $PbTiO_3$ ferroelectric tunnel barriers. Applied Physics Letters*, **96**(4):042901 (2010).

[166] Chen, F.; Schafranek, R.; Wachau, A.; Zhukov, S.; Glaum, J.; Granzow, T.; von Seggern, H.; and Klein, A. *Barrier heights, polarization switching, and electrical fatigue in $Pb(Zr,Ti)O_3$ ceramics with different electrodes. Journal of Applied Physics*, **108**(10):104106 (2010).

[167] Ibach, H. and Lüth, H. *Solid-State Physics.* Springer, New York (2009).

[168] Kötzler, J. and Gil, W. *Anomalous Hall resistivity of cobalt films: Evidence for the intrinsic spin-orbit effect. Physical Review B*, **72**(6):060412 (2005).

[169] Tsymbal, E.; Gruverman, A.; Garcia, V.; Bibes, M.; and Barthélémy, A. *Ferroelectric and multiferroic tunnel junctions. MRS Bulletin*, **37**(02):138–143 (2012).

[170] Yin, Y.-W.; Raju, M.; Hu, W.-J.; Weng, X.-J.; Zou, K.; Zhu, J.; Li, X.-G.; Zhang, Z.-D.; and Li, Q. *Multiferroic tunnel junctions. Frontiers of Physics*, **7**(4):380–385 (2012).

[171] Nogués, J. and Schuller, I. K. *Exchange bias. Journal of Magnetism and Magnetic Materials*, **192**(2):203–232 (1999).

[172] Berkowitz, A. E. and Takano, K. *Exchange anisotropy - a review. Journal of Magnetism and Magnetic Materials*, **200**(1-3):552–570 (1999).

[173] Tompkins, H. G. and Augis, J. A. *The oxidation of cobalt in air from room temperature to 467°C. Oxidation of Metals*, **16**(5-6):355–369 (1981).

[174] Tracy, J. B.; Weiss, D. N.; Dinega, D. P.; and Bawendi, M. G. *Exchange biasing and magnetic properties of partially and fully oxidized colloidal cobalt nanoparticles. Physical Review B*, **72**(6):64404 (2005).

[175] Manna, P. and Yusuf, S. *Two interface effects: Exchange bias and magnetic proximity. Physics Reports*, **535**(2):61–99 (2014).

[176] Kittel, C. *Introduction to Solid State Physics.* Wiley, Hoboken, NJ (2004).

[177] van der Zaag, P. J.; Ijiri, Y.; Borchers, J. A.; Feiner, L. F.; Wolf, R. M.; Gaines, J. M.; Erwin, R. W.; and Verheijen, M. A. *Difference between blocking and Néel temperatures in the exchange biased Fe_3O_4/CoO system. Physical Review Letters*, **84**(26 Pt 1):6102–5 (2000).

[178] van Lierop, J.; Lin, K.-W.; Guo, J.-Y.; Ouyang, H.; and Southern, B. *Proximity effects in an exchange-biased* $Ni_{80}Fe_{20}Co_3O_4$ *thin film. Physical Review B*, **75**(13):134409 (2007).

[179] Jensen, P. J.; Dreyssé, H.; and Kiwi, M. *Magnetic reordering in the vicinity of a ferromagnetic/antiferromagnetic interface. The European Physical Journal B*, **46**(4):541–551 (2005).

[180] Yang, F.; Tang, M. H.; Ye, Z.; Zhou, Y. C.; Zheng, X. J.; Tang, J. X.; Zhang, J. J.; and He, J. *Eight logic states of tunneling magnetoelectroresistance in multiferroic tunnel junctions. Journal of Applied Physics*, **102**(4):044504 (2007).

[181] Gould, C.; Rüster, C.; Jungwirth, T.; Girgis, E.; Schott, G.; Giraud, R.; Brunner, K.; Schmidt, G.; and Molenkamp, L. *Tunneling Anisotropic Magnetoresistance: A Spin-Valve-Like Tunnel Magnetoresistance Using a Single Magnetic Layer. Physical Review Letters*, **93**(11):117203 (2004).

[182] Wang, K.; Tran, T. L. A.; Brinks, P.; Sanderink, J. G. M.; Bolhuis, T.; van der Wiel, W. G.; and de Jong, M. P. *Tunneling anisotropic magnetoresistance in* $Co/AlO_x/Al$ *tunnel junctions with fcc Co (111) electrodes. Physical Review B*, **88**(5):054407 (2013).

[183] Yang, W.; Chang, K.; Wu, X. G.; Zheng, H. Z.; and Peeters, F. M. *Interplay between s-d exchange interaction and Rashba effect: spin-polarized transport. Journal of Physics C*, **17**:132112 (1984).

[184] Matos-Abiague, A. and Fabian, J. *Anisotropic tunneling magnetoresistance and tunneling anisotropic magnetoresistance: Spin-orbit coupling in magnetic tunnel junctions. Physical Review B*, **79**(15):155303 (2009).

[185] Matos-Abiague, A.; Gmitra, M.; and Fabian, J. *Angular dependence of the tunneling anisotropic magnetoresistance in magnetic tunnel junctions. Physical Review B*, **80**(4):045312 (2009).

[186] Useinov, A.; Kalitsov, A.; Velev, J.; and Kioussis, N. *Ferroelectric Control of Spin Transfer Torque in Multiferroic Tunnel Junctions* (2013).

[187] Nishida, K.; Kasai, S.; Tanaka, K.; Sakabe, Y.; Ishii, F.; and Oguchi, T. *First-Principle Studies on Elastic Properties and Spontaneous Polarizations of* $PbTiO_3$*. Japanese Journal of Applied Physics*, **40**:5806–5808 (2001).

[188] Kolmogorov, A. *Translated: Asymptotic expansions for the agreement criterion of Kolmogorov and Smirnov. Izv. Akad. Nauk, Ser. Math.*, **19**:103–124 (1955).

[189] Ishibashi, Y. and Takagi, Y. *On Distribution of Relaxation Times in Some Ferroelectrics. Journal of the physical society of Japan*, **31**(1):54,55 (1971).

[190] Dimmler, K.; Parris, M.; Butler, D.; Eaton, S.; Pouligny, B.; Scott, J. F.; and Ishibashi, Y. *Switching kinetics in* KNO_3 *ferroelectric thin-film memories. Journal of Applied Physics*, **61**(12):5467–5470 (1987).

[191] Orihara, H.; Hashimoto, S.; and Ishibashi, Y. *A Theory of D-E Hysteresis Loop Based on the Avrami Model. Journal of the physical society of Japan*, **63**(3):1031–1035 (1993).

[192] Pantel, D. *Multiferroische Tunnelkontakte.* Ph.D. thesis, Martin-Luther University Halle-Wittenberg (2011).

[193] Scott, J. F. *Ferroelectric Memories.* Springer, New York (2000).

[194] Kim, D.; Jo, J.; Kim, Y.; Chang, Y.; Lee, J.; Yoon, J.-G.; Song, T.; and Noh, T. W. *Polarization Relaxation Induced by a Depolarization Field in Ultrathin Ferroelectric $BaTiO_3$ Capacitors. Physical Review Letters*, **95**(23):237602 (2005).

[195] Wang, Z. Q.; Xu, H. Y.; Li, X. H.; Yu, H.; Liu, Y. C.; and Zhu, X. J. *Synaptic Learning and Memory Functions Achieved Using Oxygen Ion Migration/Diffusion in an Amorphous InGaZnO Memristor. Advanced Functional Materials*, **22**(13):2759–2765 (2012).

[196] Liao, Z.-M.; Hou, C.; Zhao, Q.; Wang, D.-S.; Li, Y.-D.; and Yu, D.-P. *Resistive switching and metallic-filament formation in Ag_2S nanowire transistors. Small*, **5**(21):2377–81 (2009).

[197] Jo, S. H.; Kim, K.-H.; and Lu, W. *Programmable resistance switching in nanoscale two-terminal devices. Nano letters*, **9**(1):496–500 (2009).

[198] Yang, Y.; Gao, P.; Gaba, S.; Chang, T.; Pan, X.; and Lu, W. *Observation of conducting filament growth in nanoscale resistive memories. Nature communications*, **3**:732 (2012).

[199] Liu, D.; Cheng, H.; Zhu, X.; Wang, G.; and Wang, N. *Analog Memristors Based on Thickening/Thinning of Ag Nanofilaments in Amorphous Manganite Thin Films. ACS applied materials & interfaces* (2013).

[200] Paruch, P.; Tybell, T.; and Triscone, J.-M. *Nanoscale control of ferroelectric polarization and domain size in epitaxial $Pb(Zr_{0.2}Ti_{0.8})O_3$ thin films. Applied Physics Letters*, **79**(4):530 (2001).

[201] Gruverman, A.; Wu, D.; Fan, H.-J.; Vrejoiu, I.; Alexe, M.; Harrison, R. J.; and Scott, J. F. *Vortex ferroelectric domains. Journal of Physics: Condensed Matter*, **20**(34):342201 (2008).

[202] Valencia, S.; Crassous, A.; Bocher, L.; Garcia, V.; Moya, X.; Cherifi, R. O.; Deranlot, C.; Bouzehouane, K.; Fusil, S.; Zobelli, A.; Gloter, A.; Mathur, N. D.; Gaupp, A.; Abrudan, R.; Radu, F.; Barthélémy, A.; and Bibes, M. *Interface-induced room-temperature multiferroicity in $BaTiO_3$. Nature materials*, **10**(10):753–8 (2011).

[203] Zak, J.; Moog, E. R.; Liu, C.; and Bader, S. D. *Magneto-optics of multilayers with arbitrary magnetization directions. Physical Review B*, **43**(8):6423–6429 (1991).

Acknowledgements

I would like to acknowledge all the hard working tax payers who allow us, and me personally through the SFB762 (Funktionalität Oxidischer Grenzflächen), to pursue our scientific aims.

Further more I gratefully want to thank:

My supervisor Prof. Dietrich Hesse, who gave me the opportunity to work in his fantastic group. His knowledge about condensed matter structure and characteristics were key to my understanding of many correlated phenomena that occurred during this work.

My supervisor and colleague Prof. Marin Alexe for numerous advises, leading directions, instrument introductions and proof-of-concept measurements. He had the ability to always find the right triggers to help me building up my confidence.

My colleague Norbert Schammelt for TEM lamella preparation, perfect reliability and incredible knowledge of generally every technical aspect in the lab.

Dr. Eckhard Pippel for giving me an insight into the Å-world with state of the art transmission electron microscopy.

Radu Abrudan for a very nice BESSYII experience; his help with data analysis and conceptual planning was very welcome. I could not have had a better and more effective time at a synchrotron facility.

Ignasi Fina for focussing my mind into the right direction and improving my measurements with conceptual discussions.

Vladislav Borisov, Dr. Sergei Ostanin and Prof. Ingrid Mertig for many fruitful discussions and support with state of the art theory insights of very similar solid-state systems.

Xavi Marti for his inspiration, discussion about data analysis and teaching in project-planning.

Dr. Holger Meyerheim for very solid proofs of LSMO layer termination and sample quality confirmation.

Geanina Apachitei for being such a reliable, supportive and effective colleague, helping me with SQUID measurements and sample preparation.

Sergiu Stratulat for pep-talks, physics philosophy, lots of welcome recreation and general motivation.

Daniel Pantel for the quick and effective introduction into a new topic.

Mareike Herrmann for the constant supply of tweezers, chemicals and gloves.

My colleagues Florian, Alessio, Hakan, Chengliang, Mr. Sven-Holger Stephan, Dr. Kim, Akash, Daniele, Flora, for a nice working environment.

My very special thanks go to my family:
My parents Ralf and Susanna and my sister Madita, who supported me always in every thinkable way.
My wife Gabrielle Hodgson, who gave me the confidence I needed to keep going during a brutal 2nd year. She enriches my life in so many ways. Thank you!

Declaration

Hiermit erkläre ich eidesstattlich, dass ich meine Dissertation selbständig und ohne fremde Hilfe verfasst und keine anderen als die von mir angegebenen Quellen und Hilfsmittel zur Erstellung meiner Dissertation verwendet habe. Die wörtlich und inhaltlich entnommenen Stellen habe ich als solche gekennzeichnet und den entnommenen Werken zugeordnet. Die Arbeit ist in vorliegender oder ähnlicher Form bei keiner anderen Prüfungsbehörde zur Erlangung eines Doktorgrades eingereicht worden.

Halle an der Saale, November 2014